Design and Manufacturing of Spatially Distributed and Interconnected Porous Architectures for Smart Dental Implants

by

Rana Dabaja

A dissertation submitted in partial fulfillment
of the requirements for the degree of
Doctor of Philosophy
(Mechanical Engineering)
in the University of Michigan
2024

Doctoral Committee:

Professor Mihaela Banu, Chair
Professor Bogdan I. Popa, Co-Chair
Professor Sun-Yung Bak
Professor Bogdan Epureanu
Professor Jonathan Fay
Professor Jerard Gordon
Professor Gustavo Mendonca

Rana Dabaja

rsdabaja@umich.edu

ORCID iD: 0009-0008-7297-6009

Dedication

This dissertation is dedicated to my family and friends whose unconditional support and love have been instrumental throughout this journey. Without you all, this would not have been possible. A special thank you to my mother and sister for their unwavering love and motivation to pursue a Ph.D.

Acknowledgments

First and foremost, I would like to thank Professor Banu for her continued support, encouragement, and mentorship throughout my Ph.D. I worked with Professor Banu throughout my undergraduate degree and have looked up to her as a role model ever since, especially within engineering. Thank you for challenging me and pushing me to grow as a researcher. Professor Banu has always been a source of encouragement, when a problem in my research seemed impossible, she always had a solution. Your guidance has pushed me to think outside the limits as a researcher. I appreciate your dedication as an advisor, I am truly grateful to have been a Ph.D. student in your group.

Additionally, I would like to thank my committee members, Professor Bogdan Popa, Professor Jerard Gordon, Dr. Sun-Yung Bak, Dr. Gustavo Mendonca, Professor Jonathan Fay, and Professor Bogdan Epureanu. Thank you for your support, guidance, and suggestions through my dissertation work.

I would like to thank our collaborators at the University of Michigan School of Dentistry, Ben Swanson and Dr. Yuji Mishina, Dr. Sun-Yung Bak, and Dr. Mendonca for their continued guidance throughout the project to develop a product that embodies multidisciplinary work.

Thank you to Nancy Muyanja at the Michigan Center for Materials Characterization for the guidance when conducting micro computed tomography scans and the support when it came to my research and academic career.

Thank you to Abdul Sayeed Khan for being a mentor and for collaborating with me in conducting compression tests. Thank you for your insight, guidance, support, and patience with the long hours spent configuring the DIC setup.

Thank you to Xhulja Biraku for being the best friend I could have asked for to go through this Ph.D. journey with. We have gone through it all together, from undergrad to our qualifying exams to our dissertations. I am truly grateful to have gone through all the tough and exciting times with you.

I would like to thank Daniel Rubio-Ejchel and Dillon Jobes, a part of the Gordon Group, for their support when experiments didn't always work out, guidance when I had to solve problems, collaborations, and our conversations. I always appreciated both of your feedback and unwavering support, especially during my dissertation proposal exam and dissertation.

A huge thank you to the Banu Lab, Dr. Metin Kayitmazbatir, Dr. Weiling Wen, Dr. Jaekwang Shin, Dr. Tae Hwa Lee, Xhulja Biraku, Abhishek Singh, Youngrok Lee, and Bhavana Komaraju from colleagues turned into friends. Thank you all for your support, guidance, and encouragement.

A big thank you to my family and friends for all the continued support throughout the years. Thank you to my closest friends for listening to me and being there for me through it all. To my mom, thank you for always believing in me, pushing me, and always being that positive light in my life, even when things weren't going as expected. A special thank you to my sister, Jenna, for your endless support, encouragement, and love that helped me persevere through my academic journey. To Jamil, thank you for your unconditional support, patience, and love throughout this journey. Above all, thank you for believing in me.

Table of Contents

List of Tables

List of Figures

Abstract

Dental implants serve as a prosthetic for missing teeth, aimed to replicate the natural tooth function. Titanium is the preferred material in the dental implant industry due to its biocompatibility with natural bone. Despite their widespread use, high associated risks persist, often detectable only long after insertion. Significant failures arise during the wound healing or bone remodeling phase accompanied by common occurrences of bone loss. Peri-implantitis, occurring post-insertion, leads to progressive bone loss attributed to a significant stiffness mismatch between the titanium implant and mandibular/maxillary bone. This mismatch creates non-uniform stress distributions, forming stress shields at the interface between the dental root and patient bone resulting in bone resorption. Additionally, edentulous patients with preexisting diseases causing low quality of bone, face even higher risks and, in some instances, are ineligible for dental implants due to weak metal-natural bond formation during the wound healing phase. Recent research focuses on inducing interconnected porous networks to encourage bone ingrowth and reduce stiffness to mimic bone properties. Pore characteristics, encompassing size, interconnectivity, porosity, and architecture, significantly influence cell attachment and mechanical structure properties. While existing research explores various porous architectures, a notable gap exists in comprehensive studies that evaluate and compare thier biological and mechanical performance.

This work presents a novel approach to designing and additively manufacturing (3D printing) a titanium dental implant. The design incorporates an embedded spatially distributed and interconnected microporous architecture with functionally graded properties that closely replicate the physical, biological, and mechanical behavior of bone. Two optimal porous architectures for biomedical applications, the triply periodic minimal surface (TPMS) gyroid variants and Voronoi stochastic are compared based on manufacturability, cell infiltration and adhesion, simulation, and compression testing. Understanding the impact of additive manufacturing on porous structure resolution facilitates the optimization of porous architectures and geometries. Using computer-aided design (CAD), the TPMS gyroid and Voronoi stochastic structures were modeled. A study on the feasibility of 3D printing porous titanium structures determined that the most favorable porous interconnectivity and distribution were achieved at a pore size of approximately ≥250µm. Subsequently, porous constructs were fabricated based on manufacturability for a set of in-vitro experiments, wherein a variant of the TPMS gyroid demonstrated superior cell adhesion and proliferation.

Given its outperformance in biologically and manufacturing aspects, The TPMS solid gyroid variant underwent mechanical testing at a range of pore size and porosity combinations to produce a functionally graded porous structure. The mechanical behavior is validated from a 2D digital image correlation developed compression test, micro computed tomography (micro-CT), and microscopy. Ultimately, the TPMS solid gyroid structures with a gradient of pore size (6-34%) and porosity (approximately 100-400 µm) demonstrate promising results. In summary, this dissertation developed a framework for fabricating a functionally graded porous dental implant with enhanced biological and mechanical properties, along with methods for comprehensive characterization.

Chapter 1 Introduction

1.1 Motivation

The beneficial effects of dental implants are revealed in market predictions to grow from USD 4.42 billion in 2023 to USD 6.95 billion by 2030 [1]. Statistics provided by the American Association of Oral and Maxillofacial Surgeons show that 69% of adults ages 35 to 44 have lost at least one permanent tooth to an accident, gum disease, a failed root canal, or tooth decay. Furthermore, by age 74, 26% of adults have lost all their permanent teeth. Dental implants address this issue better than all other alternatives (e.g., bridges). However, implant use has several constraints, including health conditions, the ability to pay a high cost ($2,500 - $4,500/tooth), and acceptance of the risk of failure, especially for edentulous patients. Titanium (Ti) implants account for the largest share of the global dental implant market (75.8%). Despite the large demand, challenges arise with the success of dental implant placements, with the risk of failure reaching as high as 10% [2], [3]. Additionally, there are categories of patients for whom the risk of dental implant failure remains high. A study done on medically compromised patients resulting in low bone mass density had success rates as low as 77.5% [2]. Areas with low bone mass density result in a higher risk of implant failure because of the lack of interfacial stability with bone tissue during the wound-healing phase [4]. The ultimate factor for successful dental implant placement is the biological process known as osseointegration, the direct connection between living bone and the surface of a load-bearing implant [5], [6], [7].

The factors for successful osseointegration include, but are not limited to, the bone-to-implant interface, implant material biocompatibility, and implant surface characteristics. Conversely, contributing factors to implant failure include the micromovements of the implant during early integration affecting the bone-to-implant interfacial contact, pre-existing diseases in patients that negatively influence healing, decreased bone quality at the implant site, and stress shielding [3]–[8]. In all cases, the bone healing is compromised, affecting the interface between the implant and bone, either impairing the event of osseointegration or leading to insufficient remaining bone structure. More specifically there are two primary events that are discussed and identified facing challenges in current dental implant solutions. First, medically compromised patients with pre-existing diseases affecting the bone quality in the maxillary become ineligible to receive these dental implants because of low bone mass density. Low bone mass is associated with a higher risk of implant failure because of the lack of interfacial stability with the bone tissue in the beginning stages of osseointegration upon insertion [4]. The second is implant failure led by the metallic implant's material properties. This can occur in healthy or diseased bone due to the stiffness mismatch between the industry-standard titanium implant and bone. The high stiffness mismatch results in a phenomenon known as stress shielding, where there is an insufficient load transfer between the bone and implant, leading to weakened remodeled bone [8], [9], [10].

In implants with minimally rough surfaces, there existed a lower percentage of AcH3-positive cells [11]. This indicates that a rough and porous implant could enhance osseointegration during the wound-healing phase to promote the adhesion of cells and osseointegration. In this respect, inducing pores within the implant can be an optimal solution for solving the issues of the limitations of implants mentioned. The ingrowth of bone within the pores would serve to enhance the interfacial strength between the bone and implant potentially making it possible for medically compromised patients deemed ineligible because of low bone mass density and bone loss to receive the implants. Simultaneously, the pores would reduce the strength of the titanium implant, resulting in a stiffness that would more closely match that of bone to reduce the stress shielding effect. Prior work has shown that the induction of a porous architecture into a titanium dental implant resulted in enhanced biological performance and a reduction in stress shielding. This work seeks to develop a novel porous architecture, more specifically a scaffold, to improve the interfacial connection between the bone and implant in the maxillary, while reducing the stiffness to mimic that of bone. Utilizing additive manufacturing, with its layer-by-layer approach, making a porous structure possible.

1.2 State of the Art

The industry standard material for biomedical implants is titanium and its alloys, namely Ti6Al4V extra low interstitial (ELI) grade 23 due to its superior biocompatibility and mechanical properties compared to other materials [12], [13]. It is a variant of Ti6Al4V grade 5, with low levels of interstitial elements such as iron, carbon, nitrogen, and oxygen, leading to higher corrosion resistance, better fracture toughness, and higher ductility [12], [13], [14]. The titanium alloy Ti6Al4V ELI exhibits the lowest elastic modulus compared to other implant materials, such as commercially pure titanium, while maintaining biocompatibility, leading to a more advantageous stress distribution [12]. However, its high elastic modulus relative to that of bone remains a challenge. Ti6Al4V has an elastic modulus of 114 GPa, significantly higher than cancellous (3.5-125.6 MPa) and cortical (12.7-22.8 GPa) bone [14], [15], [16]. The presence of the metallic implant causes a reduction in the load transferred from the high-stiffness implant to the bone, resulting in bone resorption [17], [18].

In dental practice, bone grafts are instrumental in addressing bone loss and further deterioration. Autografts represent the gold standard for addressing severe bone loss, providing a robust foundation for implants and exhibiting strong osteogenic characteristics that contribute to effective bone healing, modeling, and remodeling. [19], [20], [21], [22]. Success rates for autografts can reach as high as 95% [19]. However, autografts are not without limitations, including susceptibility to diseases, pain, and visceral injuries [22]. The process involves the transportation of bone from a donor site to another location within the same patient and are typically reserved for critical cases, such as jaw reconstructions, congenital bone defects, and tumors [20], [21]. Despite their established gold standard status, autografts present challenges, including a heightened risk of infections, uncertain prognoses, and complications [20], [23]. Additionally, they are less favorable due to the requisite extra surgery, increased costs, the involvement of a multidisciplinary team, and associated complications [20]. Nevertheless, autogenous bone grafts maintain their gold-standard status in bone regeneration. In contrast, allografts, involving the utilization of tissue from another person, are considered less favorable due to the associated risks of immune rejection, blood incompatibility, and disease transmission [22]. Moreover, bone grafts in medically compromised patients introduce additional complexities, as extracting bone from compromised areas can impact success rates depending on the overall health conditions of the patient. A further limitation lies in the reported success rates for autografts in dental implants, with medically compromised patients often excluded from the success rates [24], [25]. While survival rates for dental implants are generally high, an unintentional selection bias persists in private practice success rates. Variables such as the clinician's experience, time spent at appointments, and clinician-specific inclusion and exclusion criteria for patients contribute to the variability in dental implant results and success rates [26].

Manipulating the surface characteristics of dental implants has been a popular route in dental implants to enhance osseointegration and strengthen the interface between the bone and implant. The primary and secondary stability of osseointegration can be influenced by the surface characteristics of the titanium implant. The addition of roughness will increase the surface area, stimulating the growth and production of osteoblasts, which will positively influence osseointegration. A better bone fixation is achieved with surface roughness comparted to a smooth surface, thus researchers have explored multiple methods for manipulating implant surface characteristics to improve cell adherence [27], [28]. Common surface modification processes used in the field of dental implants include sand-blasted large-grit acid etching (SLA) and hydroxyapatite coating [6], [29], [30], [31]. SLA is a process where ceramic particles, usually 250-500µm, are sandblasted at a high velocity through a nozzle from the pressure of a fluid or compressed air to create craters on the surface of the implant, then dipped into an acid solution to remove any remaining unwanted particles and to create a microroughness [29], [32]. The microroughness increases the surface area consequently enhancing cell adhesion, improving osseointegration, and further increasing the survival rate. SLA was found to be more advantageous than acid-etching only or machining the implants. The second standard to enhance cell adhesion in the dental implant industry is coating the implant with hydroxyapatite (HAp) using plasma spraying [33]. HAp is a synthetic ceramic biomaterial with a chemical composition comparable to the natural components of bone, including calcium and phosphate and is one of the most used processes for creating a rough surface on titanium [29], [30]. The high biocompatibility of HAp to bone creates a higher interfacial strength between the implant and bone, enhancing cell adhesion, thus improving bone healing. HA exhibits disadvantages during failure, clinical studies found failures with HA coating had more bacterial microleakage and periimplant tissue complications. there are some concerns regarding HA coated implants including microbial adhesion, osseous breakdown and coating failure. However, the authors proposed that these implants could be beneficial in grafted bone or type IV bone where more rapid bone implant contact is needed [29]. Although rough surface implants promote osseointegration and have been shown to increase bone-to-implant contact relative to a smooth surfaced implant [33], [34], there is concern with HA used on implants in that there is poor binding, breaking at the interface, or even separating after several years [29], [35]. Further, even with SLA there is the disadvantage still exists that titanium is still highly dense, leading to an uneven stress distribution between bone and the implant resulting in stress shielding causing implant loosening, bone loss, and implant failure.

1.3 Proposed Approach

Based on the literature review of the industry's implant function, purpose, and current solutions, the approach to tackle the current problems existing within implants was developed. The approach included the study of two main bioinspired designs found to be optimal for enhancing cell proliferation while maintaining structural integrity. Based on the findings of those porous architectures, the optimal and uniquely possible way of fabrication was through the use of additive manufacturing (3D printing), specifically selective laser melting (SLM). The manufacturability of the porous architectures was then validated for manufacturability, mechanical integrity, and biological performance. The combination of these constructed a uniquely and novel design for an alternative to dental implants.

1.4 Thesis Overview

This research aims to develop an innovative design and fabrication technique as an alternative to existing dental implant solutions for edentulous patients deemed ineligible because of bone loss while mitigating the stress shielding effect for patients with healthy and medically compromised bone by matching the mechanical priorities of the implant with that of the surrounding bone. The approach involves inducing an intricate carefully designed porous architecture into titanium dental implants, fostering bone ingrowth, and reinforcing the implant-bone interface. Various porous architectures deemed optimal for biomedical applications were comprehensively studied to achieve these objectives, exploring their biological, mechanical, and manufacturability aspects.

In Chapter 3, computer-aided design (CAD) software is utilized to create two distinct porous scaffold designs: the Voronoi stochastic structure and the gyroid triply periodic minimal surface (TPMS). Various pore sizes are implemented, and the scaffolds are additively manufactured with Ti6Al4V ELI grade 23 powder using selective laser melting (SLM). The designs were subjected to micro computed tomography (micro-CT) analysis to evaluate their porosity, interconnectivity, pore size, and frequency of pores. Three potential porous scaffolds are identified for further experimentation, emphasizing optimal cell growth, mechanical strength, and manufacturability.

Chapter 4 delves into the biological behavior of the three optimized scaffolds through in vitro experiments using bone mesenchymal stromal cells. RNA quantity analysis, scanning electron microscopy (SEM), and confocal fluorescent microscopy are employed to assess cell quantity, activity, and adhesion. Computational fluid dynamics (CFD) analysis is conducted to determine scaffold permeability, offering insights into cell infiltration and trajectory. The chapter concludes with an evaluation of the potential of the porous structure based on its biological response.

Chapter 5 investigates the mechanical behavior of the optimal porous architecture identified in Chapter 4 under compression. The novel technique of digital image correlation (DIC) is developed for microporous structures to accurately analyze strain. The TPMS solid gyroid structure is characterized post-failure using microscopy and SEM to determine the modes of failure. The chapter contributes by providing the elastic modulus for five porous structures, establishing a functionally graded porous structure based on ascending pore size and porosity. Chapter 6 provides a summary of the research and outlines future directions and potential extensions, discussing porosity design techniques and additional experiments for pore characterization.

Chapter 2 Literature Review

2.1 Dental Implant Background

The prosthesis for a missing tooth is known as a dental implant. It consists of the crown, abutment, and implant fixture. Figure 1.1 shows a diagram of the implant against a natural tooth. The highlighted yellow region is the region of interest, it is the interface between the implant and the surrounding bone. The modes of failure occur due to complications occurring at the interface between the implant and surrounding bone. The industry-standard dental implant material is the titanium alloy known as Ti6Al4V., offering high biocompatibility, resistance to corrosion, and low density in relation to other metallic materials. Dental implant success is defined by two different phases of osseointegration known as primary and secondary stability. On the other hand, dental implant failure is classified into early and late failure both affected by primary and secondary stability. Primary stability occurs upon insertion, the immediate interaction between the implant and bone a prerequisite for osseointegration, while secondary stability occurs during the bone remodeling stage of osseointegration, that can later lead to late dental implant failure [36]. In other words, early implant failure occurs before implant loading and is solely related to biological complications. Conversely, late implant failure happens after implant loading usually occurring because of bone resorption or mechanical complications from the fracture of the implant [37], [38].

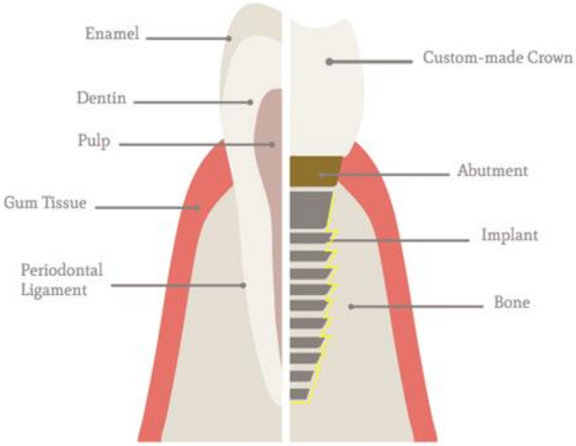

Figure 2.1 A Dental Implant Diagram

2.1.1 Factors of Dental Implant Success

The long-term success of dental implants is attributed to osseointegration. In dental implants, long-term success is associated with osseointegration, the direct connection between living bone tissue and the surface of a load-carrying implant occurring at the interface [1,2]. The ultimate success and effectiveness of osseointegration depends on the topography of the implant. The properties of the surface of the implant are crucial for adhesions and the differentiation of osteoblasts (cells that form new bone) during the initial phase of osseointegration and long-term bone remodeling [2]. We separated osseointegration into four key phases, inflammatory, proliferation, maturation of bone, and remodeling. In the initial phase, healing occurs immediately upon insertion, and a blood clot forms to initiate the inflammatory response, proteins and bone forming cells begin to leak. After this, osteoblasts begin to produce new bone around the implant surface in the form of new woven bone to establish a foundation for invading cells and bone development. During maturation the immature bone is replaced by mature lamellar bone, becoming more integrated with the surrounding bone. After this, the implant starts to gain mechanical stability where the bone begins to adapt to its environment remodeling based on the loads applied. The last phase in particular important for achieving long-term success [5], [39]. Common failures of dental implants occur in the wound-healing and bone-remodeling phases. Thus, it is important to understand the bone-to-implant interaction. There exist two causes for the impairment of osseointegration, the first during the wound healing phase where the implant interacts at the cellular and protein level and during the bone remodeling phase after the new woven bone structure has been created. Challenges still arise with the success of dental implant placements, with the risk of failure reaching as high as 10% [2], [3]. The factors that contribute to this type of failure are the micromovements of the implant during the time of osseointegration, pre-existing diseases in patients that cause bone loss, low bone quality, and stress shielding [3], [9], [10], [40], [41], [42]. Significant pre-existing diseases in patients include uncontrolled diabetes and periodontal disease, which compromise the bone-tissue interface, resulting in impaired osseointegration [42], [43]. A study done on medically compromised patients resulting in low bone mass density had success rates as low as 77.5% [2]. Areas with low bone mass density result in a higher risk of implant failure because of the lack of interfacial stability with bone tissue during the wound-healing phase [4]. Implants can have microscopic pits, grooves, and protrusions to increase the surface area to give a position to hold the bone tissue. This sets the stage for the biological responses at the interface of the bone and implant, where there is an opportunity to manipulate osseointegration to enhance it. Additionally, osteoclast activity is vital during the remodeling stage of osteointegration. Osteoclasts specialize in bone resorption, breaking down old or damaged bone. This process allows room for osteoblasts to deposit new bone, ensuring bone quality maintenance and facilitating adaptation at the bone-implant interface [44].

2.1.2 Dental Implant Failure Associated with Bone Remodeling

Although the titanium alloy Ti6Al4V Grade 23 is an industry-standard material for dental implants due to its superior biocompatibility and mechanical properties compared to other materials, its high elastic modulus relative to that of bone remains a remains a challenge [12], [45], [46], [47]. Ti6Al4V has an elastic modulus of 114 GPa, significantly higher than cancellous (3.5-125.6 MPa) and cortical (12.7-22.8 GPa) bone [14], [15], [16]. The difference in mechanical properties results in a prominent mode of failure during the bone remodeling phase of osseointegration known as stress shielding, [8], [9], [10]. According to Wolff's law, bone mass adapts to its mechanical environment from physiological loading during bone remodeling. The presence of the metallic implant causes a reduction in the load transferred from the high-stiffness implant to the bone resulting in bone resorption [17], [18]. The titanium implant will absorb a majority of the stress from the occlusal forces, and the bone will experience low stresses. Based on this, bone receiving reduced mechanical stimulus will start to degenerate by becoming more porous or decreasing in volume [48], [49]. The presence of the metallic implant causes a reduction in the load transferred from the high-stiffness implant to the bone resulting in bone resorption [17], [18]. To reduce stress shielding and enhance osseointegration, surface characteristics are modified. The reason for this enhanced effect is attributed to the relationship between porosity and mechanical properties generated by them [50]. Understanding the reasons of failure between the implant and bone both biologically and mechanically has gained interest in developing an alternative for dental implants, where a porous architecture is embedded into the solid implant to better integrate bone within the implant rather on the surface and specifically mimicking the stiffness properties of bone. Ultimately, this promotes bone ingrowth strengthening the bone to implant interface potentially enhancing osseointegration in the early stage. The mimicked mechanical properties then serve to creating a more uniform stress distribution where a stronger bone is remodeled to mitigate late implant failure.

2.2 Porous Design and Fabrication Methods for Dental Implant Alternatives

2.2.1 Influence of Porous Architectural Geometry on Dental Implants

The framework for porous architectures influences the biological and mechanical performance of scaffolds. The geometric parameters influencing these effects are pore size, interconnectivity porosity, and spatial placement of pores. First, pore sizes influence the flow of nutrients and bone growth. Bone volume increases with pore size, as shown in a previous study [51]. Pore sizes ranging between 60-125µm only showed bone formation on the outer surface, whereas pore sizes ranging from 125-250µm, 250-425µm, and 425-600µm supported uniform bone formation throughout the cross section [51]. Specifically, sizes ranging from 125-250µm and 250-425µm showed a similar amount of bone formation, the scaffolds with pore sizes from 425-600µm did not show a significantly higher amount of bone formation than the 125-425µm pore sizes[51]. A similar study showed that pore sizes in the range of 200-350µm were optimal for bone growth with a minimum pore size of 100µm for the diffusion of nutrients [52]. It was found that larger pore sizes, 500um, did not affect cell attachment, but between 300-400µm pore sizes found it was good for capillary infiltration for fluids and cells and fibroblasts completely covered the scaffolds with a pore size of 300µm and 400µm [53], [54] . Higher curvature showed a high bone growth rate because of the small spaces between the struts, leading to more tissue growth [55]. Pores less than 125µm were fount to prevent functional differentiation of an osteogenic tissue phenotype in vivo for both cell types, these small pores inhibit matrix mineralization, while sufficiently large (>250µm) pores facilitate robust mineralization [56].

Tuning the porous architecture becomes significant when embedding them in the scaffolds. Small pore sizes promote protein adsorption, large pore sizes allow for vascularization and new bone ingrowth [53]. Understanding this becomes important when designing the porous architecture and placing the porosities throughout the scaffold. Zumofen et al., suggested there is no optimal pore size, rather an optimal pore size range [57]. Previous studies showed the optimal pore size to promote bone growth ranges from 250 – 425µm and 200-300µm with a minimum pore size for vasculature ingrowth [51], [52], [56].

The architecture of the pores is another important factor that affects the mechanical and biological behavior of the implant and surrounding bone. Lattice structures, three-dimensional structure made up of pores interconnected by struts, are widely being studied for biomedical applications because of their biocompatibility, strength, and ability to be engineered as components in the human body to replace diseased human tissue and bone [58]. Not only this, but the mechanical properties are able to be altered to meet specific design requirements and structural characteristics. Within lattices, there are closed pores or open pores. Figure 2.2 shows closed pores with no interconnectivity, while open pores are interconnected. The interconnection of pores is important for the transport of nutrients and the trajectory of cell growth [59]. Various porous architectures exist that include randomly and uniformly distributed pores within those open and closed pores.

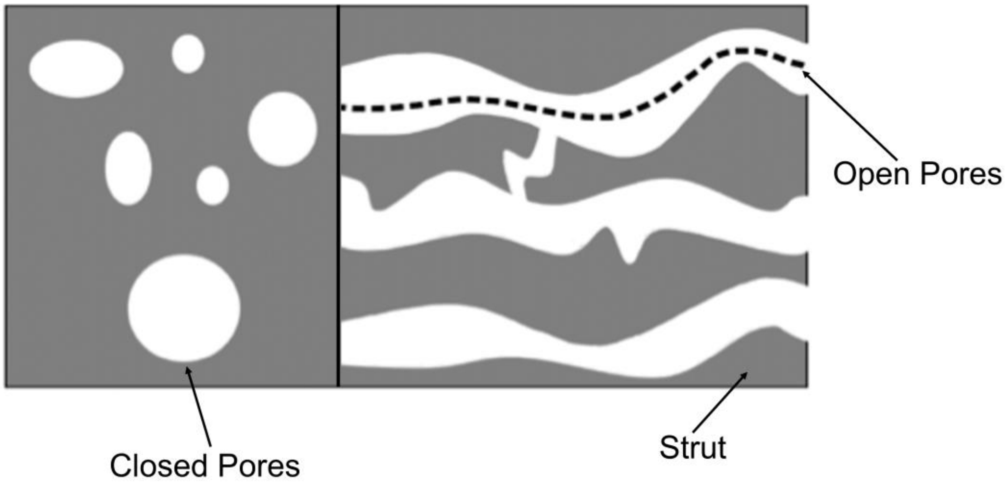

Figure 2.2 Example of a closed pore and open pore lattice structure

There exists a variation of porous designs to manipulate the architecture of lattices. Namely two lattices structures are studied most favorable for biomedical applications, the triply periodic minimal surfaces (TPMS) and the stochastic structure using the Voronoi tessellation method. Stochastic lattices mimic the non-uniformity and randomness of bone with pores randomly applied to a finite space and the TPMS structure is highly interconnected and can be controlled. A TPMS structure is continuous and periodic in three independent perpendicular directions and is a minimal surface because there is a mean curvature of zero at every point on the surface [1], [2]. The highly curved surfaces of TPMS structures promoted tissue regeneration in comparison to a flat surface [60]. The Voronoi stochastic structure mimics the non-uniformity of bone [61], [62]. Based on feature size, biological response, and mechanical properties it is important to comprehensively analyze these characteristics to understand optimal architecture for the intended use of the implant.

Porous materials, while increasing surface area for enhanced cell attachment, compromise mechanical strength, impacting their ability to withstand physiological loading [59], [63]. To address the trade-off between porosity and mechanical integrity, a porous structure is designed with functionally graded properties with the incorporation of channels leading to a dense core. This design approach aims to provide the necessary strength to withstand physiological loading while enhancing biological performance [64].

2.2.2 Functionally Graded Porous Materials

Based on the various roles pore size plays in cell attachment and the maintenance of mechanical integrity for a porous structure, functionally graded materials are proposed to improve the biological and mechanical performance. A functionally graded material is designed with a gradual variation in porosity, pore size, and mechanical properties and this closely mimic the natural structure of bone. Implementing this architecture into a metallic dental implant promotes a more seamless transition from the implant to the host tissue. This can lead to enhanced biological responses and better integration. Not only this, but helps to minimize the stress shielding effect where the excessively stiff implants shield surrounding bone from mechanical loading potentially leading to bone resorption. The gradual change in properties avoids the abrupt transitions between the implant and bone, creating a better stress distribution. The mechanical properties can be tailored along the gradient to customize it based on the patient-specific requirements.

Biologically the varying pore sizes have an effect on the biological response of the cells. This would support enhanced osseointegration providing a favorable environment for bone ingrowth, vascularization, and the formation of a robust bone-implant interface. Pore sizes directly influence the ability of cells to and populate the scaffold. Smaller pores may limit cell infiltration, while larger pores may encourage it. Functionally graded scaffolds can incorporate a range of pore sizes to accommodate different cell types and their migration needs. Small pores provide a high surface area and are effective in promoting initial cellular attachment to the scaffold. They allow for close interaction between cells and the implant surface, facilitating the early stages of osseointegration. contribute to efficient nutrient and oxygen diffusion, supporting the metabolic needs of cells near the surface of the implant. This is essential for the viability and function of cells involved in the early stages of tissue regeneration. Large pores are conducive to cellular ingrowth and tissue vascularization. They create pathways for blood vessels and bone-forming cells to penetrate deep into the scaffold, promoting the formation of new bone tissue throughout the implant. Large pores play a critical role in supporting vascularization within the implant. Vascular networks are essential for delivering nutrients, oxygen, and signaling molecules to cells throughout the scaffold, ensuring sustained cell activity and tissue development. Small and large pores allow for the adaptation of the implant to these diverse conditions of bone, ensuring that the scaffold supports osseointegration regardless of the local tissue characteristics. It is suggested that small pores are closes to the core of an implant to increase mechanical strength, and large pores on the outer surface to enhance cell penetration and proliferation [65]. Although uniform structures could also provide a suitable environment for cell adhesion, studies showed that the graded structures could provide a better stress distribution and energy absorption with increased load bearing capacities [66], [67] .

In summary, the incorporation of both small and large pore sizes in a dental implant scaffold is a strategic design approach to facilitate optimal osseointegration. It addresses the complex interplay of cellular responses, nutrient transport, vascularization, and bone tissue formation, contributing to the overall success and longevity of the implant in the oral environment. The graded approach allows for a more harmonious integration with the host tissue, improved long-term stability, reduced risk of complications, and optimized biomechanical performance, making them a promising advancement in the field of dental implantology.

2.3 Manufacturing Techniques for Induced Porous Architectures

Conventional manufacturing methods, such as subtractive manufacturing, limit the development of complex designs. This includes turning, milling, grinding, stamping and more where material is removed from a fully solid object [68], [69]. This becomes a challenge to design and manufacture more intricate and novel parts. On the other hand, additive manufacturing, colloquially known as 3D printing, uses a bottom-up approach to alleviate geometric design constraints [70]. A layer-by-layer approach is used, thus reducing material waste and allowing for more complex, customizable part with the addition of hollow structures that could not otherwise be achieved with conventional methods [71], [72]. This becomes especially important in the field of orthopedic implants, where the mechanical integrity and porosity need to be maintained. There exists a variety of additive manufacturing techniques, and among them laser-powder bed fusion (LPBF) is the most common for implant applications for Ti6Al4V and fabricating metallic implants [70], [72], [73]. Its notable technique in AM, utilizes a laser beam to selectively melt metal powders layer by layer to create a three-dimensional product. Selective laser melting (SLM) is the specific technique falling under LPBF that offers the capability to create complex structures with almost no constraints with high precision, maintaining density and enabling the production of 3D porous scaffolds and patient-specific medical devices [74], [75], [76]. This makes it especially advantageous for fabricating porous structures and internal geometries, while maintaining high density, and machine parameters can be manipulated to induce surface roughness [77]. The printing parameters of SLM can affect the part quality, geometrical accuracy, and overall density, thus careful tuning of the print parameters is required.

The schematic diagram of the SLM process is shown in Figure 2.3, where the arrows indicate the direction of motion of each part. The general process of the selective laser melting technique begins with the designed computer-aided design (CAD) model, then converted to a stereolithography format for it to be sliced in 2D, a pre-processing software is used to add supports where required and create the tool path for the laser scanning. The file is then input to the SLM machine, once the process begins the recoater spreads a thin layer of powder from the powder stock onto the powder bed, a high energy laser beam selectively melts the powder according to the toolpath from each 2D slice, for the powder bed is lowered in increments after each layer for the addition of a new powder layer to be laser melted fusing it to the previous layer. The process is repeated until the entire object is built layer by layer.

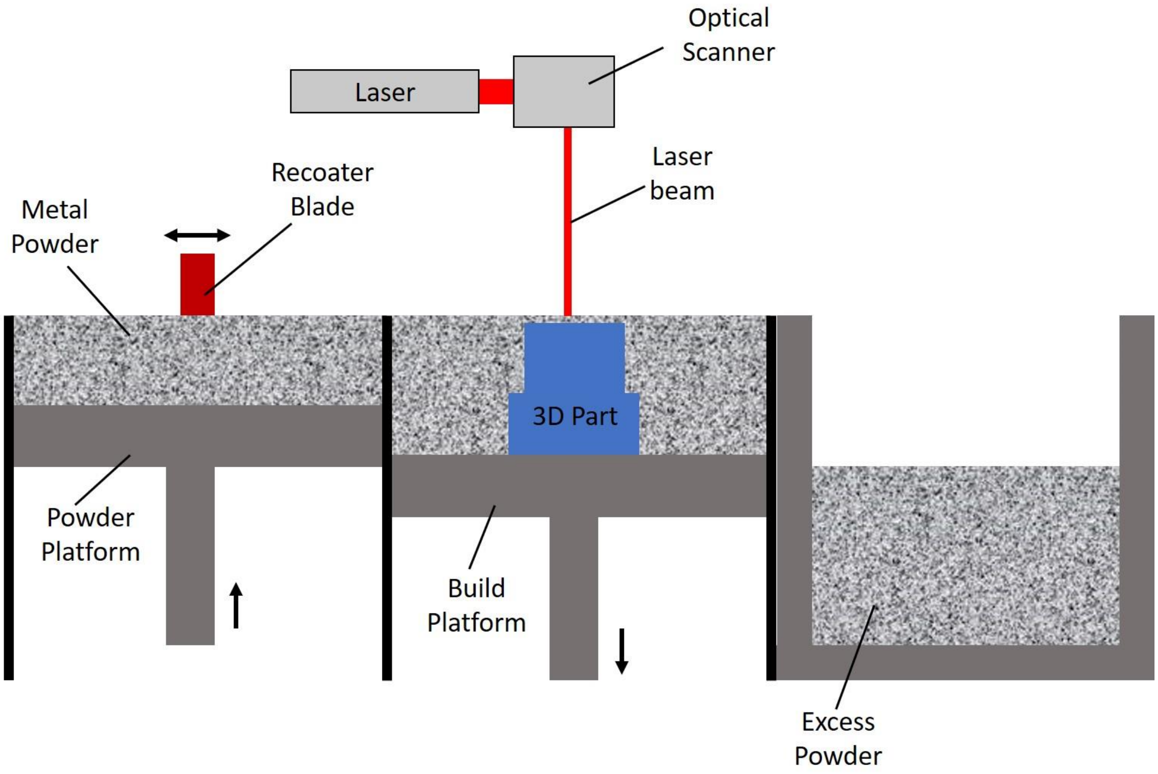

Figure 2.3: Schematic diagram of the SLM process

2.4 Summary and Conclusions

The literature review in this chapter is crucial for building a practical framework to overcome the drawbacks of current dental implant solutions. The analysis of both early and late dental implant failures provides valuable insights into the intricate relationship between bone and titanium structures. This understanding, encompassing both biological and mechanical aspects, provides a foundation for identifying potential solutions for these failures.

The review suggests that incorporating a porous architecture, conducive to cell growth while maintaining mechanical integrity, is a practical solution based on the identified implant failures. Ultimately creating a porous metallic scaffold to mimic the biological and mechanical properties of bone. Additionally, exploring the capabilities of additive manufacturing opens up the possibility of creating a functionally graded porous architecture, which could significantly enhance bone ingrowth. By synthesizing information from the literature on current solutions, failure mechanisms, determining factors for success, and manufacturing capabilities, a robust framework for developing a new dental implant technology is established. This framework not only addresses the shortcomings of existing solutions but also utilizes advanced manufacturing techniques to create a more effective and durable dental implant.

Chapter 3 Design and Fabrication Methods for Porous Architectural Metallic Implants

The application of lattice structures in biomedical research has led to the identification of two distinct porous architectures, namely the triply periodic minimal surface (TPMS) gyroid structure and the stochastic Voronoi structure. These structures are identified because of their potential to enhance cell proliferation and maintain mechanical integrity while decreasing the elastic modulus, contributing to a reduction in the stress-shielding effect. A comprehensive study is crucial to assess their feasibility, focusing on key factors such as pore size, porosity, interconnectivity, and controllability concerning manufacturability, resolution, and characterization. The entirety of the work conducted in this chapter is depicted in Figure 3.1. This chapter introduces the design process and methods of the TPMS gyroid and Voronoi stochastic architectures. Following this, we delve into the fabrication process using the selective laser melting (SLM) additive manufacturing technique of the introduced porous architectures. The optimal porous architecture is determined based on the resolution of the fabricated samples, supported by the results obtained from micro computed tomography (micro-CT) scans.

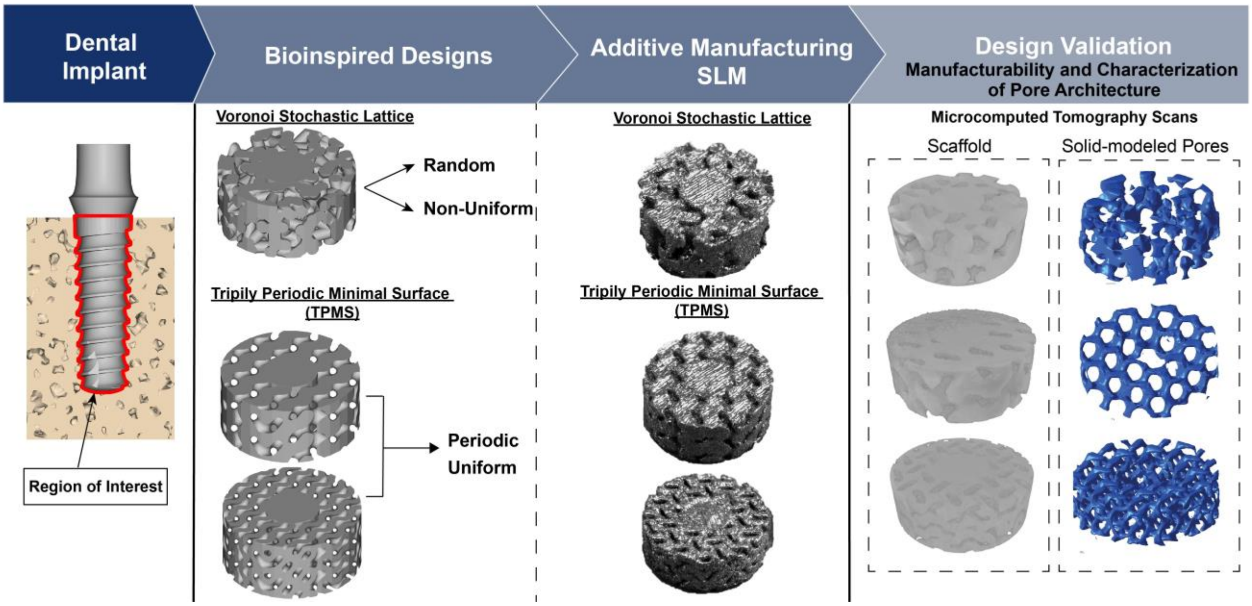

Figure 3.1: The design and manufacturing process for the optimal microporous scaffold architecture. The proposed bioinspired designs are created in CAD and additively manufactured using SLM. The designs are validated from the characterization and manufacturability.

3.1 Introduction

In the field of dental implants, osseointegration, the direct connection at the interface of living bone tissue and the surface of a load-bearing implant, is crucial for successful oral rehabilitation in edentulous patients [5], [6], [7]. However, challenges arise with the success of dental implant placements, with the risk of failure reaching as high as 10% [2], [3]. Implant failures occur during the bone healing phase and the bone remodeling phase. During the bone healing phase, pre-existing diseases in patients, such as uncontrolled diabetes and periodontal disease compromise the interfacial connection between the solid implant and bone [6-12]. During the bone remodeling phase, a phenomenon known as stress shielding occurs leading to implant failure [14]. The phenomenon is caused by the differences in mechanical properties between the bone and titanium implant [8], [9], [10]. According to Wolff's law, bone mass adapts to its mechanical environment from physiological loading during bone remodeling. The presence of the metallic implant causes a reduction in the load transferred from the high-stiffness implant to the bone resulting in bone resorption [17], [18]. Although the titanium alloy Ti6Al4V Grade 23 is an industry-standard material for dental implants due to its superior biocompatibility and mechanical properties compared to other materials, its high elastic modulus relative to that of bone remains a challenge [12], [45], [46], [47]. Ti6Al4V has an elastic modulus of 114GPa, significantly higher than cancellous (3.5-125.6MPa) and cortical (12.7-22.8 GPa) bone [14], [15], [16]

To address the risks of dental implant failure during the bone remodeling and healing phase, porous scaffolds as a replacement for implants have been developed and serve to reduce the elastic modulus, mitigating the effects of stress shielding and consequently providing channels for the transport of nutrients and bone ingrowth for enhanced osseointegration. Suitable architecture, including pore size, porosity, geometry, and interconnectivity, is fundamental to increasing cell ingrowth. Previous studies showed the optimal pore size to promote bone growth ranges from 250-425μm and 200-300μm with a minimum pore size for vasculature ingrowth [51], [52], [56]. Specifically, lattice structures are extensively researched for biomedical applications, driven by their structural characteristics and adjustable mechanical properties [58]. Two lattice configurations were designed and engineered: a triply periodic minimal surface (TPMS) and a stochastic structure using the Voronoi tessellation method. TPMS lattices are uniform, continuous, and periodic in three independent perpendicular directions, resulting in greater interconnectivity, while Voronoi stochastic lattices mimic the non-uniformity and randomness of bone [61], [78], [79], [80]. Song et al. [81] investigated the TPMS gyroid structure, and Du et al. [82] the Voronoi tessellation method with designed porous titanium structures of 30% and 48.24% porosity and 500μm and 512μm pore sizes, effectively reducing the elastic modulus to 65 ± 5.90GPa and

2.59GPa. In most studies, as seen in previous studies, the constructs are cubes, while dental implants are cylindrical. Thus, it is necessary to consider the geometrical differences across various studies. While increasing surface area for enhanced cell attachment, porous materials compromise mechanical strength, impacting their ability to withstand physiological loading [59], [63]. To address the trade-off between porosity and mechanical integrity, a porous structure is designed with the incorporation of channels leading to a dense core. This design approach aims to provide the necessary strength to withstand physiological loading while enhancing biological performance [64].

Lattice structures are highly complex and have intricate internal geometrical porous channels that conventional manufacturing methods struggle to meet the demands of porous designs crucial for implant development. Conventional manufacturing methods include subtractive manufacturing techniques such as casting, forging, and extrusion. These conventional methods can be costly because of the material waste, and the patient-specific needs of implants can be costly. Additive manufacturing (AM) has emerged as a revolutionary technology, overcoming the limitations of conventional subtractive manufacturing methods. 3D printing enables the manufacture of complicated parts with hollow structures that cannot be achieved with other traditional methods The advantages of AM lie in its ability to produce intricate, patient-specific designs without material waste, making it particularly cost-effective for implants. With the recently developed additive manufacturing processes, manufacturing of such lattice structures became achievable at high precision of executing a porous design. Additive manufacturing, colloquially known as 3D printing, uses a bottom-up approach to alleviate geometric design constraints [72].

Laser Powder Bed Fusion is a notable technique in AM, specifically employed in the medical implant field. SLM, in particular, offers the capability to create complex structures with high precision, maintaining density and enabling the production of 3D porous scaffolds and patient-specific medical devices. Laser Powder Bed Fusion, a widely used powder bed fusion process, utilizes a laser beam to selectively melt metal powders layer by layer, requiring careful tuning of various process parameters. Specifically, selective laser melting (SLM) can produce complex shapes from computer-aided design (CAD), such as porous structures and internal geometries, while maintaining high density, and machine parameters can be manipulated to induce surface roughness [77]. Laser powder bed fusion is the most commonly used additive manufacturing technique for metals and tissue engineering powder bed fusion.

However, challenges persist in AM, notably the occurrence of keyhole pores and lack of fusion. Uncontrolled porosity, influenced by machine parameters like laser power and scan speed, can result in unintended defects. Keyhole pores, spherical and less than 100µm in diameter, and lack of fusion pores can emerge based on energy density variations during printing. These factors necessitate a thorough investigation to achieve controllable porous structures, especially when fabricating implants for biomedical applications. This is because pores with sizes less than 100µm are attributed to the keyhole and lack of fusion effects during printing and do not significantly affect cell growth. Pores with sizes less than 20µm are categorized as gas pores, considered a limitation of additive manufacturing [48]. These pores are typically formed during printing and have minimal impact on cell growth. Machine parameters can control these effects. The combination of the process parameters in selective laser melting can result in induced porosity during printing. In the case of manufacturing scaffolds for biomedical dental implants, the induced porosity is unfavorable. The ultimate goal is to produce a porous interconnected architecture as designed in the CAD model with high controllability. The energy density of the process parameters controls the amount of porosity. There exists two main types of induced porosity, lack of fusion where the energy density is high, and keyhole pores where the energy density is too low. Depending on the laser parameters and machine the optimal parameters for each materials varies from machine to machine. Keyhole pores are formed when there is… and are usually spherical and 100μm or less in diameter. Lack of fusion pores is when the energy density is too… causing a lack of fusion where the pores are non-uniform in shape and larger.

This work investigates the manufacturability of the Voronoi stochastic, TPMS solid gyroid, and TPMS sheet gyroid porous architectures. The study is intended to conduct a comparison between the pore architecture characterization of two TPMS gyroid variants and Voronoi stochastic structure. The design criteria of the lattice structures are based on the properties of trabecular and cortical bone. The design criteria include an open cell, interconnected, porous architecture leading to a dense core. The stiffness mismatch caused by the difference in the elastic modulus of bone is the result of the induced pores. The interconnectivity of the pores serves as channels for the transport of nutrients, while the dense core will help maintain the mechanical integrity. The effects of the machine parameters in combination with the porous architecture on part quality and resolution were studied to establish a set of limitations and criteria for porous architecture designs for scaffolds. First, a study on the resolution of the machine and its ability to produce a porous interconnected structure starting with 50μm was analyzed. After the limitations and criteria for the machine were set, the TPMS solid gyroid, TPMS sheet gyroid, and Voronoi stochastic structures were printed to gain insight into the highest-resolution porous architecture. This study shows that 50-150μm pore size of the Voronoi stochastic structure is unattainable due to the complexity of the algorithm in creating the porous architecture. The two variants of the

TPMS gyroid structures showed to have more uniform interconnectivity which is more favorable for cell growth. The results suggest that the TPMS solid gyroid is the optimal porous architecture for manufacturing.

3.2 Methods: Porous Architecture Design and Characterization of Additively Manufactured Scaffolds

The material selected for this study is Ti6Al4V which is the most common alloy used for dental implants because of its high biocompatibility. The requirements for the Ti6Al4V dental implant are generated by the necessity to match its stiffness (Elastic Modulus) with the stiffness of the bone surrounding the implant formed of a trabecular and cortical structure. An estimation of the trabecular and cortical bones stiffness is presented by Farag et al. [16] and Misch et al. [15] which will be used as target values for the designed elastic modulus and the pore characteristics are applied in the proposed lattice structures, shown in Figure 3.2. Lattices are a three-dimensional structure made up of pores interconnected by struts to fabricate structures that are interconnected and controllable pore sizes. There exist periodic and random lattices, and in both cases could achieve interconnectivity and controllable pore sizes and porosity. The fabrication of the lattice structures is achieved using additive manufacturing, specifically SLM, however the intricate microporous structures presented a challenge, so significant attention was given to the design for manufacturability.

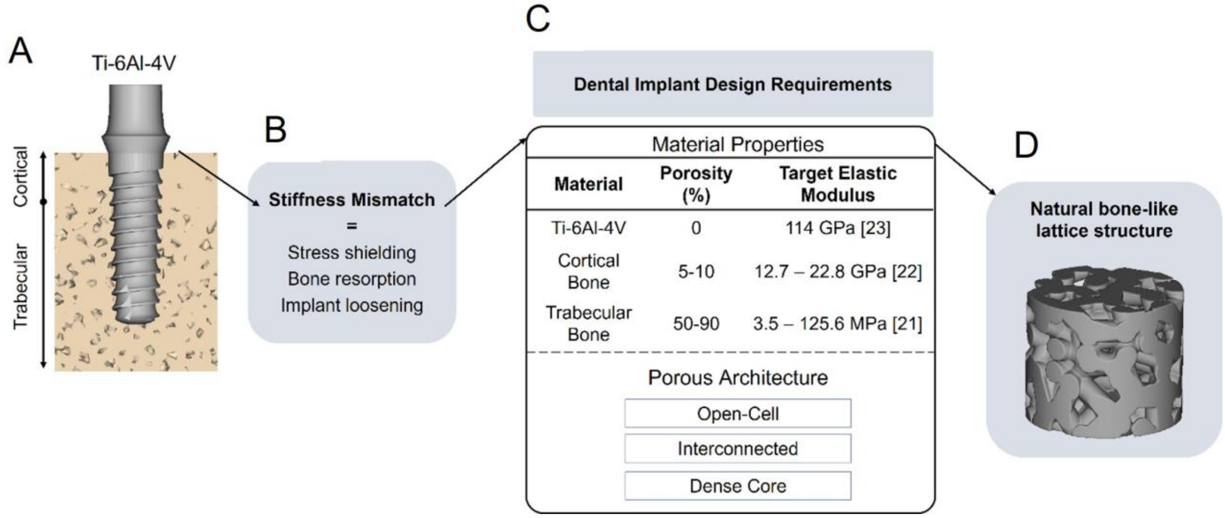

Material	Porosity (%)	Target Elastic Modulus
Ti-6Al-4V	0	114 GPa [23]
Cortical Bone	5-10	12.7 – 22.8 GPa [22]
Trabecular Bone	50-90	3.5 – 125.6 MPa [21]

Figure 3.2: Design methodology of the porous dental implant. (A) The titanium alloy dental implant is in contact with cortical and trabecular bone; (B) the stiffness mismatch results in stress shielding; (C) the target design requirements include matching the elastic modulus; (D) Natural bone-like porous architecture.

3.2.1 Methods for Modeling of Porous Architectures

Three lattice methods were carefully selected to achieve a structure that closely replicates natural bone. These methods include the Voronoi stochastic structure, solid network gyroid TPMS, and sheet network gyroid TPMS, all designed using nTopology v3.25.3.

A triply periodic minimal surface (TPMS) can be defined as an approximation of equations, which are a set of trigonometric functions, for a periodic implicit surface. TPMS structures have a mean curvature of zero and are triply periodic because they are repeated in three coordinates. TPMS structures are favorable in biomedical applications because of their nature-inspired lattice found in biological cubic membranes, exoskeletons of beetles, and butterfly wings [2]. In this research, we only consider the gyroid TPMS structure because it has a larger surface area enabling smoother cell penetration resulting in higher permeability and superior cell viability in comparison to other TPMS structures [4], [5]. Not only this, but the Gyroid structure exhibits high mechanical strength [4], which is desired to be able to withstand physiological loads while promoting the ingrowth of bone. TPMS structures can be categorized into two distinct groups, solid and sheet network structures. These categories are characterized by their respective mathematical models described in equations 1 and 2 by applying a wall thickness to the gyroid surface. The design of the pores structures depends on user-defined values for the geometrical parameters L, the unit cell size applied in the x-y-z cartesian coordinates direction, and c, the isovalue constant that controls the wall thickness [60]. Equation 1 models the solid network gyroid where the thickness is exclusively applied in one direction, either $\varphi(x, y, z) < c$ or $\varphi(x, y, z) > c$ and equation 2 models the sheet-network gyroid where c is simultaneously applied in both directions[60], [83].

$$\varphi_G \equiv sin\left(\frac{2\pi}{L}x\right)\cos\left(\frac{2\pi}{L}y\right) + sin\left(\frac{2\pi}{L}y\right)\cos\left(\frac{2\pi}{L}z\right) + sin\left(\frac{2\pi}{L}z\right)\cos\left(\frac{2\pi}{L}x\right) = c \quad (3.1)$$

$$\varphi_G \equiv sin\left(\frac{2\pi}{L}x\right)\cos\left(\frac{2\pi}{L}y\right) + sin\left(\frac{2\pi}{L}y\right)\cos\left(\frac{2\pi}{L}z\right) + sin\left(\frac{2\pi}{L}z\right)\cos\left(\frac{2\pi}{L}x\right) = \pm c \quad (3.2)$$

First, the unit cell is defined by two values, L and c, and the unit cell is then applied to a defined geometric space periodically in the x, y, and z directions. The thickness constant varies the wall thickness between the pores and is defined as either c >0 or c <0. Figure 3.3 shows the effects of varying the thickness constant and unit cell size and applying it to a finite 10 x 10 x 10mm cubical space. In Figure 3.3 (B-D) L is increased at three different values 1mm, 1.5mm and 2mm and keep the thickness constant, c, at a constant value of zero. In this case, the wall thickness and pore size are increased, and the periodicity of the unit cell is applied to the cube. On the other hand, in Figure 3.3 (E-G) when the wall thickness constant, c, increases and the unit cell size is kept at a constant value, pore size decreases and periodicity is constant. When c>0, pore size is increased and c>0 increases pore size.

Increasing L increases the size and periodicity of the pores of the unit cell in the x-y-z direction, and increasing c increases the wall thickness which decreases pore size. The TPMS unit cell created using the equations is then assigned to a specific finite shape to induce porosity as seen in Figure 3.3.

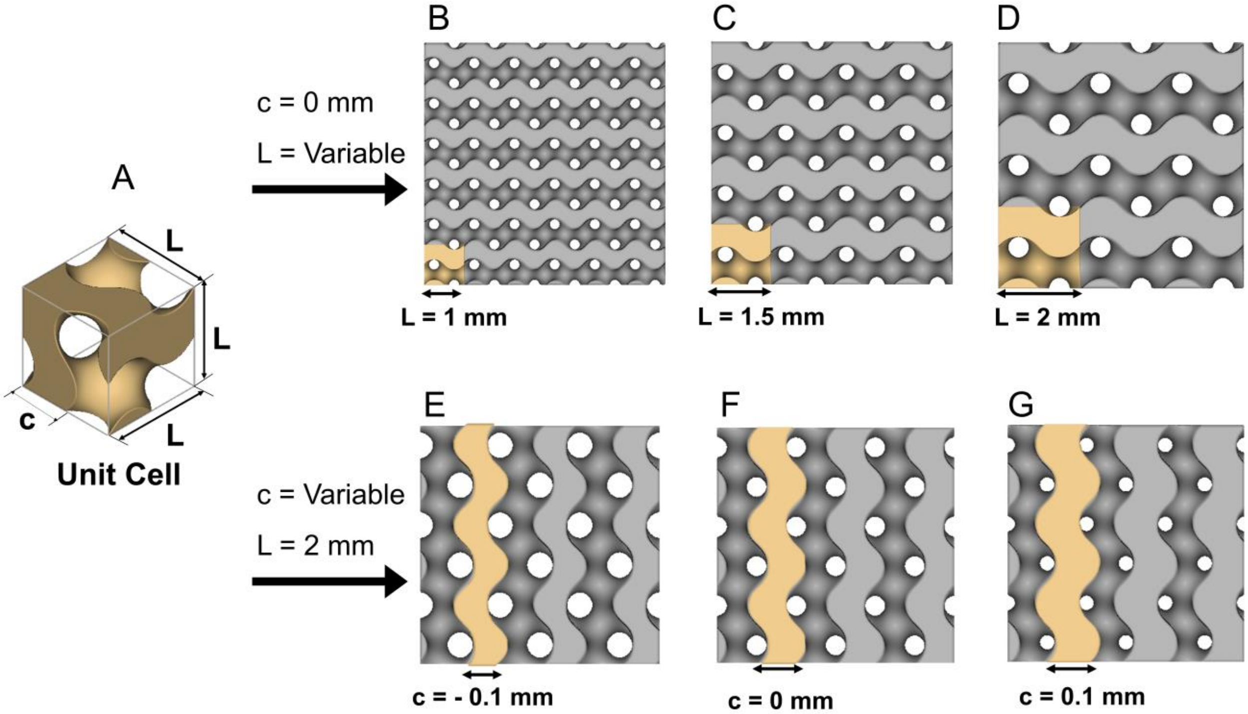

Figure 3.3: TPMS solid gyroid structure with varying the unit cell size, L, and thickness constant, c. (A) The unit cell applied to a finite space. (B-D) Varying L in three directions and constant thickness of 0mm. (B) L is 1mm, (C) L is 1.5mm, and (D) L is 2mm. (E-G) Varying thickness constant c and constant unit cell size of 2mm. (E) c is -0.1mm, (F) c is 0mm, and (G) c is 0.1mm.

The TPMS sheet gyroid is modeled in Figure 3.4. The thickness constant is kept constant at a value of 0.15mm applied in both the positive and negative directions with varying the unit cell size, L, in the x-y-z direction. Increasing L increases the pore size and decreases periodicity. On the contrary when L is kept at a constant 2mm and the thickness constant c is varied the periodicity of the pores is kept constant with an increasing wall thickness resulting in decreasing pore size.

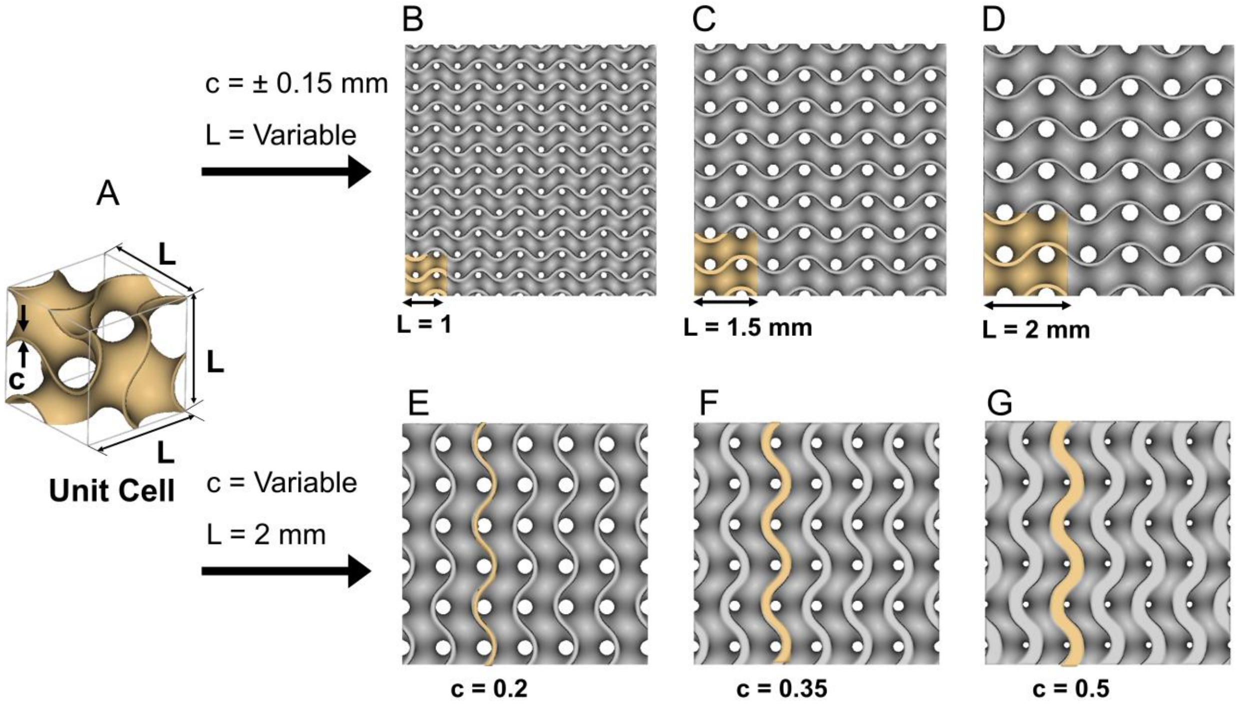

Figure 3.4: TPMS Sheet-network gyroid structure with varying the unit cell size, L, and thickness constant, c. (A) The unit cell applied to a finite space. (B-D) Varying L in three directions and constant thickness of 0mm. (B) L is 1mm, (C) L is 1.5mm, and (D) L is 2mm. (E-G) Varying thickness constant c and constant unit cell size of 2mm. (E) c is 0.2mm, (F) c is 0.35mm, and (G) c is 0.5mm.

Sheet network surfaces theoretically exhibit a higher surface area, which is conducive to cell growth, but the design is more complex than the TPMS solid gyroid. On the contrary, the TPMS solid gyroid has a simpler design more favorable for manufacturing.

Although TPMS structures offer excellent controllability and permeability, the Voronoi tessellation stochastic algorithm possesses a non-uniform, random pore distribution mimicking the design features of trabecular bone [62]. The governing equation supporting the algorithm to produce the stochastic Voronoi tessellation method is shown in equation 3 [82], where $P_1, \ \ldots, P_n$, is the set of distinct seeds in a finite region, $V(P_i)$ is the Voronoi polygon associated with P_n, and D is the Euclidean distance between the points.

$$V(P_i) = \{P \mid D(P,\ P_i) \ \le\ D(P,\ P_j),\ i\ \ne\ j,\ and\ i, j\ = 1,2,3,\ \ldots, n\} \quad (3)$$

The Voronoi tessellation method first randomly distributes seeds in a selected region. The seeds are then encompassed by polygons continuously growing outward until they intersect [61]. The lattice is then thickened to create a 3D structure once applied to a 3D finite space, the design process is shown in Fig.3.5.

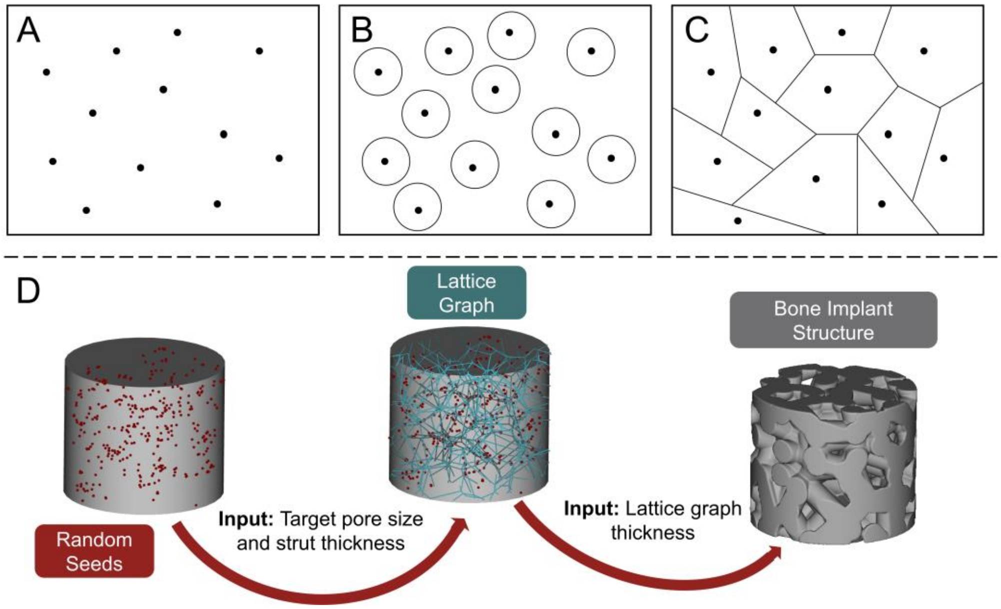

Figure 3.5: (A-C) The representative 2D application of the Voronoi tessellation algorithm. (A) a set of seed points randomly distributed to a finite space, (B) circles encompassing each seed point increase outwards until they intersect, and (C) a set of polygons. (D) Representation of the Voronoi tessellation method applied to a 3D finite geometry. The red points represent the random seed points applied to the cylindrical structure, the input target pore size and strut thickness generates a lattice graph. The lattice graph thickness input fabricates a random porous architecture.

3.2.1.1 Geometric Characterization of Pore size and Porosity

In all cases, TPMS and Voronoi structures, the chosen porosity was influenced by the dimensions of the cylindrical structure relative to the size of dental implants to maintain the load bearing strength while inducing interconnected channels. Porosity is calculated using equation 4, where P is the porosity volume fraction, V_{pores} is the volume of the porous scaffold structure, and V_{solid} is the volume of the fully dense structure [84].

$$P = \left(1 - \frac{V_{pores}}{V_{solid}}\right) x\ 100 \qquad (3.4)$$

Measuring pore size has gained some controversy, there is no existing standard or unified definition used for pore diameter available [85]. There exist two different methods for defining pore dimensions, 3D and 2D. The first form of measurement is based on the maximum sphere size that can be placed within the pores without intersecting the wall. The second is the diameter of the pore in a 2D plane, which is the measurement of the 2D circle. The maximum space for a cell to grow within the porous structure differs. We define pore size for both the Voronoi stochastic and TPMS structures in the three-dimensional space, because of the fluid and cell flow that exists within the pores. It is defined as the maximum space for a cell to grow in the direction of fluid flow, this can be seen in Figure 3.6 and Figure 3.7. The pore size was calculated by the largest sphere size that could fit into the pore without intersecting the structure in three dimensions. Some literature uses the unit cell size in regular structures to characterize the dimensional parameters, in this research we use both. In the case of the TPMS structure, the unit cell is rotated in an isometric view in the direction that flow will be traveled. The diameter of the void D_p is taken as the pore size from the unit cell that will be applied to the finite structure. The diameter is measured using the ruler in the nTopology software and filling the pore with a sphere to validate the pore size as seen in Figure 3.6. The limitation here is that there is no function to calculate pore size except manually from measuring the pore size using the ruler in the software.

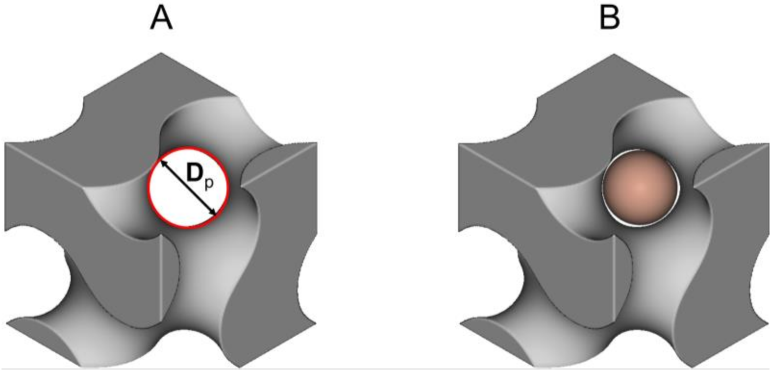

Figure 3.6: (A) Measurement of pore size, D_p , from the TPMS gyroid unit cell in the position of the path of flow and (B) filled with a sphere to validate the pore size.

The Voronoi stochastic pore size is calculated using an existing function in the nTopology software. First, seed points are mapped within each lattice graph, a point map is generated with a corresponding diameter. Spheres are applied to each mapped point for a visualization of the assembly of pores, shown in Figure 3.7.

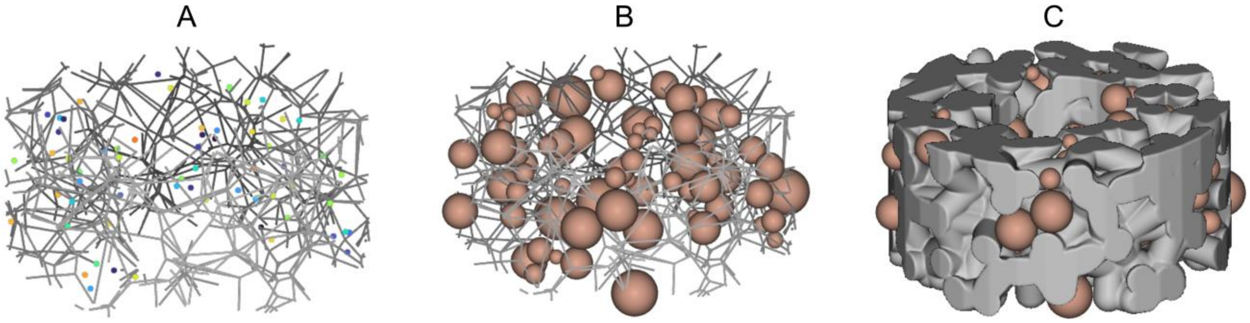

Figure 3.7:Stochastic Voronoi pore size calculation (A) each pore is mapped with a point in the lattice structure, (B) the point generated into spheres to fill the void spaces. (C) 3D Voronoi scaffold and mapped spheres.

The pore size for the Voronoi stochastic structure has an average pore size of the targeted value, because of its randomness in nature. This is one limitation that exists with the design of the Voronoi stochastic structure, there will be a minimum and maximum pore size set as the upper and lower limit from the average and targeted value. The targeted pore size is taken as the measurement of the pore size measurement.

3.2.2 Modeling of the Porous Scaffolds for Manufacturability

Three different studies were conducted to analyze the manufacturability and resolution of the porous architectures. The first was a preliminary study conducted to understand the effects of the SLM process parameters on part quality. Based on the optimal process parameters the Voronoi stochastic architecture was analyzed for three different pore size, 50µm, 150µm, and 250µm. This was conducted to study the lowest pore size that could be achieved while maintaining interconnectivity. The third study was aimed at comparing the sheet gyroid TPMS, solid gyroid TPMS, and Voronoi stochastic structure maintaining a designed a pore size within 200-250µm. Serving as a reference, Figure 3.8 shows a summary of the design process of the two variants of the TPMS gyroid unit cells and the Voronoi stochastic structure lattice graph applied to the intended geometry a 5mm diam x 3mm thickness cylindrical construct and a 2mm dense core.

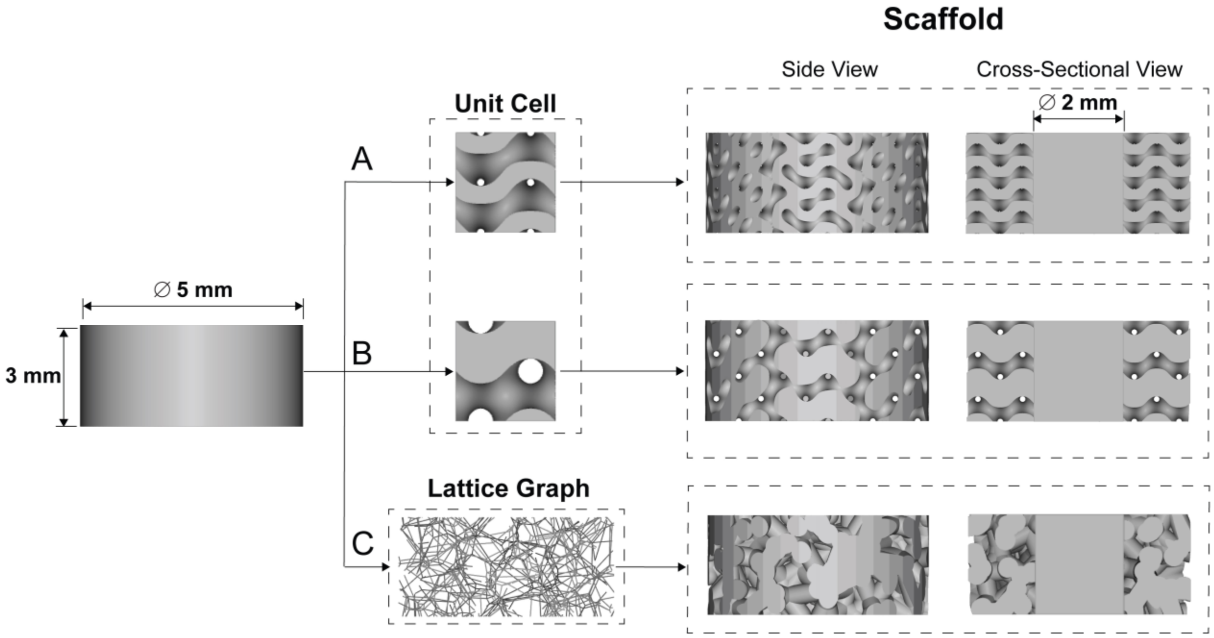

Figure 3.8:CAD scaffold modeling process of the unit cells and lattice graph of each porous architecture applied to a cylindrical geometry with channels leading to a 2mm dense core: (A) TPMS – Sheet Gyroid, (B) TPMS – Solid Gyroid, and (C) Voronoi – Stochastic.

3.2.3 Methodology for the Fabrication of Lattice Structures and Part Quality Validation

The parameters of the machine can induce undesirable pores, and the complexity of the lattice structure can be a limitation of the machine's capabilities. First, the optimal process parameters are set up in the TruPrint 1000 SLM machine for manufacturing the CAD design scaffolds, and the manufactured scaffolds are then scanned using micro computedcomputed tomography for design validation. The criteria for design validation encompassed interconnectivity, manufactured pore size, manufactured porosity, and the frequency distribution of pores. First, a range of varying pore sizes and porosity for the Voronoi stochastic structure were designed, fabricated, and analyzed to indicate the optimal pore size for printing and cell infiltration through an interconnected channel.

The constructs are designed using nTopology, inputted into the Materialise Magics 25.0 pre-processing software as an STL file, and printed with the TruPrint 1000 SLM machine in an argon environment. The resolution for the machine is 30µm, which correlates to its 30µm laser beam diameter. The Ti6Al4V titanium alloy powder had a particle distribution of 15-45 µm. The process parameters, specifically the energy density, play a role in the quality of the parts printed. Two printing phases were conducted to analyze the process parameters and the smallest printable pore size. In the first printing phase, a scan speed of 200mm/s, hatch spacing of 60µm, laser power of 80W, and chess hatch style were used to print 50µm pores. The results from these process parameters proved to be inefficient in terms of print time and quality of parts. The optimized process parameters for Ti6Al4V ELI Grade 23 were obtained from the TruPrint manufacturer which consisted of a scan speed of 1200mm/s, laser power of 80W, hatch spacing of 60µm, and stripes hatch style. The outcomes from both phases were compared. Table 3.1 shows the two printing parameters that were used.

Table 3.1**:** TruPrint 1000 SLM print parameters for fabrication validation.

Print Parameter	**Scan Speed (mm/s)**	**Hatch Spacing (µm)**	**Laser Power (W)**	**Hatch Style**	**Beam Diameter (µm)**
1	200	60	80	Chess	30
2	1200	60	155	Stripes	30

The quality and resolution of the printed scaffolds are evaluated using micro computed tomography (micro-CT) scanning using the Zeiss XRadia Versa 520 3D X – ray Microscope, seen in Fig.6. The TPMS solid and sheet gyroid, and the Voronoi stochastic cylindrical samples, with a diameter of 5mm and length of 3mm, were scanned and each data set has a voxel size of 7.49µm and resolution of 14.98µm.

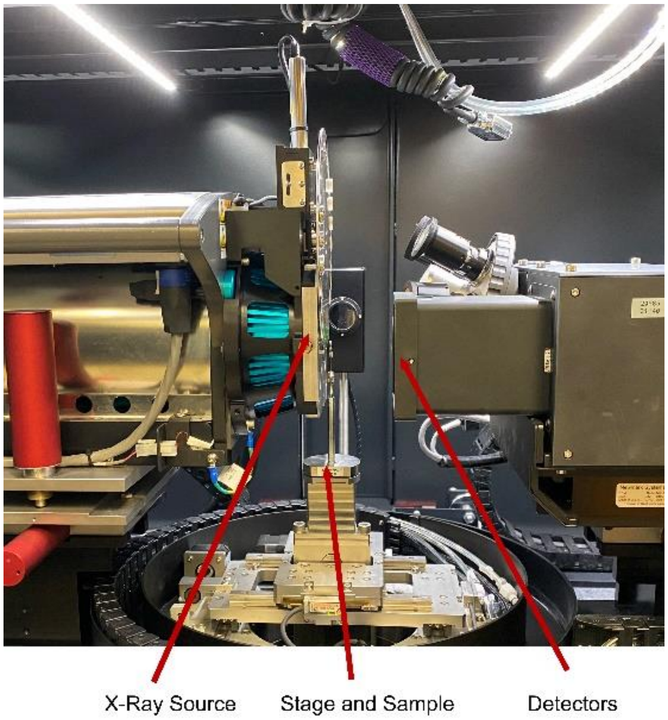

Figure 3.9: Zeiss XRadia Versa 520 3D X – ray Microscope setup with the samples mounted on a stage between the X-ray source for scanning and detector for magnification adjustments.

Subsequently, the resultant CT scan files underwent analysis using DragonFly ORS and Bruker CT-Analyzer software, yielding measurements for pore size, porosity volume fraction, pore size distribution, pore connectivity, and 3D models of the geometric structures. The 3D models were inverted in DragonFly to generate solid – modeled pores, enhancing accuracy for analysis in the computational fluid dynamics simulation.

3.3 Results and Discussion

3.3.1 Parameter Effects on Part Quality

Print parameters of selective laser melting can cause unintended pores based on the combination of laser power and scan speed, also known as energy density. Figure 3.10 shows the preliminary results from printing with parameters chosen based on previous works. The porosity percentage was almost doubled, and the average porosity size was almost double the target pore size. Referring to Table 3.1 with the two different print styles, the part quality was affected significantly. It is important to note that uncontrollable porosity can be generated based on the machine process parameters, namely the laser power, scan speed, and hatch spacing. When the scan speed is high relative to the laser power, the energy density is not sufficient to melt the powder, creating unintentional pores known as a lack of fusion pores. Alternatively, when the laser power is increased, the energy density is high, leading to pores known as keyhole pores that are spherical in shape and less than 100μm in diameter [86]. This research is aimed at fabricating controllable porous structures on the basis of mathematical models using CAD.

Qualitatively looking at the sample, the patterns of the hatch style are imprinted on the surface, the solid core has an abundance of unintended pores. In comparison to the sample designed using print style 2, the solid core has fewer unintended pores analyzed. Table 3.1 shows the difference in manufactured pore size and porosity based on the print parameters. The Voronoi stochastic structure printed with a scan speed of 200mm/s and laser power of 80W had an increase in pore size and porosity of almost double. According to a process map for the TruPrint 1000 and Ti6Al4V powder, these print parameters are in the over melting region indicating the possibility of keyhole pores [87]. Where as the Voronoi stochastic structure printed with a scan speed of 1200mm/s and 155W laser powder, the porosity was decreased and the pore size was almost within the standard deviation for achieving 50μm. According to the process map, these parameters are within the fully dense pores so the reduction in pore size and porosity could potentially be because of the complexity of achieving that low of a pore size [87].

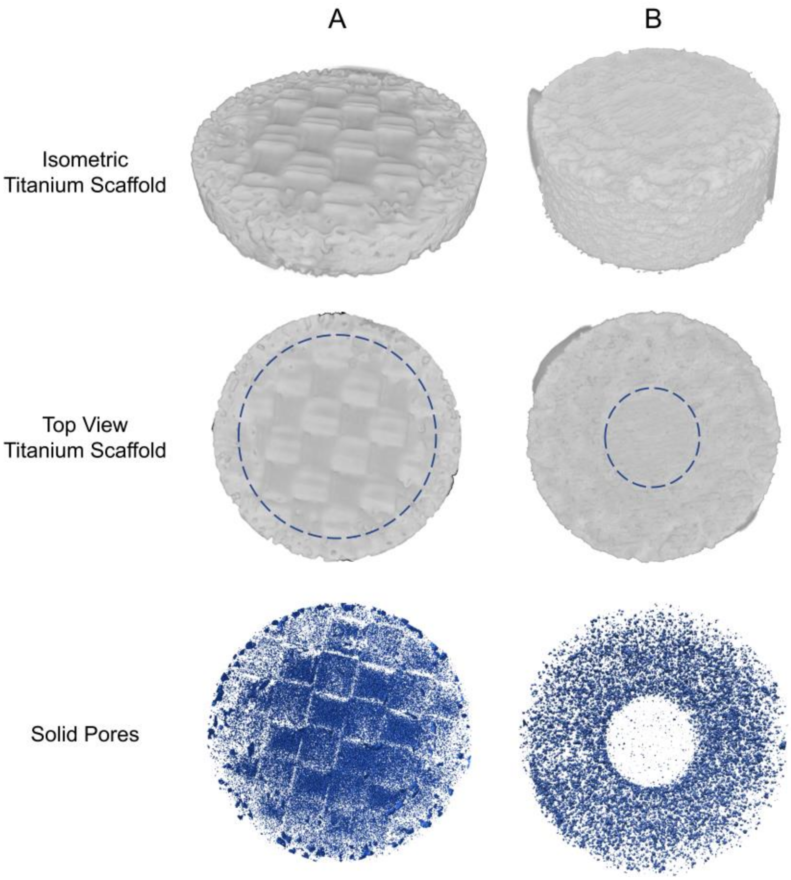

Figure 3.10: Voronoi stochastic scaffolds printed with 50µm pores showing the isometric and top view of the titanium scaffold with the solid core encircled in blue, and the solid modeled pores for a comparison of print parameter resolution. (A) 50µm Voronoi stochastic structure printed with 200mm/s scan speed and 80W laser power and (B) 50µm Voronoi stochastic structure printed with the optimal parameters a scan speed of 1200mm/s and laser power of 155W.

Table 3.2: SLM fabricated pore size and porosity of the Voronoi stochastic structures using two different print parameters.

	Designed		**SLM Manufactured**	
Design Architecture	**Pore Size** (µm)	**Porosity** (%)	**Pore Size** (µm)	**Porosity** (%)
Print Parameter 1	50	1.22	96.34 ± 11.83	2.11
Print Parameter 2	50	16.48	34.39 ± 13.57	6.09

3.3.2 Voronoi Stochastic Porous Architectural Effect on Part Quality and Interconnectivity using SLM

The pore size and architecture played a significant role in the print quality of the parts. First, a range of pore sizes for the stochastic Voronoi structure was studied. Then a range for the TPMS solid gyroid was discussed, similar for the TPMS sheet gyroid. The analysis was done through the frequency of distribution and dragonfly from micro-CT. To establish the minimum pore size for interconnectivity within the Voronoi stochastic structure, structures with 50µm, 150µm, and 250µm pore sizes were designed in nTopology and manufactured using print parameter 2 from Table 3.2. Figure 3.11 shows the CAD model of the pores with the titanium scaffold, titanium and solid-modeled pores, and just the solid-modeled pores. The solid – modeled pores in Figure 3.11 (A) and (B) for the 50µm and 150µm pore sizes, shows to have a more complex geometry with no interconnectivity compared to the 250µm structure. The capabilities were analyzed using micro-CT after fabrication.

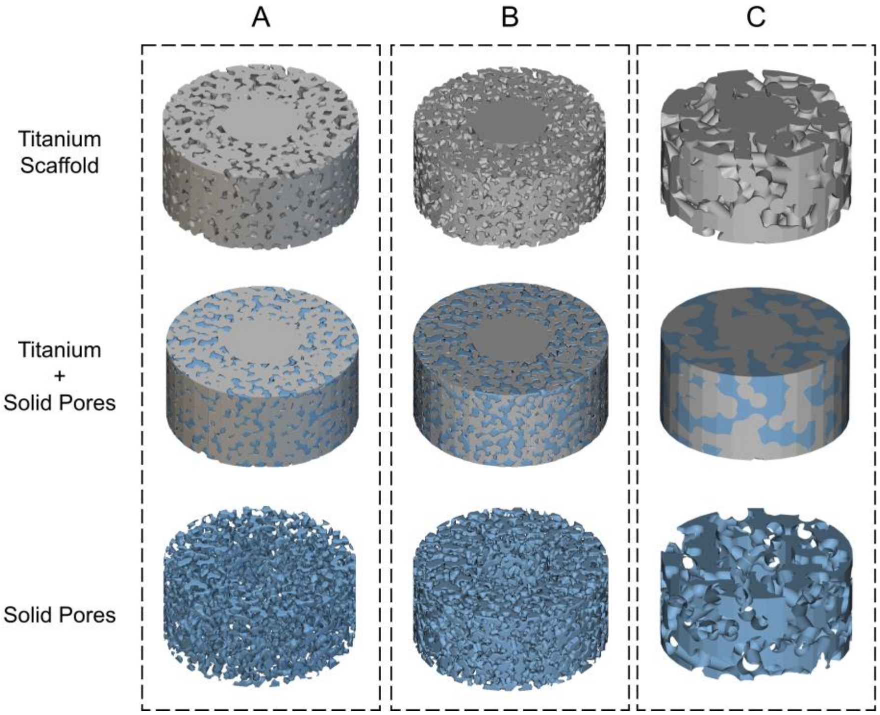

Figure 3.11: CAD models of the titanium scaffold, titanium and solid modeled pores, and the solid modeled pores for varying pore sizes of the Voronoi stochastic architecture. (A) 50µm pores, (B) 150µm pores, and (C) 200µm pores.

The solid modeled pores for the 50µm and 150µm pores in Figure 3.11 qualitatively showed to have high complexity and low interconnectivity compared to the 250µm pore size Voronoi stochastic structure. The scaffolds were manufactured and analyzed from the modeled outputs from the micro-CT scan. Table 3.3 presents the target and manufactured pore size, porosity, and micro-CT outputs. From these results, the 50µm and 150µm achieved a much lower porosity and average pore size. Figure 3.12 shows the micro-CT scan outputs. The reason for the lower manufactured porosity for the 50µm and 150µm pore sizes can be attributed to the closed pores from the result of the manufacturing increasing the chance for trapped powder particles within the pores. In Figure 3.12 (C), the 250µm designed pores were closely achieved to the designed porous structure, thus the 250µm structure was chosen to compare against the two variants of the TPMS gyroid structures.

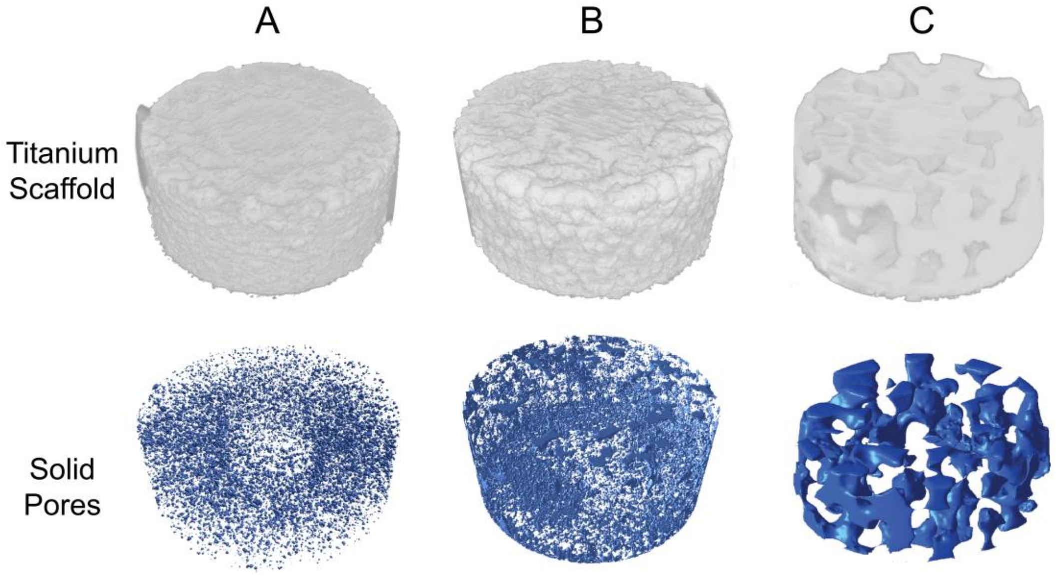

Figure 3.12: Voronoi stochastic pore size study for analysis of the resolution and interconnectivity of pores. (A) 50µm, (B) 150µm, and (C) 250µm.

Table 3.3: SLM fabricated Voronoi stochastic structures with varying pore size and porosity

	Designed		**SLM Manufactured**	
Design Architecture	**Pore Size** (µm)	**Porosity** (%)	**Pore Size** (µm)	**Porosity** (%)
1	50	16.48	34.39 ± 13.57	6.09
2	150	39.98	47.21 ± 26.30	7.91
3	250	41.59	214.90 ± 140.00	19.00

To create an equal comparison of porous architecture quality between the Voronoi stochastic structure and two variants of the TPMS gyroid structures the TPMS solid and sheet gyroid structures were designed with a target pore size between 200-250μm. The TPMS and Voronoi uses a different algorithm and technique for designing pores, explaining the range 200-250μm as the criteria for pore size. Three scaffolds were designed using nTopology, SLM-manufactured, and analyzed from the micro-CT scan outputs in DragonFly. The 250μm pore size scaffold exhibited the highest resolution of the stochastic scaffold, thus the 50μm and 150μm designs were eliminated for further analysis.

3.3.3 Part quality and Resolution Comparison of the TPMS Gyroid and Voronoi Stochastic Porous Architectures

The Voronoi stochastic structure exhibits interconnected pores at 250μm pore size. The TPMS sheet and solid gyroid scaffolds are compared against the Voronoi stochastic structure architecture for print quality and interconnectivity. Figure 3.13 shows the TPMS sheet gyroid, TPMS solid gyroid, and Voronoi stochastic SLM fabricated structures using the optimal print parameters for Ti6Al4V for the TruPrint 1000 with a 80W laser power, 1200mm/s scan speed, and 60μm hatch space. The geometry 5mm Diam x 2mm height are manufactured for similarity to a dental implant, micro-CT analysis, and for the purpose of In-vitro cell culturing. The TPMS sheet gyroid, TPMS solid gyroid, and Voronoi stochastic scaffolds were designed with a target pore size and porosity of 200μm and 51.10%, 220μm and 32.57%, and 250μm and 38.39%.

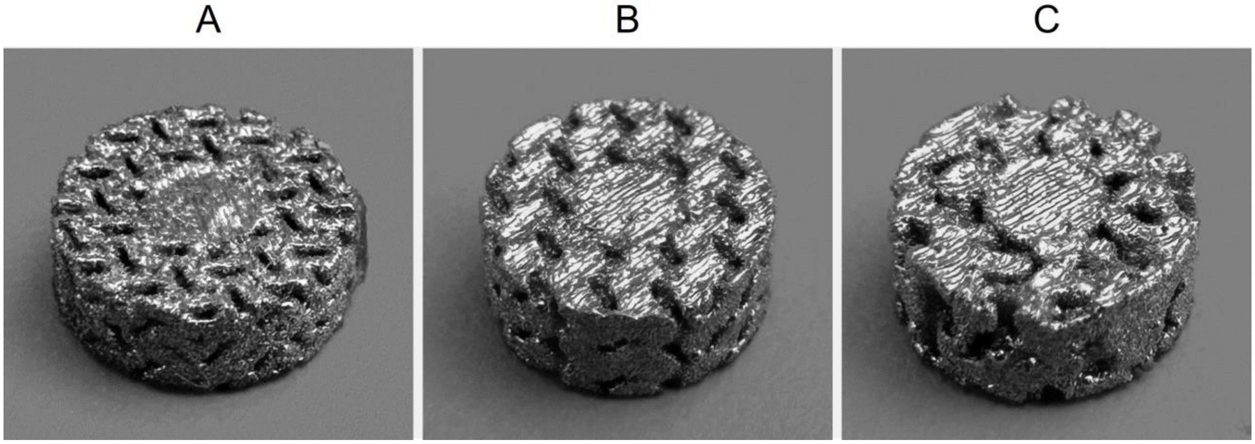

Figure 3.13: Selective laser melted scaffolds. (A) TPMS sheet gyroid, (B) TPMS solid gyroid, and (C) Voronoi stochastic

Although the TPMS sheet gyroid had the closest average pore size, the variability remained the most. Similarly, with the Voronoi stochastic structure. It is important to validate the design resolution with the outputs from the manufactured samples pore size and porosity along with the variability in pore size. Not only this, but to consider biological behavior. Figure 3.14 shows the 3D printed constructs from the micro-CT scan and the voids modeled as a solid to analyze the pore interconnectivity. Qualitatively analyzing the 3D μCT scan of the solid – modeled pores in Figure 3.14, the pores are interconnected in both TPMS structures, and the stochastic structure is not fully interconnected from the inlet to the core but has the advantage of randomness like bone. Further experiments were conducted to study the behavior of the pores.

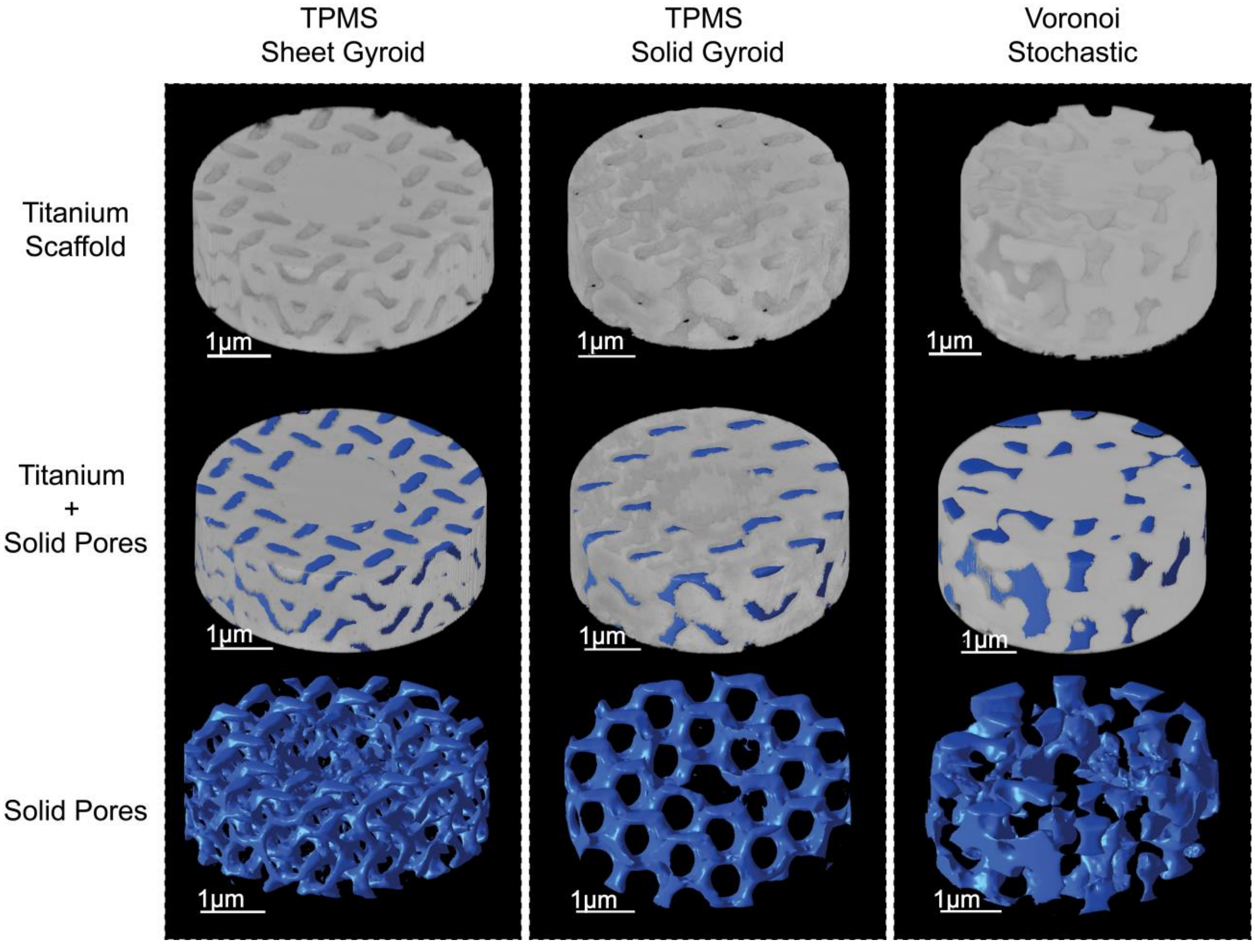

Figure 3.14: Micro computed tomography model outputs with the titanium scaffold model, titanium and solid-modeled pores, and the solid–modeled pores of the TPMS sheet gyroid, TPMS solid gyroid, and Voronoi stochastic.

Table 3.4 shows the manufactured porosity and average pore size for each design analyzed from the models in Figure 3.14. In each design, the target pore size fell within the standard deviation, but the porosity decreased from the target by 32.29% for the TPMS sheet gyroid, 12.66% for the solid gyroid, and 19.39% for the Voronoi stochastic structure. The sheet gyroid structure had the highest decrease from the intended porosity attributed to the printer's ability to produce the design's complexity. The TPMS solid gyroid was shown to have the highest resolution in terms of pore size and porosity. The precision in the design, fabrication, and overall arrangement of the interconnectivity of the pores is a crucial factor to consider in the unique micro-scale design approach for pores below 300μm in cylindrical constructs. Despite not reaching the desired porosity, the intricate porous structures achieved interconnectivity, resulting in improved biological properties compared to a fully solid structure.

Table 3.4: Comparison between the target and SLM manufactured pore size and porosity of the scaffolds.

	Target		**SLM Manufactured**	
Design Architecture	**Pore Size** (μm)	**Porosity** (%)	**Pore Size** (μm)	**Porosity** (%)
TPMS Sheet Gyroid	200	51.10	197.74 ± 91.49	18.81
TPMS Solid Gyroid	220	32.57	153.28 ± 60.92	19.91
Stochastic Voronoi	250	38.39	214.90 ± 140.00	19.00

The distribution of porosity in the complex micro-level porous designs provides valuable insights into the quality of the printing process. Understanding the distribution of porosity helps evaluate the overall performance and functionality of the printed structures. Figure 3.15 shows the porosity distribution for each scaffold, data was taken for pores within the range of 100-450μm. This is because pores with sizes less than 100μm are attributed to the keyhole and lack of fusion effects during printing and do not significantly affect cell growth. Pores with sizes less than 20μm are categorized as gas pores, considered a limitation of additive manufacturing [48]. These pores are typically formed during printing and have minimal impact on cell growth. Machine parameters can control these effects. Thus optimal manufacturer parameters were used for Ti6Al4V powder in the TruPrint 1000 to limit the undesired pores. Pore sizes ranging from 200-425μm are considered optimal for promoting cell growth. The target pore size for each design falls within the range of 200-250μm, but the distribution of pore sizes varies for each porous architecture. In Figure 3.15, the Voronoi stochastic structure exhibits a random frequency distribution of pores with no specific pore size dominating. The TPMS sheet gyroid shows a distribution centered around approximately 160μm. The TPMS solid gyroid has the least amount of randomly distributed pores, with the maximum pore size reaching 272.61μm and a distribution centered around 200μm.

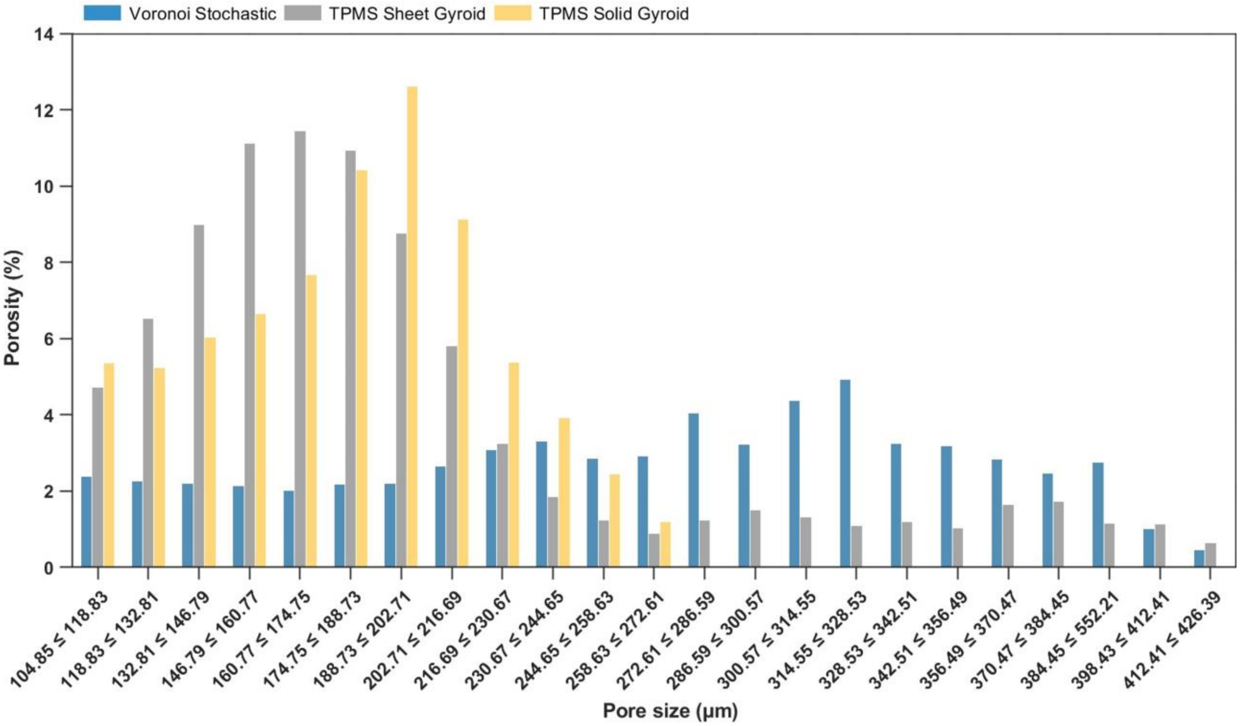

Figure 3.15: Pore size distribution of the selective laser melted Stochastic Voronoi, TPMS Sheet Gyroid, and TPMS Solid Gyroid structures from micro-CT scans.

The TPMS solid gyroid scaffold demonstrates the highest controllability level for designing and manufacturing processes, resulting in greater precision and control over the characteristics and properties of this scaffold design. Despite the intended pore size of 250μm for the Voronoi stochastic architecture, the resolution of the print was found to be the lowest based on the frequency distribution of the pore sizes. This suggests that the level of detail and accuracy in reproducing the intended pore size was not as easily achieved.

3.4 Conclusions

The main contribution of this work was to conduct a study on the print parameters of SLM printing and establish criteria and assess the quality of printing for three porous architectures. The criteria included a minimum pore size having an interconnection of pores for the Voronoi stochastic structure because of its randomness. The purpose was then to compare it against the TPMS sheet gyroid and TPMS solid gyroid for the pore size, porosity, and interconnectivity. No interconnectivity is achieved for the Voronoi stochastic structure's designed pore size of less than 250µm. Furthermore, the TPMS solid gyroid outperformed the Voronoi stochastic and TPMS sheet gyroid on the basis of print resolution. The value of the frequency distribution centered around 200µm shows the least variability in pore size when printing, and qualitatively shows the highest interconnectivity and simplicity of its design. The establishment of the optimal porous architectures based on print parameters, print quality, and the outcomes of the printed porous architectures allowed for further experimental work for in-vitro cell culturing.

In this work, we developed, assessed, analyzed, and established the optimal parameters for SLM printing for the TruPrint 1000 and the optimal porous architecture for scaffolds.

The aim of this study was to assess, analyze, and establish optimal print parameters coupled with the optimal porous architectures. It can be concluded that the print parameter 1 in Table 3.2

cannot be used and a pore size of 50µm is not practical for the interconnection of pores and enhancing cell proliferation. The results suggest that the optimal designed porosity of the two variants, solid and sheet, TPMS gyroid and the Voronoi stochastic structures optimal starts at 200µm.

Chapter 4 Validation of Enhanced Biological Properties of the Gyroid Triply Periodic Minimal Surfaces and Voronoi Stochastic Scaffolds

The biological performance of the random Voronoi stochastic lattice structure and the TPMS gyroid structures are important in the characterization of the optimal scaffold choice to replace dental implants. In combination with the manufacturability of the scaffolds, it is important to understand the behavior in an environment of cell growth. These structures are identified because of their potential to enhance cell proliferation and maintain mechanical integrity while decreasing the elastic modulus, contributing to a reduction in the stress-shielding effect. In parallel to the cell culturing, the micro-CT scans from Chapter 3 of the 200-250µm pore size scaffolds were studied for permeability. This chapter studied the in vitro cell culturing behavior of each porous scaffold characterizing the RNA quantity, indicating enhanced cell proliferation and infiltration into the construct, cell morphology, and fluorescent microscopy to understand the depths of the pores. In-vitro experiments demonstrate the possibility of improved cell attachment and proliferation, which is an early step in host-implant integration by populating the cell-titanium surface.

4.1 Introduction

Tissue engineering and regenerative medicine demand meticulous attention to the fabrication of biomimetic scaffolds, which serve as the cornerstone for successful integration between living bone tissue and implants. This integration, commonly referred to as osseointegration, plays a pivotal role in determining the longevity and functionality of implants. Within the scope of osseointegration, two critical aspects associated with implant failure are primary and secondary stability. [88], [89], [90]. Primary stability is influenced by factors including implant design, bone quality, surgical technique, and the interaction between the implant surface and the bone [89]. In the initial stages of osseointegration, contributing factors to implant failure include the micromovements of the implant during early integration with the host, pre-existing diseases in patients that negatively influence healing, decreased bone quality at the implant site, and stress shielding [3], [9], [10], [40], [41], [42]. Pre-existing diseases, including uncontrolled diabetes and periodontal disease, compromise bone healing and osteogenesis, impair osseointegration, and decrease the likelihood of long-term success of implantation [42], [43]. Additionally, specific regions of the jaw with a lower bone mass density, such as the posterior maxillary, result in a higher risk of implant failure because of the lack of interfacial stability with bone tissue during the wound-healing phase [4]. Enhancing the initial primary stability will ensure long-term success for the dental implant[91].

Primary stability, achieved during implant placement, creates a stable environment essential for effective osseointegration, subsequently contributing to the development of secondary stability [92]. The latter evolves over time, representing the gradual strengthening of the implant-bone interface through bone regeneration and remodeling [89]. During the bone remodeling phase, stress shielding is another prominent mode of implant failure occurs [93]. The phenomenon is caused by the differences in mechanical properties between the bone and titanium implant [8], [9], [10]. Although the titanium alloy Ti6Al4V Grade 23 is an industry-standard material for dental implants due to its superior biocompatibility and mechanical properties compared to other materials, its high elastic modulus relative to that of bone remains a challenge [12], [45], [46], [47]. Ti6Al4V Grade 23 with a modulus of 110 GPa significantly surpassing that of cancellous (3.5-125.6 MPa) and cortical (12.7-22.8 GPa) bone leads to uneven stress distribution, impacting the secondary stability of osseointegration during bone remodeling stages causing bone resorption and implant loosening [14], [15], [16], [18]. To address this, introducing pores into the titanium implant emerges as a viable solution. Pore incorporation reduces the elastic modulus, aligning it more closely with bone properties, thus mitigating stress shielding effects and establishing a robust interfacial connection between the implant and surrounding bone for improved osseointegration success through bone ingrowth. Hence, a thorough understanding of cell interaction in relation to dental implant architecture becomes imperative for enhancing initial primary stability, thereby ensuring long-term success for dental implants.

Research has shown that titanium implants with rough surfaces have enhanced osteoblast cell adhesion [35], which is crucial for osteogenesis directly on the titanium surface. Integrating rough and porous topographies further improves bone-to-implant contact, enhancing interfacial stability and optimizing stress distributions for effective bone reinforcement during regeneration. Scaffolds in tissue engineering act as temporary extracellular matrices, promoting cell ingrowth, proliferation, and tissue integration. offers channels for the cells to directly attach to the implant for the ingrowth of bone and facilitate the transfer of nutrients and waste within the construct [94]. Previous studies showed the optimal pore size to promote bone growth ranges from 250-425μm and 200-300μm with a minimum pore size for vasculature ingrowth [51], [52], [56]. Pore sizes in excess of 1000 μm would lower the elastic modulus dramatically and negatively impact the mechanical strength to withstand physiological loads [63]. Pores that are excessively small similarly occlude vasculature ingrowth and cell migration into the construct, leading to void spaces, negatively impacting integration, and leaving potential surface areas for bacterial infection. While porous materials increase surface area, favorable for cell attachment, however, they concurrently reduce mechanical strength [59], [63]. To address the trade-off between porosity and mechanical integrity, a porous structure with the incorporation of channels leading to a dense core is proposed. This design approach aims to provide the necessary strength to withstand physiological loading while enhancing biological performance [64].

Suitable pore architecture, including size, porosity, geometry, interconnectivity, and curvature is critical for increasing cell ingrowth. Lattice structures are extensively researched for biomedical applications, driven by their structural characteristics and adjustable mechanical properties [58]. Stochastic and triple periodic minimal surfaces (TPMS) lattices have garnered extensive attention in biomedical applications due to their structural characteristics and adjustable mechanical properties. TPMS lattices are uniform, continuous, and periodic in three independent perpendicular directions resulting in greater interconnectivity, while Voronoi stochastic lattices mimic the non-uniformity and randomness of bone [61], [78], [79], [80]. TPMS gyroid structures, characterized by low surface curvatures and narrow curvature distributions, possess straightly opened channels, resulting in higher permeability [95], [96]. Recent studies have highlighted the high permeability and cell proliferation conditions of TPMS gyroid structures [97] These structures exhibit consistent fluid permeation, positioning them as suitable designs for tissue engineering applications [98]. Permeability, defined as the measurement of fluid passage through a porous medium, profoundly influences cell proliferation and vascularization [99]. Research demonstrates that different scaffold architectures yield varying permeability. Castro el al, conducted a study on three different TPMS structures the gyroid, Schwarz diamond, and Schwarz primitive all designed with 70% porosity. This study showed that although they are all TPMS structures and designed with the same porosity, the architecture affected the surface area and as a direct result affect the permeability performance concluding that all three structures had varying permeabilities [100]. This agreed with another study showing that comparing the same geometry with lowering porosities results in lower permeability, however, comparing different geometries the lower porosity levels did not correlate to a lower permeability [98]. Among the TPMS structures exist two variants, the sheet and solid structures. Sheet based TPMS gyroid structures exhibit a higher surface area which is more conducive to cell growth [101]. Although theoretically this would coincide with better cell performance, in-vitro cell culturing experiments are needed to validate this claim. The sheet based gyroid is more complex in nature than the solid gyroid which could in turn contribute to a lower resolution structure, which would not relate to that claim. It is still not clear whether the TPMS sheet gyroid would outperform the solid gyroid and in turn compare the better variant of the two to the random Voronoi stochastic structure. On the other hand, Kiselevskiv et al. and Liang et al., found that the Voronoi stochastic models with irregular structures exhibit favorable cytocompatibility, enhanced osteoblast proliferation, and differentiation, mimicking fluid behavior akin to reconstructed cancellous bone and outperforming regular periodic structures [102], [103], [104]. Irregular porous structures with varying pore shapes have demonstrated the ability to promote osteoblast proliferation and differentiation. Understanding these structural intricacies is vital for comparing biological behavior.

In this work the Voronoi stochastic structure, sheet gyroid TPMS, and solid gyroid TPMS scaffolds designed with a target pore size of 200-250μm and 30-50% porosity with a solid core using CAD and fabricated with Ti6Al4V ELI Grade 23 powder using the selective laser melting additive manufacturing technique. The biological behavior of the scaffolds were investigated through in vitro cell culturing to analyze the response of cells to different curvatures and geometries. The RNA quantity, cell morphology using SEM, and fluorescent confocal microscopy to output the cell penetration through the pores were extracted after cell culturing. The SLM manufactured samples were scanned using micro computed tomography (micro-CT) to assess the permeability of the manufactured samples virtually using computational fluid dynamics (CFD). These experiments demonstrate improved cell attachment and proliferation, which is an early step in host-implant integration by populating the cell-titanium surface in relation to the existing fully dense structures. The objective of this research was to choose the optimal porous architecture based on permeability, interconnectivity, and cellularization, comparing the performance between the two variants of TPMS gyroid and the random Voronoi stochastic architectures.

4.2 Experimental Methods for Evaluating the Biological Performance of the Porous Architectures

The TPMS sheet gyroid, TPMS solid gyroid, and Voronoi stochastic scaffolds from Chapter 3 were tested for their performance in a biological context. The scaffolds are cell cultured in-vitro (section 4.2.2) to test the RNA quantity, pore morphology with scanning electron microscopy (SEM), and the cell trajectory within the pores using fluorescent confocal microscopy. In parallel, the solid-modeled pores from the outputs of the micro computed tomography (micro-CT) of the SLM fabricated samples are simulated in the environment of cell-culturing and human blood (section 4.2.3) to understand the permeability of each scaffold and the interconnectivity for the optimal porous architecture in a biological environment.

4.2.1 Fabrication of the Porous Scaffolds for Cell Culturing Experiments

The TPMS sheet gyroid, TPMS solid gyroid, and Voronoi stochastic structures were designed using nTopology and manufactured using the TruPrint 1000 selective laser melting

(SLM). The scaffolds exhibited a geometry of 5mm diameters, 3mm height, and a 2mm dense core. The TPMS sheet gyroid, TPMS solid gyroid, and Voronoi stochastic structures experimented in vitro, each designed with a pore size and porosity of 220µm and 51.10%, 250µm and 32.57%, and 200µm and 20%, and the fully dense structure shown in Figure 4.1. The target was to maintain a pore size within the range of 200-250µm with a porosity achieving interconnectivity, making it possible to create an equitable comparison of the environment of the cell seeding. Figure 4.1 shows the fully cylindrical Voronoi stochastic, TPMs sheet and solid gyroid, and the fully dense constructs with 5mm diameter and 3mm length which were manufactured and cell cultured. These constructs were used for cell and pore morphology analysis under SEM and extraction of RNA quantity. Figure 4.2 shows the cross-sectional isometric and front-view for the Voronoi stochastic, TPMS solid gyroid, and fully dense structures which were manufactured and cell seeded to study the cell depth penetration and trajectory through the pores. The geometry used was 2.5mm in diameter and 3mm in length.

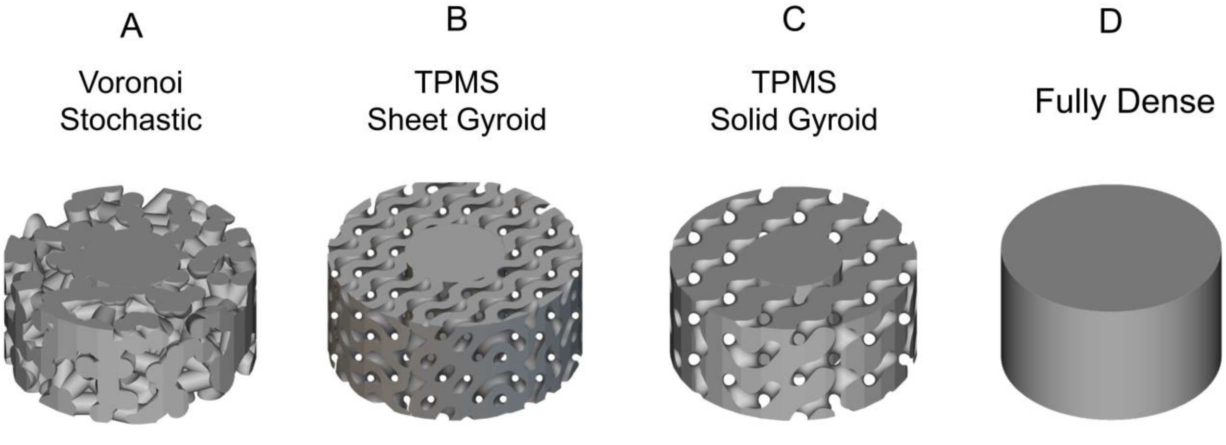

Figure 4.1: CAD models of the (A) Voronoi Stochastic, (B) TPMS Sheet Gyroid, (C) TPMS Solid Gyroid, and (D) fully dense constructs for RNA and SEM experiments.

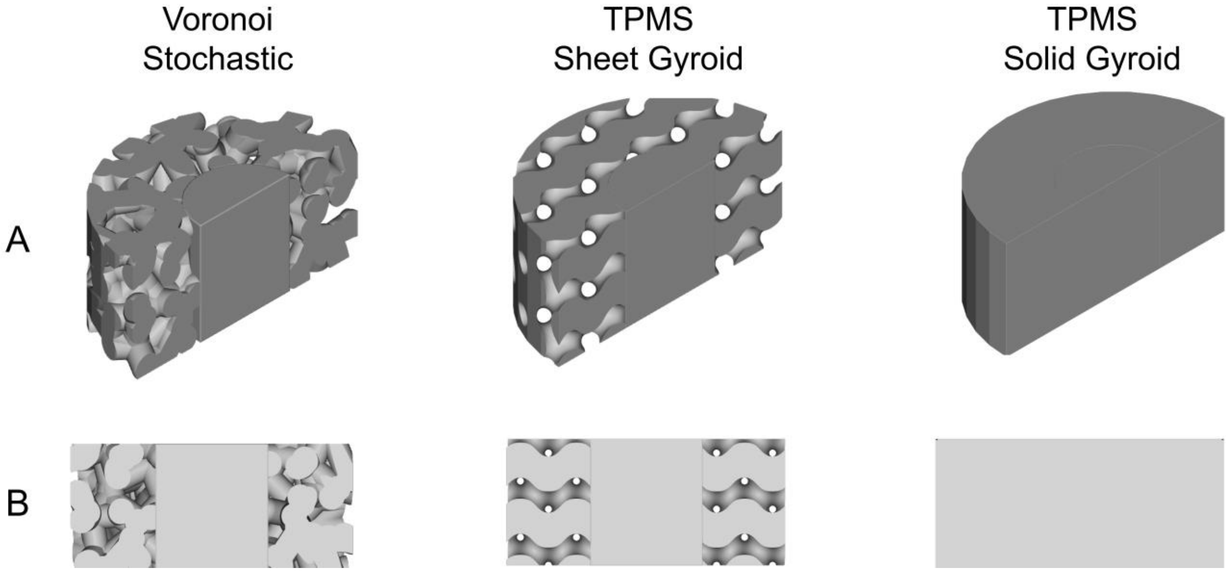

Figure 4.2: Voronoi Stochastic, TPMS Solid Gyroid, and Fully Dense constructs fabricated, cell cultured, and analyzed using fluorescent confocal microscopy for cell penetration. (A) Isometric and (B) front view of cross-sectional

The optimal TruPrint 1000 SLM parameters for Ti6Al4V ELI Grade 23 and a laser spot size of 30µm to fabricate the scaffolds are 1200mm/s scan speed, 80W laser power, and 60µm hatch spacing. The manufactured scaffolds were modeled in DragonFly from the outputs of the micro computed tomography using the Zeiss XRadia Versa 520 3D X – ray Microscope. The TPMS solid and sheet gyroid and the Voronoi stochastic cylindrical samples, with a diameter of 5mm and length of 3mm, were scanned, and each data set has a voxel size of 7.49µm and resolution of 14.98µm. The models of the manufactured scaffolds and their respective pores modeled as a solid are shown in Figure 4.3 (A-C), the TPMS sheet gyroid, TPMS solid gyroid, and Voronoi stochastic.

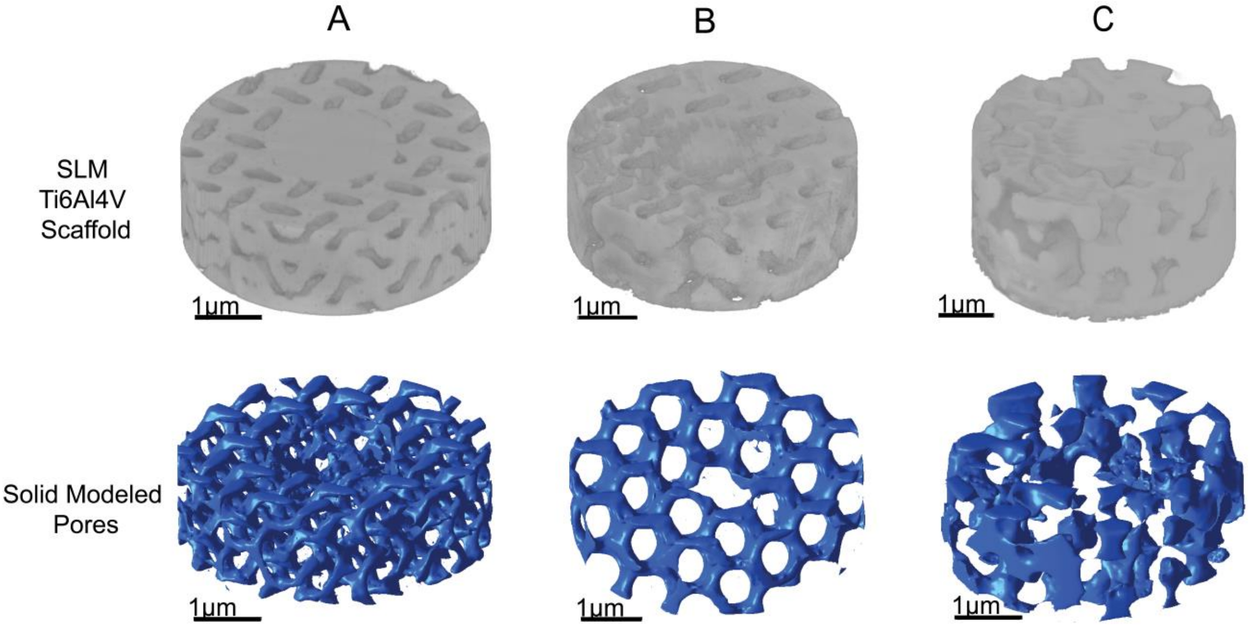

Figure 4.3: Output micro computed tomography scans of the scaffolds representing the Ti6Al4V scaffold and the pores inverted as a solid. (A) TPMS sheet gyroid, (B) TPMS solid Gyroid, (C) Voronoi stochastic.

4.2.2 In-Vitro Cell Culturing

To determine the response of mesenchymal stromal cells to these various morphologies, the 3D printed constructs were seeded with primary bone marrow stromal cells (BMSCs) isolated from 8-week-old wild-type C57BL6/J by flushing the bone marrow. Primary cells were cultured in growth media (DMEM, 10% FBS and 1,000 U of penicillin/streptomycin) in tissue-culture-treated polystyrene dishes, grown to confluence, and seeded to constructs at passage 2. Prior to cell seeding, constructs were sterilized by ethylene oxide gas. Immediately before seeding, constructs were soaked in 70% ethanol for 30 minutes, followed by washing in phosphate-buffered saline (PBS, pH 7.4) and three times in growth media. 300,000 cells were seeded per scaffold in non-treated polystyrene tissue culture dishes (n=4 per group). Cells were allowed to adhere to the Ti disks for 30 minutes at 37^{o}C, then growth media was added to the culture and changed every

48 hours. At 48 hours, Ti disks were removed from the ~~tissue~~ culture plate into a fresh vessel, and RNA was extracted with 500 uL Trizol reagent according to the manufacturer's protocol; RNA quantity was assessed by triplicate measurement of A260 using a Beckman benchtop spectrophotometer.

Scanning electron microscopy (SEM) and confocal laser microscopy were used to evaluate the distribution and morphology of BMSCs in constructs, at various time points, specimens are fixed in EM-grade paraformaldehyde for 24 hours at 4C. **Scanning Electron Microscopy**: Surface morphology was observed by scanning electron microscopy (JEOL JSM-7800 FLM) with an accelerating voltage of 5 kV and a working distance of 10-15mm. Before observation, samples were coated with gold using a sputter coater (Desk II, Denton Vacuum Inc.). **Confocal laser microscopy:** A Nikon Eclipse C1 microscope is used for all confocal imaging. A 1:1000 solution of Hoescht nuclear stain and 1:200 Alexa-Fluor 488 Phalloidin was applied and incubated for 20 minutes. Samples were washed three times before imagining them.

4.2.3 CFD Validation of the Connectivity and Permeability of the Scaffolds

The 3D solid – modeled pores from the micro-CT scan output of the SLM fabricated scaffolds were evaluated for permeability using Ansys CFX, a computational fluid dynamics software. Figure 4.3 (a-c) shows the solid-modeled pores of the manufactured TPMS sheet gyroid, TPMS solid gyroid, and Voronoi stochastic structure.

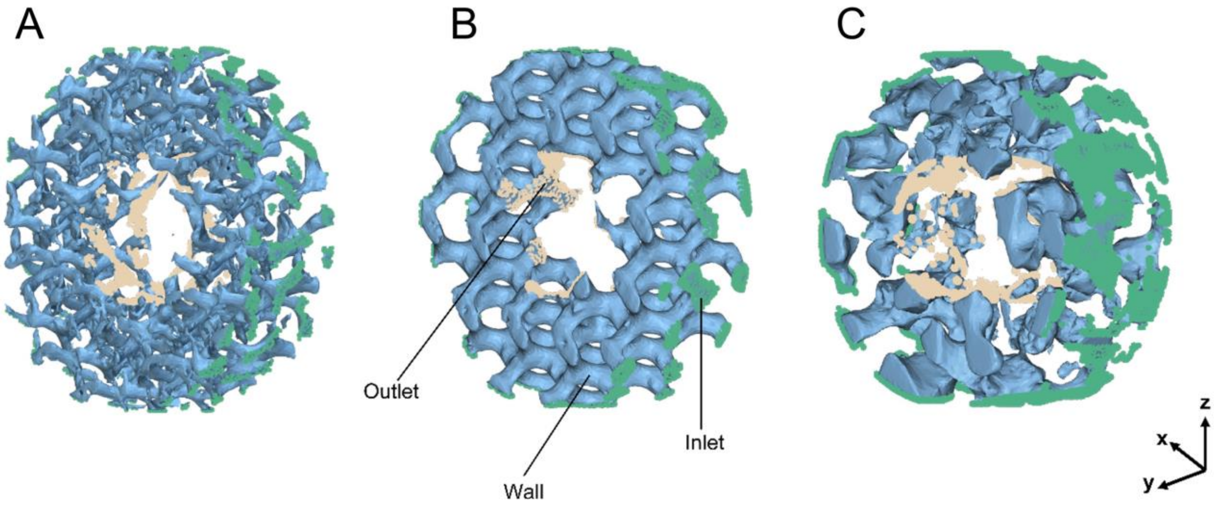

Figure 4.4**:** Diagram of the SLM solid–modeled pores from the micro computed tomography scans and the boundary conditions: (a) TPMS sheet gyroid, (b) TPMS solid gyroid, and (c) Voronoi stochastic architectures used for the computational fluid dynamics simulation to output permeability. The inlet and outlet are highlighted in green and light orange nodes, and the solid-modeled pores are taken as the wall.

A single-phase, laminar flow was assumed, and two cases were considered: a static cell seeding environment to mimic the in-vitro cell culturing experiments and a simulation of the environment of the human body. The laminar flow assumption is the resultant of the relatively slow and viscous flow through the scaffold correlating to a low Reynold's number making the assumption of no turbulence reasonable. Darcy's law shown in Equation 4.1 is used to calculate permeability where k is the permeability, Q is the volumetric flow rate, μ is the dynamic viscosity, L is the distance of fluid flow through the construct, A is the area of the construct, and ΔP is the pressure gradient from the inlet to outlet [105].

$$k = \frac{Q}{A}\frac{\mu L}{\Delta P} \qquad (4.1)$$

The density and dynamic viscosity of DEMEM, 1000 kg/m^3 and 9.3 x 10^{-4} kg/m·s, were used for the case of static cell seeding, and the density and dynamic viscosity for blood, 1050 kg/m^3 and 4 x 10^{-3} kg/m·s was considered for the environment of the human body [106], [107]. A constant velocity of 0.01mm/s was used for static cell seeding conditions, and a constant velocity of 0.7mm/s was assumed for blood [107], [108] applied at the inlet boundary condition and the outlet pressure was set to 0. The pressure gradient value, ΔP, was outputted from the ANSYS CFD simulation to calculate the permeability.

4.3 Results and Discussion

4.3.1 Biological Performance from In-Vitro cell culturing

The results from in-vitro cell culturing refined the selection for the scaffold with the optimal performance in a biological setting. First, it was determined that the TPMS solid gyroid structure has a significantly higher capacity for cell adhesion and maintenance at 72 hours based on the amount of extracted RNA (given a standardized cell seeding), as seen in Figure 4.5. RNA is a genetic material for coding proteins, in other words, it is the recipe for proteins. An increased cell number making RNA leads to increased cell activity, thus resulting in more protein being made. When early cells secrete proteins o the extracellular matrix it becomes more favorable for tissue to attach. The increased RNA cell capacity, mean there is a higher capacity for cell adhesion and further influences cell behavior. Thus, the RNA quantity gives insight into the environment and survival of the cell.

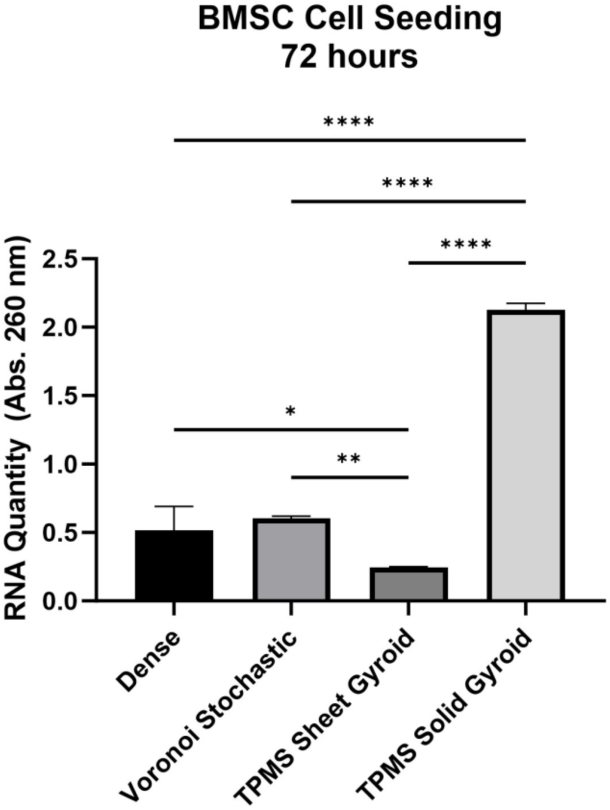

Figure 4.5: RNA quantity comparison of the dense, Voronoi stochastic, TPMS sheet gyroid, and TPMS solid gyroid at 72 hours.

To assess the surface morphology, distribution of cells, and adhesion patterns for the dense (control), TPMS solid gyroid, TPMS sheet gyroid, and Voronoi stochastic scanning electron microscopy and confocal microscopy were performed. The results from SEM for each construct are shown in Figure 4.6 for a qualitative assessment of the surface morphology and behavior of the cells. These micrographs demonstrate the TPMS solid gyroid has considerably greater pore interconnectivity, which is a critical parameter for cells to colonize the scaffold beyond the porous surface. The increased surface roughness from additive manufacturing increases material surface favorable for the adhesion of cells. It is noted that the TPMS solid gyroid exhibits a homogeneous distribution of cells throughout the construct in comparison to the TPMS sheet gyroid and Voronoi stochastic architectures, resulting in a basis for a uniform extracellular matrix formation leading to uniform tissue growth, thus explaining the observed increased RNA capacity [109], [110] . clustered cells are least favorable causing the cells to slow down. In the TPMS sheet gyroid, there is less porosity, less interconnectivity, resulting in less space for cells to exist. This indicative of the low RNA quantity and less favorable pore morphology. The results from SEM indicated there were spherical unmelted powders as a result of additive manufacturing attached to the surface of the scaffolds and pores. The cells favored this feature because of its surface roughness, curvature, and morphology where there was cell growth on and between these unmelted powders. This in turn positively affects cell adhesion and proliferation. Song et al., proposed that powders with a contact angle greater than 90 degrees are considered harmful since they are likely to fall from the scaffold and exist within the human tissue [111]. Some studies used chemical etching using hydrofluoric acid to remove these spherical powders and found no negative effect on cell attachment [111], [112], [113].

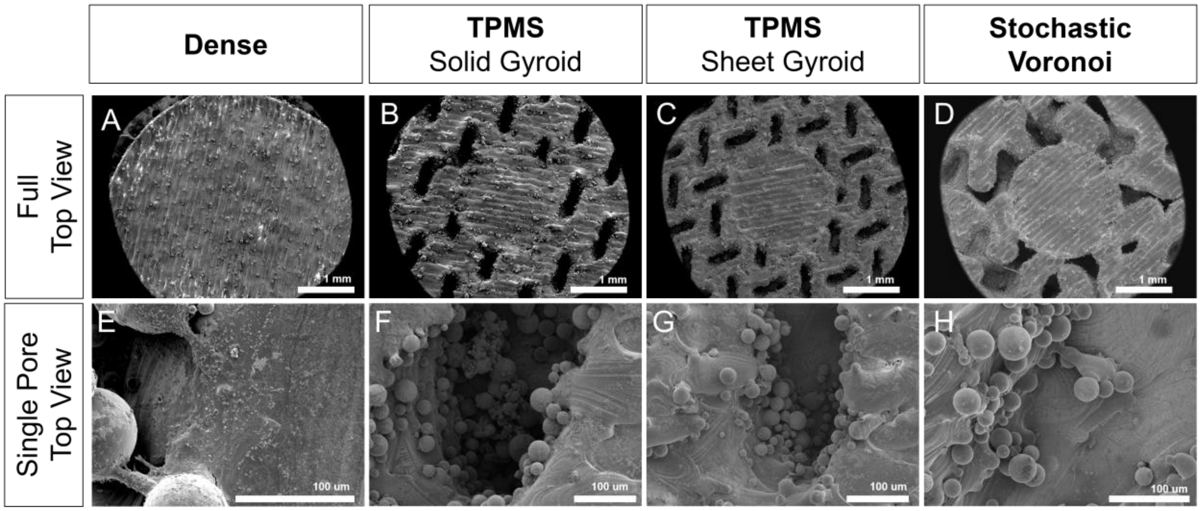

Figure 4.6: Scanning electron microscopy imaging of the full top view and single pore top view morphology. (A,E) Dense, (B,F) TPMS solid gyroid, (C,G) TPMS sheet gyroid, and (D,H) Voronoi stochastic scaffolds.

Based on the RNA extraction and SEM observation results, the TPMS sheet gyroid was excluded from the fluorescent microscopy experiments since the TPMS solid gyroid had more favorable properties. The objective was to assess and contrast the non-uniform, random stochastic Voronoi scaffold to the TPMS uniform, periodic scaffold to determine their relative advantages. Cross-sections of the TPMS solid gyroid, Voronoi stochastic, and dense structures were printed by SLM to evaluate the pore interconnectivity and cell penetration further, as seen in Figure 4.7(A-C). Confocal laser microscopy assessed the cell distribution profile across the pores. Figure 4.7 (A) and (B) shows the cell growth across the cross-sections of each porous design and within the pore channels. In Figure 4.7(B), the TPMS solid gyroid showed increased cell activity for both the outer surface and pore channels compared to Figure 4.7(A), the Voronoi stochastic structure. The Z-profile of the surface of each construct and representative cross sections from the CAD design are shown in Figure 4.7(D) and (E). The TPMS solid gyroid and Voronoi stochastic design illustrate pores capable of facilitating cell growth, as shown by the signal profile along the Z-axis of cell-scaffold constructs. Notably, a greater number of pores are cellularized in the TPMS gyroid compared to Voronoi stochastic. Additionally, the cell trajectory profile comparison within a single pore is shown in Figure 4.8. The slope of the Voronoi stochastic is significantly steeper than the TPMS, which may negatively influence cell migration, integration, and occlude vascular ingrowth critical to subsequent bone formation.

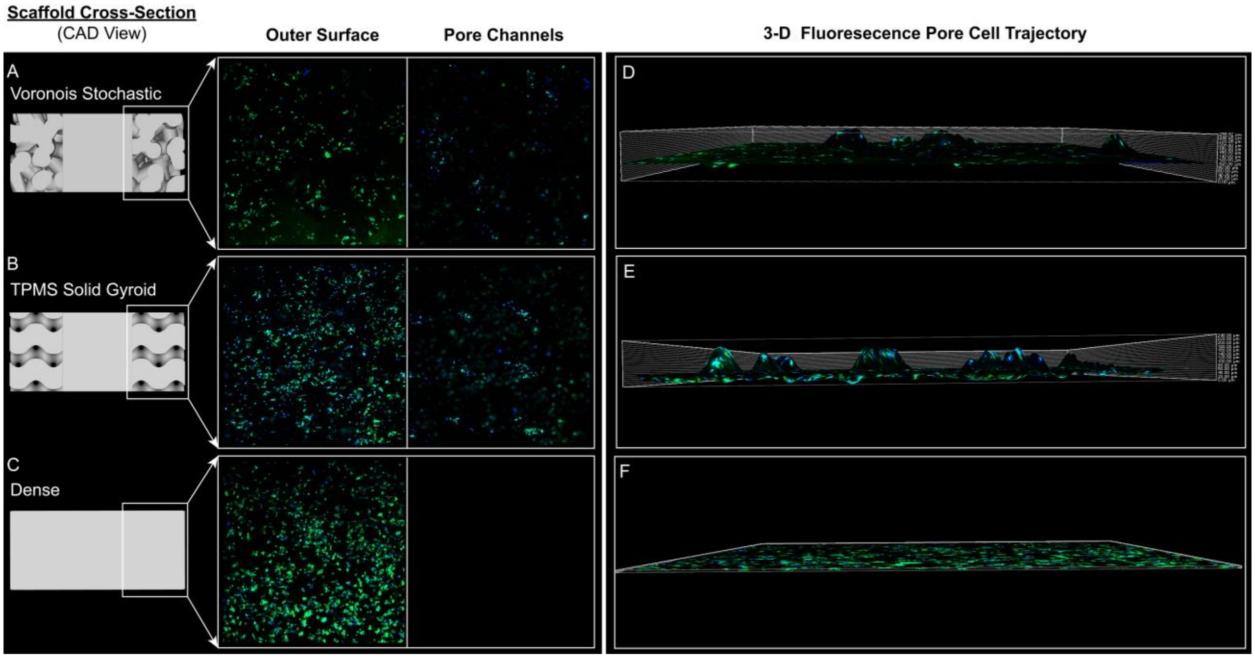

Figure 4.7: Confocal microscopy of the cell colonization on the SLM printed cross-sections on the outer surface and within the pore channels. The cytoskeleton is stained in green (Aleca Fluor Phalloidin 488) and the nucleus is stained in blue (DAPI). (A) Voronoi Stochastic, (B) TPMS solid gyroid, and (C) dense constructs, (D) 3-D fluorescence cell trajectory within a single pore for Voronoi stochastic, (E) 3-D fluorescence cell trajectory within a single pore for TPMS solid gyroid, and (F) 3-D fluorescence cell trajectory for no porous structure (dense).

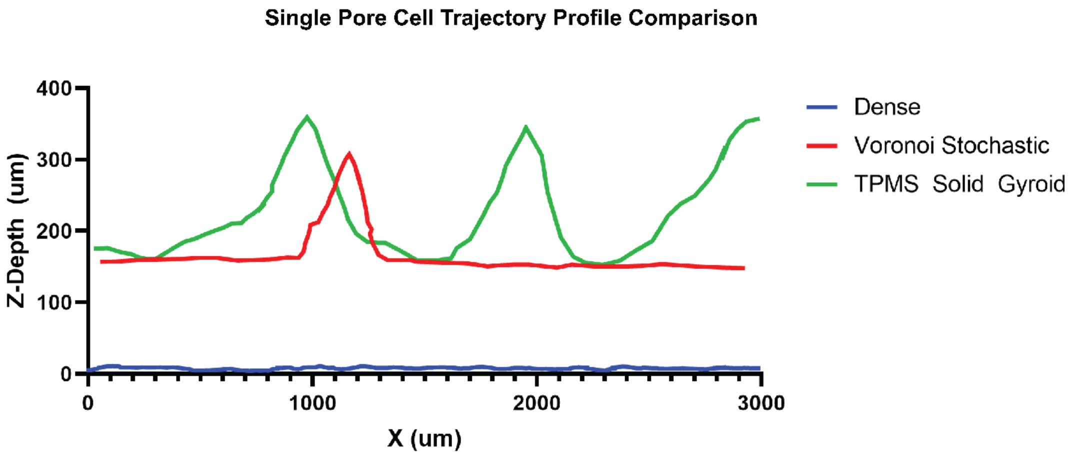

Figure 4.8: Comparison of the cell trajectory profile within a single pore of the cross-sectional Voronoi stochastic and TPMS solid gyroid scaffolds and on the cross-sectional surface of the dense structure.

4.3.2 Permeability and Streamline Interconnectivity

The characteristics of pores play a critical role in determining cell behavior, influencing processes such as cell adhesion, nutrient diffusion, cell proliferation, and bone growth. The solid-modeled pores from the micro-CT scan of the SLM-printed scaffolds in Figure 4.3 were used to comprehensively assess the theoretical behavior of cells using CFD simulation. This study examined the streamline patterns and permeability, coupled with in-vitro cell culturing, to systematically compare and eliminate the design with the least favorable permeability and trajectory behavior. Permeability values under static cell seeding and human body conditions were documented in Table 4.1, using DMEM and human blood as the fluid domain. The TPMS solid gyroid scaffold outperformed the TPMS sheet gyroid and Voronoi stochastic scaffold designs, exhibiting higher permeability than bone. The permeability of human and bovine trabecular bone is in the range of 0.22-1.45 x 10^{-8} m^2, and another study found the permeability of proximal tibia to be in the range of 0.467 – 14.80 x 10^{-9} m^2 [114], [115]. In this study, the

TPMS solid gyroid exhibited a permeability of 9.26×10^{-7} m^2 and 3.34×10^{-7} $m^{2,}$ as seen in Table 4.1.

Table 4.1: Permeability output for each porous construct in the cell culturing and human blood environment.

	Input		**Permeability** (m^2)		
Fluid	**Dynamic Viscosity** (kg/m·s)	**Inlet Velocity** (mm/s)	**Voronoi Stochastic**	**TPMS** Sheet Gyroid	**TPMS** Solid Gyroid
DMEM	9.30×10^{-4} [106]	0.01[108]	2.09×10^{-10}	1.3×10^{-10}	9.26×10^{-7}
Human Blood (Bone Marrow Microvessels)	4.00×10^{-3} [107]	0.7 [107]	1.10×10^{-10}	1.16×10^{-10}	3.34×10^{-7}

In addition to permeability, the velocity profiles and trajectory paths of the scaffolds influence the transport of mass and cell attachment [116], [117], [118]. Figure 4.9(A-F) shows the velocity and qualitative trajectory profiles from the computation fluid dynamic simulation of each scaffold in the environments of static cell seeding and the human body. Focusing on the TPMS structures in Figure 4.9(A), (B), (D), and (E), the minimal internal fluid rates indicate a more consistent velocity distribution, an attribute conducive to favorable bone growth [117]. The low-velocity profile facilitates robust cell adhesion to the titanium surface, promoting cell clustering and subsequent proliferation. The augmented proliferation positively indicates bone growth, particularly for the initial phases of osseointegration. However, the increasing velocity at the center of the pores shows the acceleration of cell migration to the scaffold core, a crucial factor for deeper bone growth. This phenomenon is consistent across all three porous structures shown in Figure 4.9. In Figure 4.9(B) and (E), the TPMS solid gyroid demonstrates the highest fluid trajectory with the most streamline paths traversing from the inlet to the center. Overall, the TPMS solid gyroid exhibits a lower internal fluid flow rate and the highest fluid trajectory, suggesting its potential for fostering an environment for enhanced cell growth. This observation aligns with the results of the in-vitro experiments for the TPMS solid gyroid configuration.

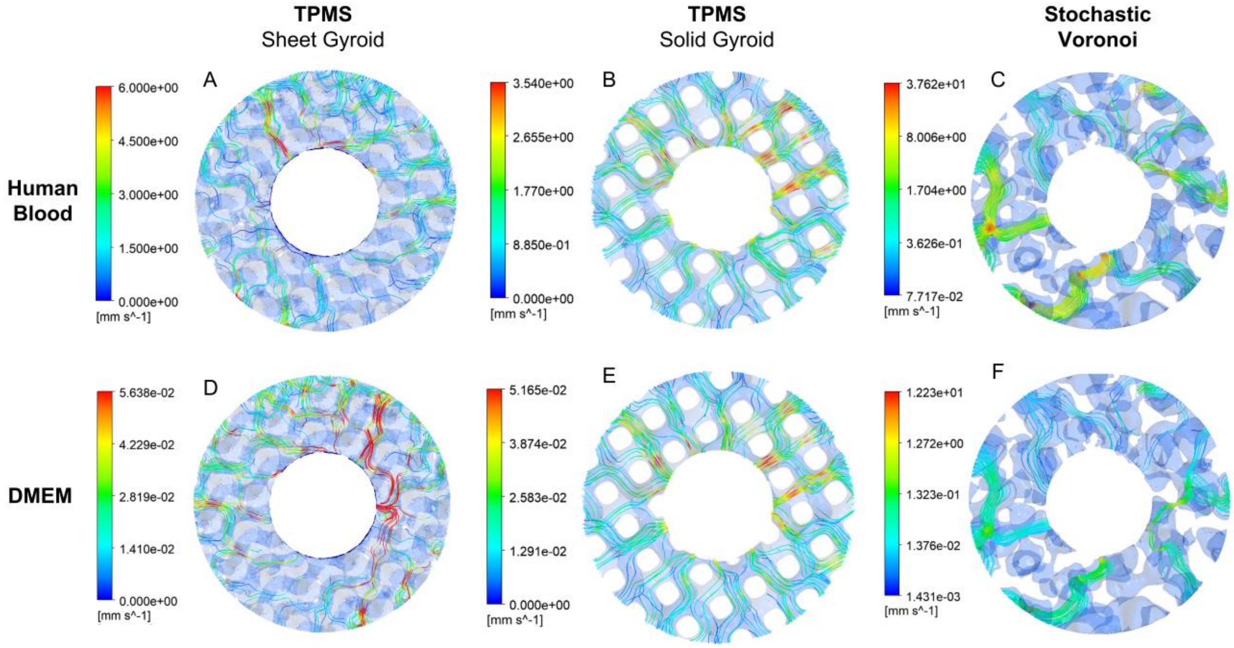

Figure 4.9: Velocity profile from CFD analysis of the TPMS sheet gyroid, TPMS solid gyroid, and Voronoi stochastic scaffolds: (A-C) scaffolds modeled in the environment of human blood; (D-F) scaffolds modeled in static cell seeding conditions using DMEM fluid. (B,E) The TPMS solid gyroid shows a high volume of flow trajectory from the inlet to the outlet.

4.4 Conclusions

This study investigates the optimal design of a Ti6Al4V SLM-manufactured porous architecture to improve the cell-implant contact area and supply interconnected channels for bone ingrowth. Understanding the relationship between pore size, permeability, velocity, trajectory, and cell infiltration within the porous channels is crucial for developing effective scaffolds that promote bone growth. The TPMS solid gyroid, TPMS sheet gyroid, and Voronoi stochastic scaffolds had a target design of 200-250μm interconnected pores. The findings suggest that the TPMS solid gyroid scaffold exhibited enhanced cell proliferation. Qualitatively assessing the solid-modeled pores from the micro-CT scan, the TPMS solid gyroid exhibited high interconnectivity and the CFD permeability study agreed with permeability values of 9.26 x 10^{-7} m^2 and 3.34 x 10^{-7} m^2 in the environments of cell culturing and human blood, which was closest to bone. The TPMS solid gyroid had enhanced cell interaction results with RNA quantity four times higher than the fully dense construct, the Voronoi stochastic scaffold showed an increased RNA quantity. Based on these results the TPMS sheet gyroid was not considered to be further tested for fluorescent microscopy. The TPMS solid gyroid architecture had favorable cell growth with the highest z-depth reaching 300µm within a single channel of the pore. The manufacturability paired with the biological response to each scaffold concluded that the TPMS solid gyroid architecture at a microporous scale showed promising results for enhancing cell behavior and tissue regeneration in bone tissue engineering. The unmelted or partially melted spherical powders as a resultant of SLM need to further be studied on the effects of cell adhesion and its harmfulness. Further hydrofluoric acid etching needs to be conducted and compared with the as-built structures. It is not yet clear if the randomness of the stochastic structure will outperform the periodic and uniform TPMS structure in a living bone environment. It is necessary to conduct in-vivo experiments comparing the behavior of the TPMS solid gyroid and Voronoi stochastic structure in relation to bone ingrowth.

Chapter 5 Mechanical Properties Evaluations of the TPMS Solid Gyroid Scaffold for the Fabrication of a Functionally Graded Porous Structure

5.1 Introduction

Bone regeneration plays a critical role in ensuring the sustained success and functionality of dental implants in edentulous patients. The biological process responsible for this success is osseointegration, which entails the direct connection between bone and the metallic implant [1]. Although the titanium alloy Ti6Al4V extra low interstitial (ELI) Grade 23 is most widely used in orthopedics because of its high biocompatibility, resistance to corrosion, low density, low elastic modulus, and high strength, there remains a high stiffness mismatch between the metallic implant and bone leading to failure mechanisms during the bone remodeling stage [2], [3]. There is an insufficient load transfer from the dense, high-strength metallic implant to the bone, resulting in an uneven stress distribution and a remodeling of weaker bone [4], [5]. This phenomenon is known as the stress shielding effect that causes bone resorption and subsequent complications [5]. The titanium dental implant interfaces with trabecular and cortical bone, exhibiting elastic moduli of 3.5-125.6 MPa, and porosity of 50-90% and 12.7-22.8 GPa and porosity of 5-10%, respectively, in contrast to the high-strength Ti6Al4V implant at 114 GPa and 0% porosity [6]–[8].

Lattice structures have become increasingly popular for modeling porous architectures in orthopedic implants with their ability to be manipulated for desired mechanical properties to match that of its surrounding bone [9]. More specifically, the triply periodic minimal surfaces (TPMS) lattice configurations are uniform, periodic, and continuous in three independent perpendicular directions, resulting in high interconnectivity [10]. Various TPMS structures exist, but the design of interest is the solid gyroid structure because of its superior mechanical properties and permeability compared to other TPMS structures[11]. There also exists two variants of the TPMS gyroid structure, a sheet and solid structure. The geometry of the sheet gyroid structure has a higher stiffness when compared to the solid gyroid, but in our previous work it was shown that the TPMS solid gyroid had superior biological performance and higher manufacturability. A study was conducted comparing the mechanical properties of a sheet gyroid and solid gyroid under the same testing conditions, showed that the elastic modulus of the solid gyroid decreased by 1.09 GPa from the sheet gyroid [12]. However, for dental implants it is desirable to have a lower elastic modulus to reduce the stress shielding effect without compromising the mechanical integrity.

The integration of pores increases the stress in the surrounding bone, leading to a reconstruction of higher-density bone reducing the stress shielding effect and potential for enhanced biological performance [13]. Although porous materials would increase surface area for enhanced cell attachment and reduce the elastic modulus to eliminate the stress shielding effect, it would in turn compromise their mechanical integrity to withstand physiological loading [14], [15]. To address the trade-off, a functionally graded porous architecture with a variation in pore size and porosity leading to a dense core is proposed and would mimic the physical attributes of bone, maintain sufficient mechanical strength, and enhance biological performance. The smaller pores provide an environment for better cell attachment because of the higher available surface area, while the larger pores would enable cell infiltration for bone regeneration. Specific pore size ranges also play an important role in the promotion of bone growth and transport of cells. Pore sizes ranging from 200-425µm are optimal for cell growth, while pore sizes between 60-125µm inhibit and do not significantly affect bone growth[16].

For the safety of the patients, it is important to understand the relationship between the porous architecture, mechanical properties, and mechanical integrity of the proposed implant design. The compressive properties are of main interest because dental implants are under compressive occlusal forces. Inducing the TPMS solid gyroid porous architecture alters the mechanical structure and behavior of Ti6Al4V, thus it is important to characterize the failure behavior of the lattice along with the mechanical properties. Notably, compression testing the functionally graded porous structure with the solid core would provide misleading results because the solid core will withstand the loading at a higher rate, thus the characterization of the pore architecture and porosity at each point along the gradient is not possible. Xiong et al showed that adding the dense core increased the compressive mechanical strength of an additively manufactured Ti6Al4V lattice structure compared to a fully porous structure [17]. Previous studies first characterized fully porous structures before fully integrating it into the implant. Seyad et al, compression-tested TPMS gyroid structures with porosities ranging from 54-72% and 600- 1200µm pore sizes successfully reducing the compressive modulus ranging between 5.69-8.46 [18]. Yang et al, fabricated and compression-tested Ti6Al4V gyroid unit cells using laser powder bed fusion with a volume fraction of 25% and an elastic modulus of 2622.42 ± 110.33 MPa [19]. These studies obtained global strain measurements, and at a microporous level, it is important to analyze the strain behavior locally. The manipulated titanium alloy structures with the inductions of pores result in unknown structural behavior under loading, making a single measurement strain gauge insufficient for comprehensive characterization [20].

Digital image correlation (DIC) has been widely accepted and used in previous studies to output full-field strain measurements while observing the failure mechanism of porous structures [21]–[23]. DIC is a contactless, optical measurement that tracks the deformation from images taken from a high-speed camera to output strain [21]. The deformation is tracked from a gradient speckle pattern applied to the surface of the sample, using spray paint [21], [24]. It provides high-accuracy deformation outputs from the sequence of digital images recorded with respect to the pores, and strain can be analyzed locally at specific areas of interest [21]. The use of DIC as a strain measurement during compression testing to report the compressive elastic modulus of additively manufactured SLM Ti-6Al4V in lattice structures is limited. The limitations that are considered are the small dimensions of the samples, roughness of the surface and, consequently, difficulty in focus and calibration of the DIC lenses for pore sizes at the micro scale.

This work aims to design, fabricate, and characterize a TPMS solid gyroid functionally graded implant. Our design approach consists of an interconnected structure with larger pores and increased porosity on the outer surface to promote a larger volume of bone growth while decreasing the pore size and porosity of the dense core will help maintain the mechanical integrity to withstand physiological loading [25]. The bottom-up, layer-by-layer approach of additive manufacturing is the optimal fabrication method for these lattice structures. Specifically, selective laser melting (SLM) can produce parts with mechanical properties and density comparable to the bulk material and achieve complex lattice design features [26].To understand the mechanical behavior and properties of each induced porosity within the gradient, we separately designed and manufactured five combinations of pore size and porosity that create the target gradient. First, an analytical model was used to gain insight into the relationship between porosity and elastic modulus in a functionally graded structure. Based on these results, we developed the five different combinations of the porosity and pore size with the TPMS solid gyroid architecture, these included 16.75% and 130μm, 21.65% and 185μm, 31.28% and 280μm, 40.64% and 360μm, and 48.42% and 420μm. Consequently, the optimal porosity and pore size combination for mechanical integrity and compressive properties can be chosen to produce the optimal functionally graded porous dental implant structure.

Therefore, this study aims to experimentally characterize each individual pore size and porosity combination along the intended gradient to identify the optimal combinations for a functionally graded TPMS solid gyroid porous structure. The characterization includes the elastic modulus, crack behavior, and failure mode under compression with the implementation of 2D DIC paired with optical microscopy for the analysis of microscale deformation. It is vital to draw a relationship between the porous architecture and mechanical integrity. The methods for modeling the TPMS solid gyroid structure, manufacturing, and experimental testing are presented in this paper.

5.2 Methodology for the Mechanical Performance Evaluation of a Functionally Graded TPMS Gyroid Scaffold

The analytical numerical model is introduced as a starting point for the designing and fabrication of five different porous structures optimal to be included in the functionally graded porous design leading to a dense core. Based on this, a range of the porosity and pore size combinations of the TPMS solid gyroid architecture are designed and fabricated using SLM to evaluate the optimal design for a functionally graded porous structure and characterized using micro-CT. Each combination of pore size and porosity are experimentally tested in compression using 2D digital image correlation to accurately evaluate the strain during compression of the microporous structures. The fracture of each of these designs is then analyzed for the mode of failure and behavior under compression.

5.2.1 TPMS Solid Gyroid Design of Experiments of Pore Size and Porosity Combination for a Functionally Graded Porous Scaffold

The target is to design a functionally graded TPMS solid gyroid porous scaffold with a dense core. To evaluate the optimal combination of porosity and pore size, ascending from the middle solid core, five fully porous structures were designed, varying the pore size and strut length, which manipulated the porosities. The porosities were chosen based on the analytical model used to output the theoretical elastic modulus of a functionally graded structure. The implant was sectioned into five different zones, excluding the solid core.

The mathematical model in equation 4.1 was used to analyze the relationship between the functionally graded porous structure and the elastic modulus [27]. A and B denote the porous and solid material properties, where the porosity is increasing outward, and a solid core is in the center, as seen in Figure 5.1, where the center area is 100% solid titanium and 0% porous with an increasing porosity moving outward from the center to each side equally.

$$P_{(FGM)}(z) = (P_{(A)} + P_{(B)})(\frac{1}{2} + \frac{z}{h})^{n} + P_{(B)} - \frac{\alpha}{2}(P_{(A)} + P_{(B)})(1 - \frac{2|z|}{h}) \qquad (5.1)$$

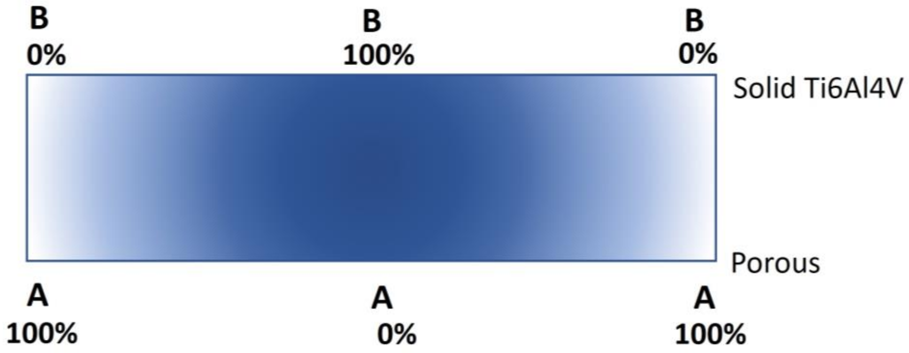

Figure 5.1: Functionally graded porous material varied along the thickness direction with the center as the solid core.

In Equation 5.1, P denotes the material property, in this case, the elastic modulus, z is the location across the thickness coordinate, h is the thickness of the sample, α is the defined porosity volume fraction, and n is the power-law index. The range of porosities studied was from 10-50%, this limitation was set based on the practicality of being implemented into a dental implant. The power law exponent used was 11. When the power law exponent tends to zero, it assumes a homogeneous isotropic sample built from two different compositions. When the power law exponent tends to infinity, it assumes the plate is tending towards a single phase [27] . Since the core is fully dense, it is assumed that a higher power law exponent be used. On the other hand, in previous research when the center of the sample is composed of two different phases a lower power-law exponent is used based on the behavior of the elastic modulus of the samples studied[1]. This is attributed to the fact that, the softer the material the higher the power law index used. In this study, we assume that the material on the top surface is stiffer than the material on the bottom surface, which means the plate becomes softer with a larger power-law index [28] . Compression test data will then be used to create a correlation between the experimental mechanical properties and predicted to validate this assumption.

The results from the analytical model in Equation 5.1 are shown in Table 5.1. When the porosity is at 0%, the elastic modulus is 114 GPa.

Table 5.1: Analytical elastic modulus from the mathematical model for each zone with a porosity ranging from fully dense to 50% volume fraction.

Zone	**Porosity** (%)	**Analytical Elastic Modulus** (GPa)
--	0	113.99
1	10	103.94
2	20	93.53
3	30	81.66
4	40	65.10
5	50	35.25

Based on the analytical model, five different pore sizes and target porosities of 10%, 20%, 30%, 40%, and 50% were designed, manufactured, and compression tested. Figure 5.2 shows an example of the CAD model with the designed gradient of pores separated into five zones with a pore size and porosity combination based on the analytical model applied to a section along the z axis. The smaller pores begin at the solid core and increase in porosity and pore size to the outer surface for the promotion of bone growth. In this sample the length of the gradient, h is identified as 4.5mm, excluding the solid 0.5mm solid core, and z is the point at the start of each zone along the coordinate.

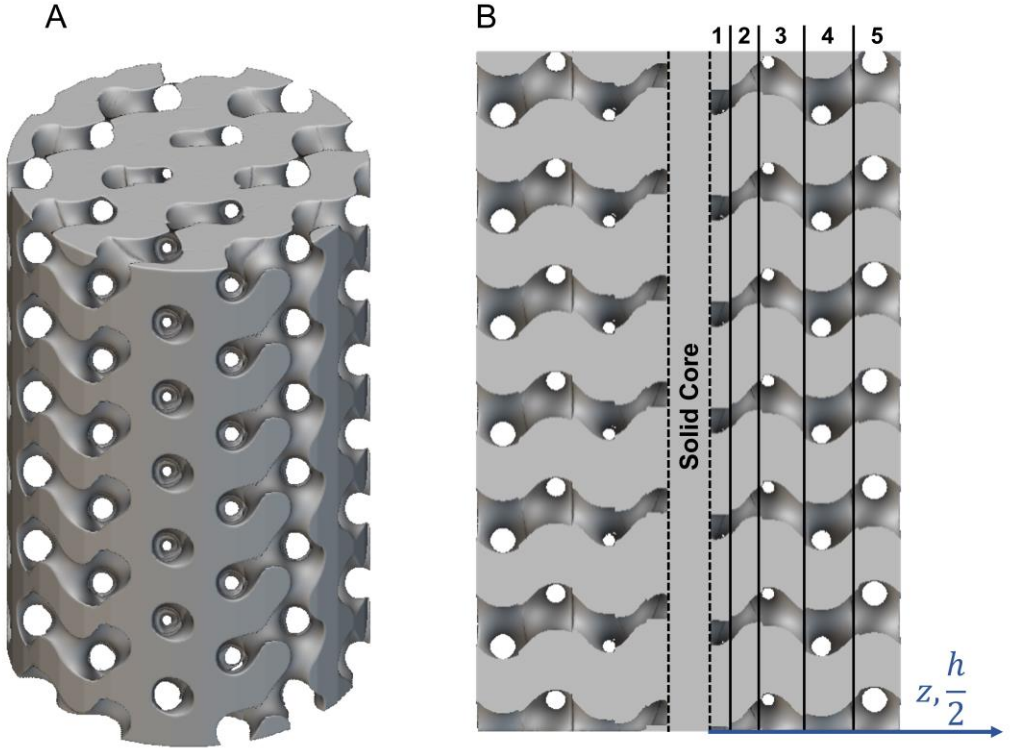

Figure 5.2: Functionally Graded TPMS Solid Gyroid Porous Structure. (A) Isometric view; (B) Cross-sectional CAD model with a solid core, ascending pore size, and porosity to the outer surface divided into five zones. z represents the point along the coordinate and the height divided by 2.

The pore size was chosen based on the optimal size for cell growth ranging from 130-420µm [16]. We designed, manufactured, and tested five fully porous designs from each zone to characterize each porous zone. Table 5.2 shows the combination of parameters to achieve the porosities based on the analytical model and the pore sizes based on optimal cell growth. Two input parameters exist to alter the pore size and porosity, these are the unit cell size and the wall thickness constant. The unit cell was kept constant for consistency of the periodicity of the applied porous architecture. To maintain a constant periodicity in each structure, a 1.25mm x 1.25mm x 1.25mm constant cell size was set for each construct, while the thickness constant was manipulated to alter the porosity and pore size. The unit cell size of 1.25mm in the x-y-z direction was chosen to achieve porosities close to the analytical model while maintaining a pore size conducive to cell adhesion to achieve bone ingrowth. The goal was to test at a low-porosity pore-size combination that still achieved interconnectivity and maintained physiological loading and a high-porosity pore-size combination that promoted the ingrowth of bone and was still deemed optimal to withstand physiological loading. The pore size and porosity are decreased when the wall thickness increases.

Table 5.2: Combination of the designed pore size, wall thickness, and porosity with a constant cell size.

Zone	**Cell Size (mm)**	**Wall Thickness (mm)**	**Designed Pore Size (µm)**	**Designed Porosity (%)**
1	1.25	0.21	130	16.74
2		0.18	185	21.65
3		0.12	280	31.28
4		0.06	360	40.64
5		0.01	420	48.42

Figure 5.3(A-E) shows the isometric and side view of the individual zones as fully porous structures 16.74%, 21.65%, 31.28%, 40.64%, and 48.42%. The dimensions of the porous structures were chosen based on the American Society of Testing Materials ASTM E9 standard for the geometric size to reduce buckling during compression testing while maintaining dimensions similar to a dental implant [29]. These dimensions are a 5mm diameter and 7.5mm length to achieve a diameter-to-height ratio between 1 and 2.

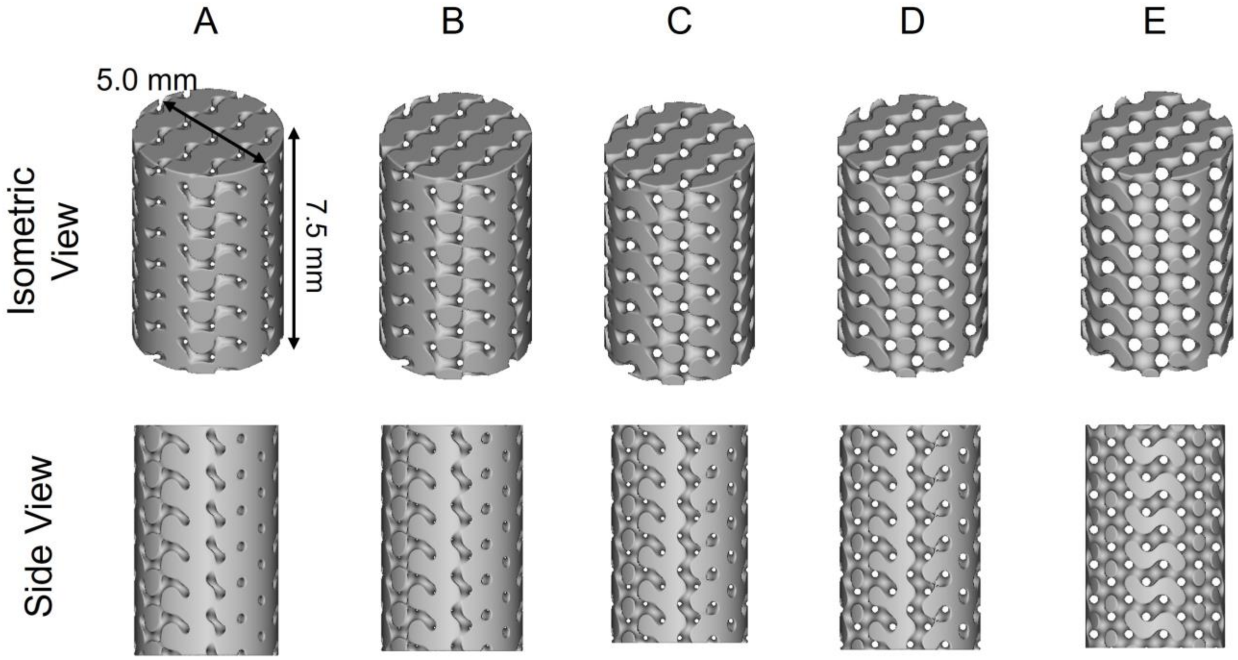

Figure 5.3: CAD Models of the 5mm diam x 7.5mm length TPMS solid gyroid samples with a constant 1.25mm cell size and varying pore sizes, porosity, and wall thickness. (A) 16.74%, 130µm, 0.21mm; (B) 21.65%, 185µm, 0.18mm; (C) 31.28%, 280µm, 0.12mm; (D) 40.64%, 360µm, 0.06mm; (E) 48.42%, 420µm, 0.01mm.

The additive manufacturing technique, selective laser melting (SLM) using the TruPrint 1000 machine and Ti6Al4V Grade 23 ELI powder was used to fabricate the intricate microporous structures shown in Figure 5.4. The optimal machine parameters to produce high resolution and near dense parts included a laser power of 155W, a laser diameter of 30µm, a layer thickness of 20µm, a hatch space of 60 µm, and a scan speed of 1200mm/s. The Ti6Al4V titanium alloy powder had a particle distribution of 15-45 µm. Figure 5.4(A-E) shows the additively manufactured samples for compression testing.

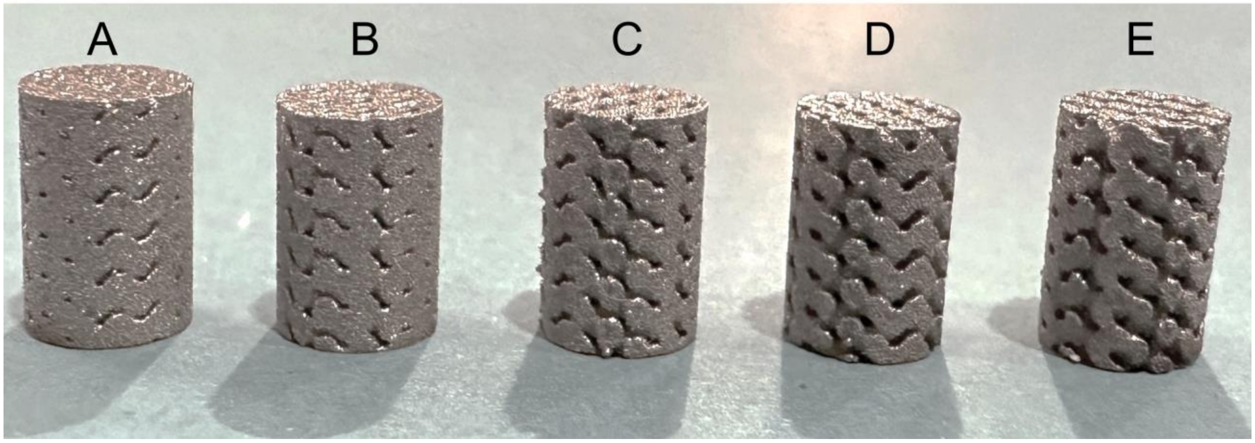

Figure 5.4: The selective laser melted samples for each designed porosity, pore size, and wall thickness. (A) 16.74%, 130µm, 0.21mm; (B) 21.65%, 185µm, 0.18mm; (C) 31.28%, 280µm, 0.12mm; (D) 40.64%, 360µm, 0.06mm; (E) 48.42%, 420µm, 0.01mm.

The manufactured porous structures were then evaluated using micro-CT for their manufactured pore size and porosity. The results from the compression test helped choose the optimal porosities in a functionally graded porous dental implant. The manufactured pore size and porosity were inputted into a micro-CT scan using the Zeiss XRadia Versa 520 3D X–ray Microscope at the Michigan Center for Materials Characterization at the University of Michigan. The outputs from the micro-CT scan were inputted into DragonFly ORS to characterize the pore size, porosity, and pore size distribution.

5.2.2 Experimental Compression Setup using 2D Digital Image Correlation

The real-time dental implant application is in compression, so quasi-static compression tests were performed on the MTS 810 Material test System. The test conditions were carried out based on the International Organization for Standardization ISO 13314:2011 [30]. The constructs were tested under uniaxial compression at a strain rate of 10^{-3}/s and correlated to the crosshead speed of 1mm/min. A sample size of three was used for each porous design. Each test was stopped when the sample failed. The microporous structure and 5mm diameter x 7.5mm length posed a challenge for accurately measuring the strain. Digital image correlation (DIC) was the optimal choice for strain measurement to accurately characterize the failure and strain. Cameras from Correlated Solutions and the Vic-2D Digital Image Correlation software were used to record and post-process the images. DIC is used to measure the full-field displacement, and the irregularities in the structure. Figure 5.5(A-D) shows the compression testing setup of the specimen in the MTS compression machine with a load cell of 100kN and the DIC system. The DIC system in Figure 5.5(A) and (B) consists of a two-camera, two-light fixture setup. Figure 5.5(C) shows a side view of the test specimen between the cylindrical platens. The platens were covered in black cloth to reduce glare in the cameras and increase the resolution of the output images of the sample. Digital image correlation relies on a speckle pattern imposed on the sample to measure the deformation. The DIC algorithm tracks the speckle pattern during the compression test, and the difference in displacement of the speckles is used to output the strain measurement. The sample was first sprayed with a matte white paint to reduce glare from the camera and an airbrush was used to induce the black speckle pattern. Figure 5.5(D) shows an enlarged image of the sample with the speckle pattern for DIC.

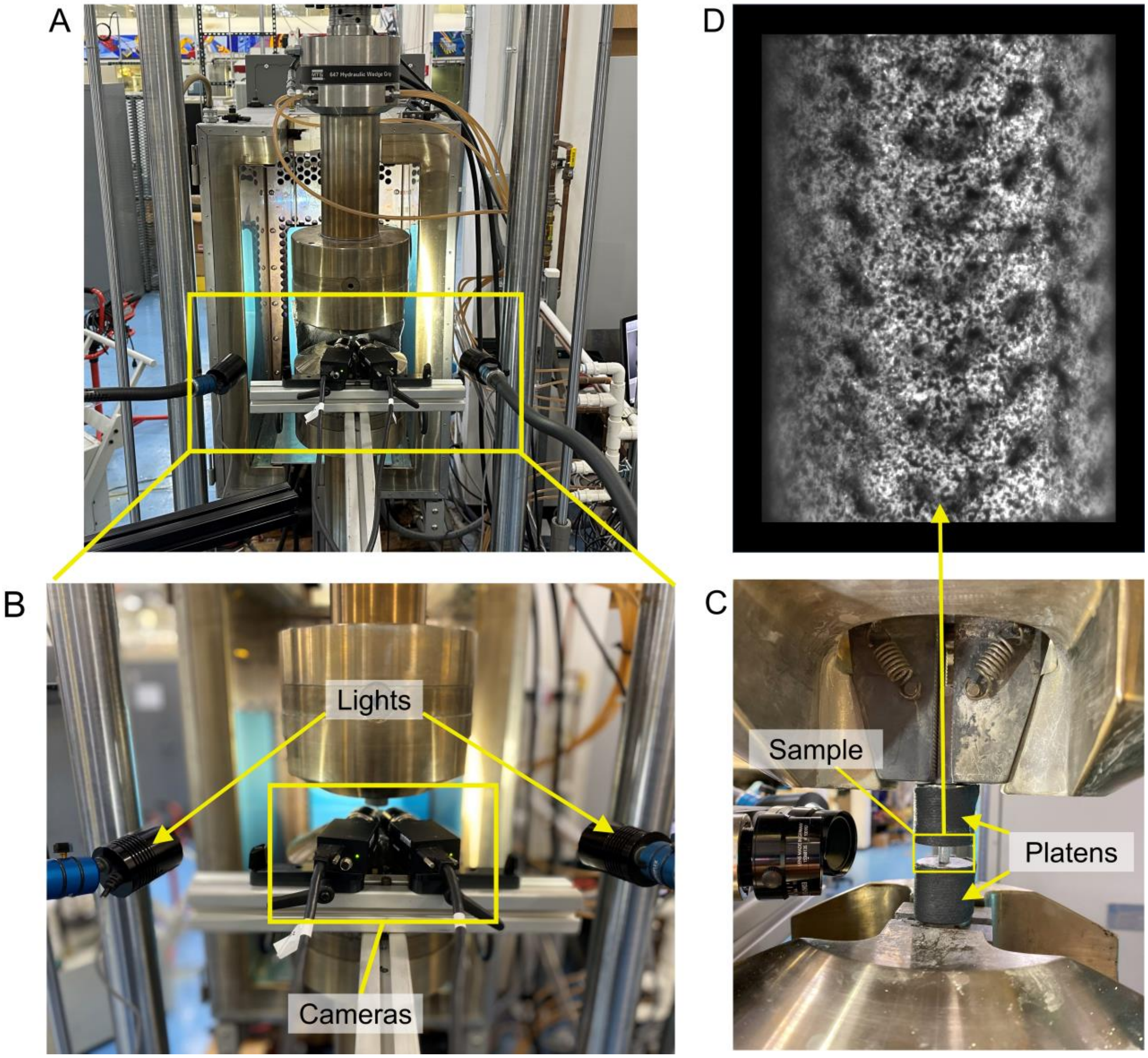

Figure 5.5: (A) The complete digital image correlation (DIC) configuration. (B) The enlarged setup of the two cameras and two light fixtures. (C) Side view of the 5mm diameter x 7.5mm length test specimen between the two compression platens. (D) The enlarged output image of the test specimen with the speckle pattern before loading.

The sampling frequency was set at 5Hz for the DIC and MTS systems data output of the force and displacement measurements. Figure 5.6 shows the data processing method where a region of interest, Figure 5.6 (B), is selected from the output image obtained from DIC and applied to the entirety of the output images from the entire duration of the compression test, and the strain is calculated. In the DIC software, an extensometer is placed along the region of interest to output a strain value for every displacement image.

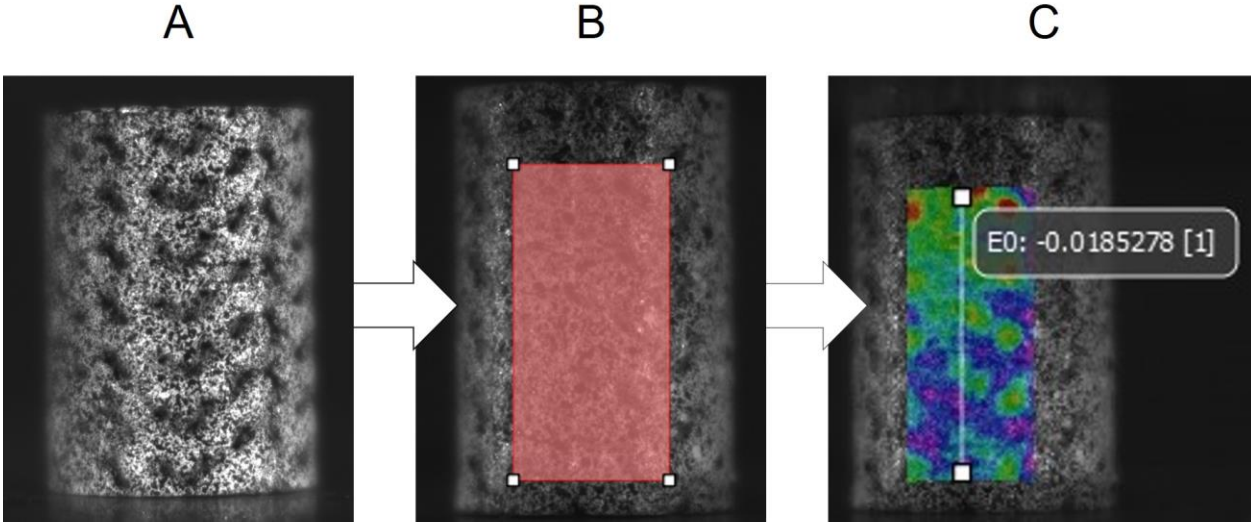

Figure 5.6: Data processing method for DIC: (A) Images at each form of displacement during compression. (B) Region of interest to analyze deformation. (C) Strain calculated in the region of interest at each point of displacement.

The force values from the MTS system were correlated to the strain outputs from the DIC system to plot the stress-strain curves and calculate the elastic modulus for each sample from the slope of the stress-strain curve in the elastic region.

5.2.3 Characterization of Failure from Experimental Testing

The fracture of the five different porous samples was analyzed to gain insight into the failure behavior of the TPMS architecture during testing. The Nikon Eclipse Ci Biological Microscope with a DS-R12 camera and a capture resolution of 16.25 megapixels was used in the Van Vlack Lab at the University of Michigan. An image was taken at four different sections along the fracture line for each sample at a 10x magnification using the NIS-Elements software. At each section, the angle of the line was measured to analyze the failure mode.

The surfaces of the internal fractured samples were observed using the TESCAN RISE scanning electron microscopy (SEM) at the Michigan Center for Materials Characterization at the University of Michigan. Before the analysis, the samples were coated in gold using a sputter coater.

5.3 Results and Discussion

5.3.1 Manufacturability of the TPMS solid gyroid scaffolds with varying pore size and porosities

The SLM-manufactured pore sizes and porosity are listed in Table 5.3 with the percent error in relation to the designed porosity. It can be noted that with increasing the pore size, the difference between the designed and measured porosity decreases, and this trend is represented by the results from micro-CT. With increasing pore size, it is more easily attainable through SLM because the complexity is reduced.

Table 5.3: Designed and SLM manufactured pore size and porosity at each zone.

	Designed		**SLM Manufactured**	
Zone	**Pore Size** (µm)	**Porosity** (%)	**Average Pore Size** (µm)	**Porosity** (%)
1	130	16.74	69.47 ± 44.76	5.04
2	185	21.65	111.10 ± 59.52	11.64
3	280	31.28	168.20 ± 75.16	17.78
4	360	40.68	245.72 ± 91.48	25.91
5	420	48.42	300.45 ± 108.65	34.00

The manufactured pore size deviated from the target design, but a gradient was attained from large to small pores with a standard deviation. The distribution of pores for each SLM-manufactured porous sample is shown in Figure 5.7 (A-E) from the processed image data from the micro-CT scans. In Figure 5.7(A), the pore size distribution of the designed 130µm SLM manufactured average pore size calculated was 69.47 ±44.76µm but is centered around 93.01 µm. Figure 5.7 (B), the pore size distribution of the designed 185µm SLM manufactured average pore size calculated was 111.10 ±59.52µm and is centered around 174.39 µm. Figure 5.7 (C), the pore size distribution of the designed 280 µm SLM manufactured average pore size calculated was 168.20 ±75.16µm and is centered around 232.52µm. Figure 5.7 (D), the pore size distribution of the designed 360µm SLM manufactured average pore size calculated was 245.72

±91.48μm and is centered around 313.9μm. Figure 5.7 (E), the pore size distribution of the designed 420μm SLM manufactured average pore size calculated was 300.45 ±108.65μm and is centered around 383.66μm.

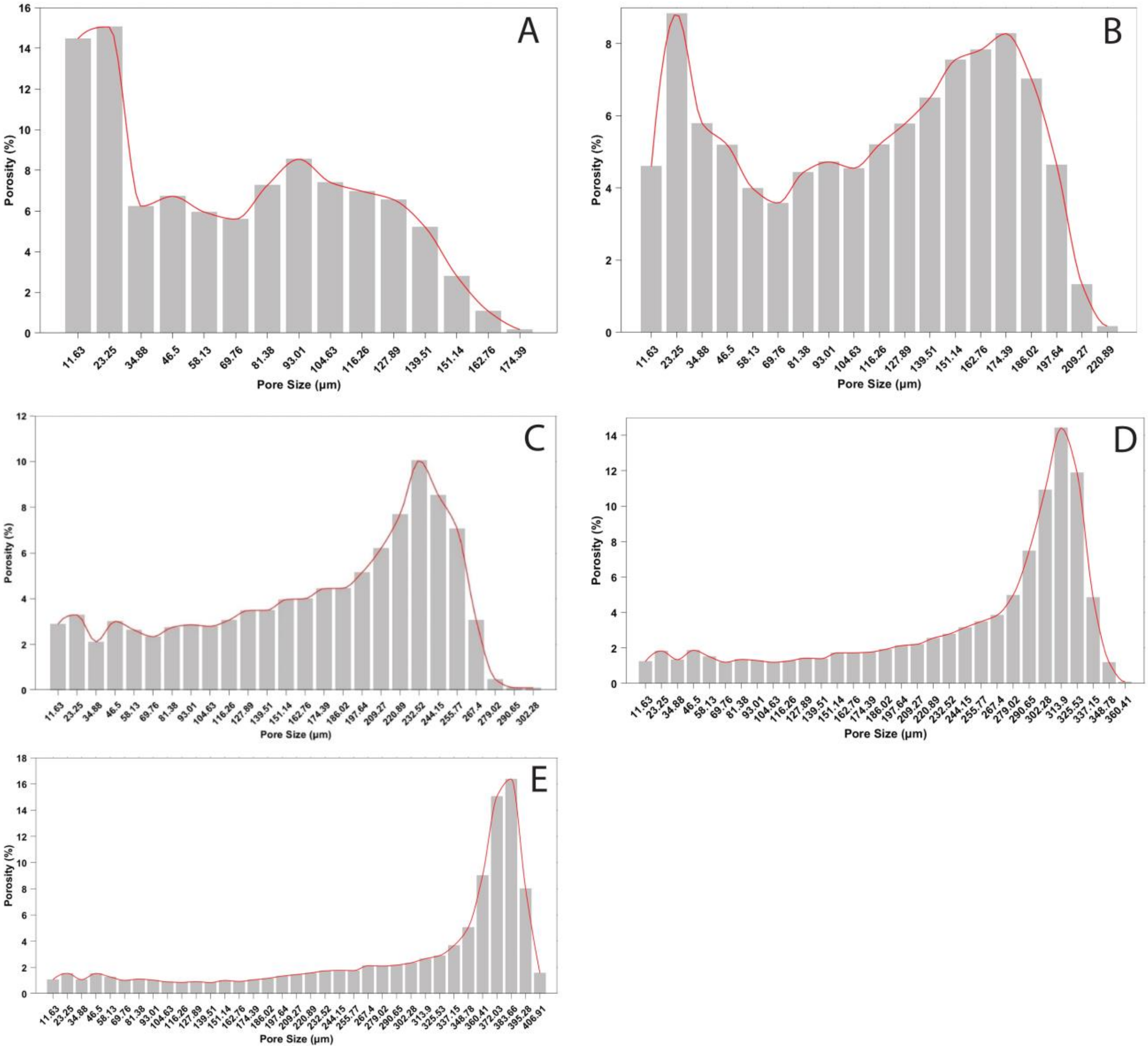

Figure 5.7: (A-E) The pore size distribution of each manufactured construct. (A) 5.04%, (B) 11.64%, (C) 17.78%, (D) 25.91%, (E) 34.00%.

Designed pore sizes of 130μm and 180μm, Figure 5.7(A,B) showed the highest number of pores distributed from 11-100μm. The spot size of the TruPrint machine is 30 μm, thus the resolution is centered around this. The pores less than around 30 μm could be a result of keyhole, lack of fusion, or entrapped gas pores. The large number of pores that are less than 30μm can also be attributed to the fact that in the pores that are not interconnected, closed pores, some powder particles trapped pores are affecting the calculation of pore size. Referencing the process map by Weber et el. for the TruPrint 1000 for Ti6Al4V, the process parameters are within the fully dense melting phase. The process parameters were also obtained from the TRUMPF company for the optimal parameters for Ti6Al4V with a laser spot size of 30μm. It has been noted that gas pores tend to be less than 10μm and are considered negligible [31]. The overall effect of pores induced from printing due to either process parameters or limitations in the machine for producing complex geometry is unclear. The overall effects of the pore sizes induced in this case are not clear but hypothesize and attribute these to two different effects. First, it is a entrapped gas pore and due to the size we ignore it in relation to further testing. Second, this could be attributed to the partially melted powder particles that are partially fused to the walls. This is an effect that can not be completely avoided even by adjusting the process parameters. These are formed during laser scanning when the adjacent powders are partially melted onto the side and overhang surfaces. The trend of pore sizes was still attained, although the designed pore trend was intended to reside within 130-420μm, the manufactured pore sizes resided within approximately 93-386μm. This was acceptable for our purpose in terms of creating a functionally graded porous structure with interconnected pores to promote bone ingrowth while reducing the elastic modulus to match that of bone. All while maintaining mechanical integrity.

5.3.2 Mechanical Properties from 2D Digital Image Correlation

To effectively reduce the stress shielding effect, the elastic modulus needs to be decreased to create a more even stress distribution from the loading. The Ti6Al4V, with the TPMS solid gyroid architecture, has altered structural properties with no standard of direct comparison. It was important to fully characterize these structures and their behavior. Cellular metallic foams typically exhibit a compressive mechanical behavior in three phases. It starts with a linear elastic region upon loading until its maximum loading point, once this elastic limit is reached there is a plateau constant where sometimes there are multiple peaks as a result of collapse and the plastic deformation of the lattice struts and progressive cell crushing. In the third phase there is densification, where the collapsed cell walls come into contact and there is a significant increase in stress because the load is directly transmitted to the next layer of cells [140]. In our results, not all structures followed this behavior. Because we are interested in biomedical implants and stress shielding, the main focus is to reduce the elastic modulus to mitigate stress shielding; thus, the elastic behavior and properties are of interest with a high yield stress for effect on improving fatigue resistance. With this, there are also three modes of possible failures that lattice structures can exhibit, layer-by-layer failure, which corresponds to low energy absorption, each layer collapsing into the on below it. Second is a brittle fracture, and the propagation of the cracks through an internal pores, the third is in diagonal shear. In some cases there are a combination of layer-by-layer and shear. Figure 5.8 (A-E) shows the stress-strain curves from the compression tests for each of the five specimens tested: 5.04%, 11.64%, 17.78%, 25.91%, and 34.00 %. Each curve is labeled by the first digit of the corresponding porosity and the number proceeding is the sample number. The behavior of the TPMS solid gyroid specimens did not directly follow the behavior of the conventional cellular structures. All fractures were measured under a microscope and further studied using SEM.

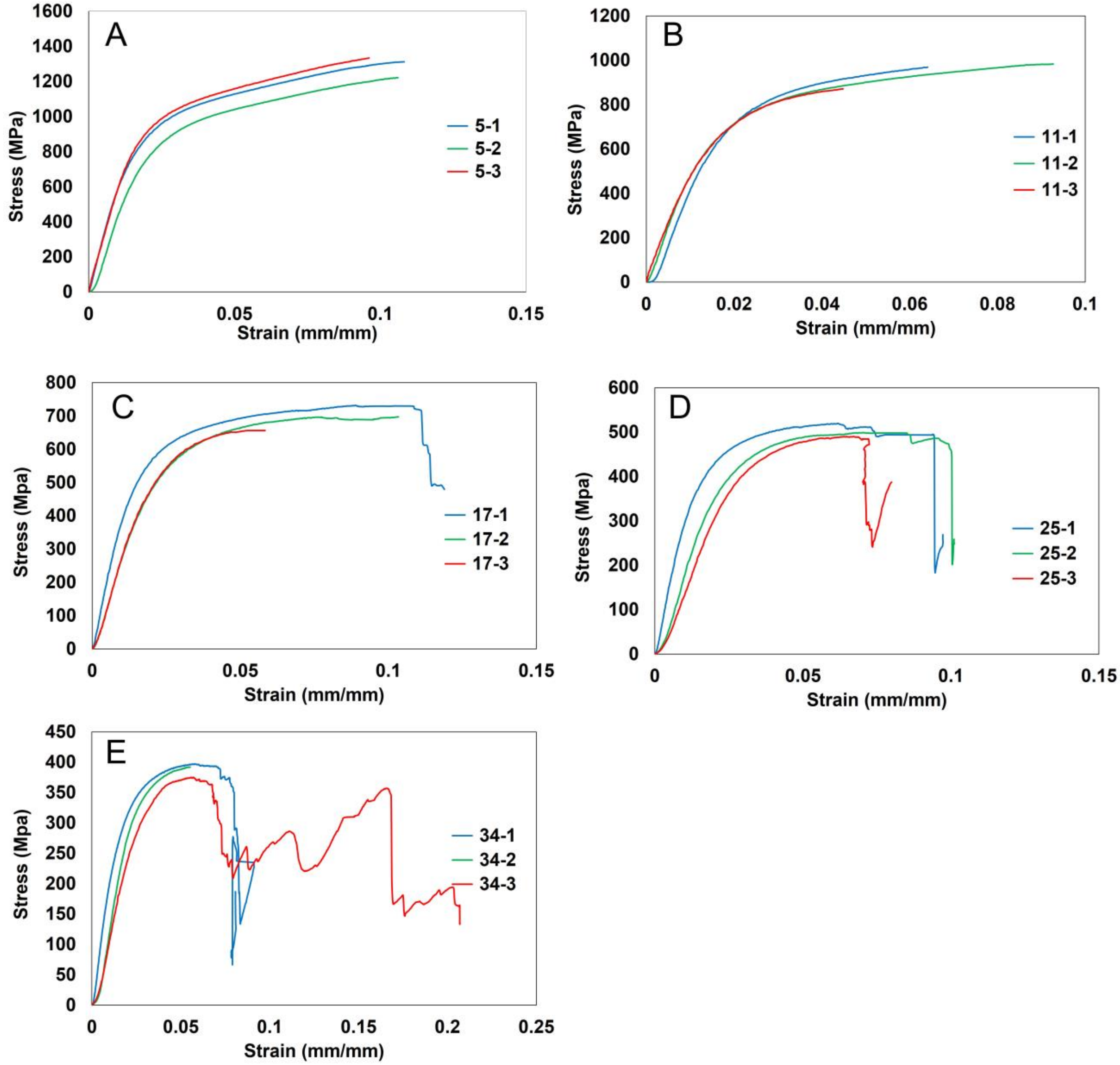

Figure 5.8: Compressive stress-strain curves for each set of TPMS solid gyroid scaffolds tested with varying pore size and porosity. (A) 5.04%, (B) 11.64%, (C) 17.78%, (D) 25.91%, and (E) 34.00%.

In Figure 5.8(A) and (B) the gyroids with a porosity and pore size of 5.04% and 130μm and 11.64% and 260μm behaved as a bulk material with low ductility, with displacement and strain increasing with increasing stress. In both cases it was observed to have failed in shear.
In Figure 5.8(D), the 25.91% porosity and 380μm structure had a sharp stress decline. We hypothesize this is a brittle failure, but further SEM was conducted to analyze the fracture [32].

The maximum force withstood decreased with increasing porosity; thus, the strength was reduced. During compression testing there was an observations made for the higher porosity and pore size samples. In the 25.91% and 34.00% porous samples, an internal collapsing was observed from the DIC output camera, then there was an increase in the load applied until failure. This could be due to the combination of the layer-by-layer and shear failure modes. This behavior is also attributed to a behavior that mitigates the risk of catastrophic failure, which is favorable in biomedical applications.

The average elastic modulus of the three samples compression tested for each porosity and pore size combination is plotted and compared to the analytical model shown in Table 5.4. The structural elastic modulus was obtained from the linear elastic region of the stress-strain curves, ranging from 59.48GPa to 19.19GPa for porosities between 5.04% and 34.00%. The manufactured samples had a lower elastic modulus than the analytical model. The reason for this is that the analytical model only considers the porosity of the material, not the porous architecture, for example, the geometry of the beams between the pores that play a role in maintaining mechanical strength. In particular, the TPMS solid gyroids architecture has high mechanical strength. Not only this, but they do not exhibit nodal points, the curvature between the pores eliminated the stress concentration [33]. The reason for considering the analytical model was to gain insight into the potential material properties of a functionally graded porous structure with a solid core. This was used as a starting point for the design, manufacturing, and experimental process.

Table 5.4: The theoretical porosity and elastic modulus compared to the manufactured sample porosity and experimental elastic modulus from the compression tests.

Theoretical		**Experimental**	
Porosity (%)	**Elastic Modulus (GPa)**	**Porosity (%)**	**Elastic Modulus (GPa)**
10.00	103.94	5.04	59.48
20.00	93.53	11.64	51.53
30.00	81.66	17.78	35.33
40.00	65.10	25.91	25.02
50.00	35.25	34.00	19.19

In Figure 5.9 for each porous structure at different porosities, the trend was clear: with increasing porosity, there was a decrease in mechanical strength. Each zone was plotted to its corresponding average elastic modulus with increasing porosity where zone 1 is 5.04%, zone 2 is 11.64%, zone 3 is 17.78%, zone 4 is 25.91%, and zone 5 being the most porous with 34.00% porosity. The error bar indicates the maximum and minimum elastic modulus from the three trials, and the plotted value is the average. Values found from previous research for cortical and trabecular bone in the jawbone were plotted with the experimental average elastic modulus. Notably, depending on the location of the bone in the jaw the mechanical properties vary so a range of elastic modulus of cortical and trabecular bone in the jawbone found from previous literature was compared. The elastic modulus for cortical bone in the jawbone from previous work was 22.8GPa, 20GPa, 17GPa, and 15.85GPa [16], [143], [144], [145]. Trabecular bone was found to have an elastic modulus of 7.95GPa and 0.35GPa [144], [145]. It can be seen that an elastic modulus similar to cortical bone was achieved for porosities at zone 4 and 5, 25.91% and 34.00% respectively. Zone 4 had a minimum and maximum elastic modulus of 17.62GPa and 35.17GPa and zone 5 had a minimum and maximum elastic modulus of 15.06GPa and 24GPa. The implant is in contact with both cortical and trabecular bone, thus, either pore size and porosity combination for zone 4 or 5 can be used as the outermost porous architecture for the functionally graded porous scaffold.

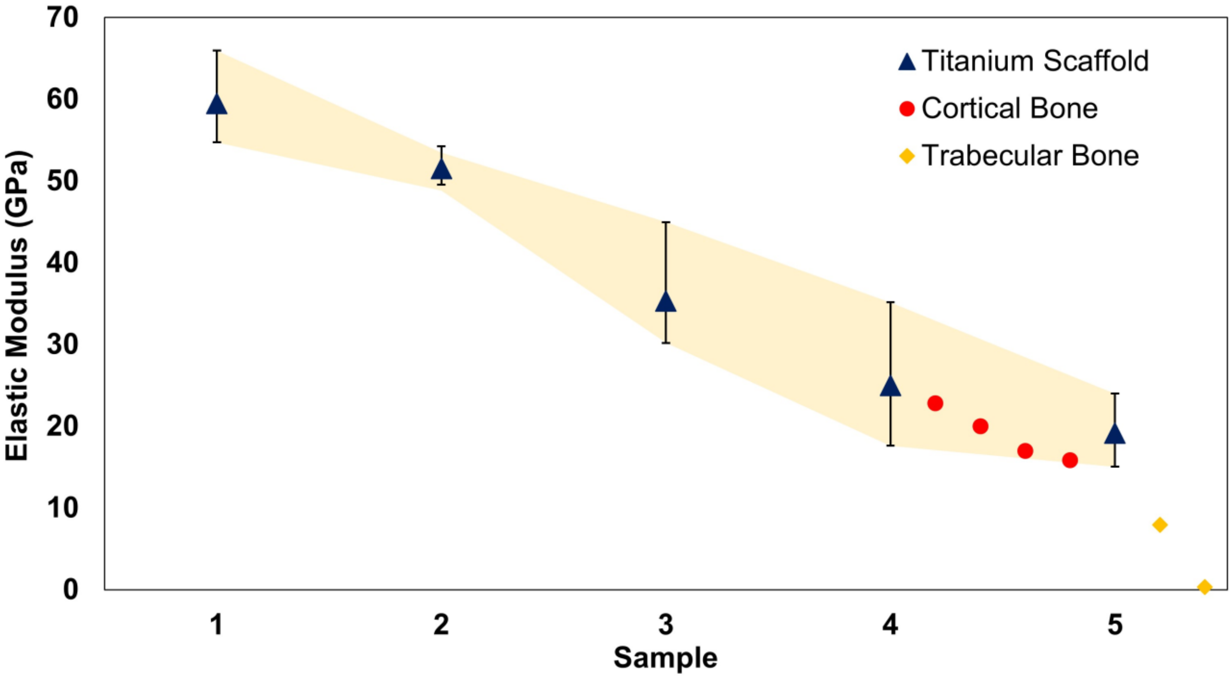

Figure 5.9: The average experimental elastic modulus of the porous structures at the five designed zones in comparison to cortical and trabecular bone.

Since the structure of the samples was altered with induced porosity, it was important to further analyze the fracture behavior of the samples. Visually, the samples fractured in shear, shown in Figure 5.10 (A-E) in ascending order, 5.04%, 11.64%, 17.78%, 25.91%, and 34.00%.

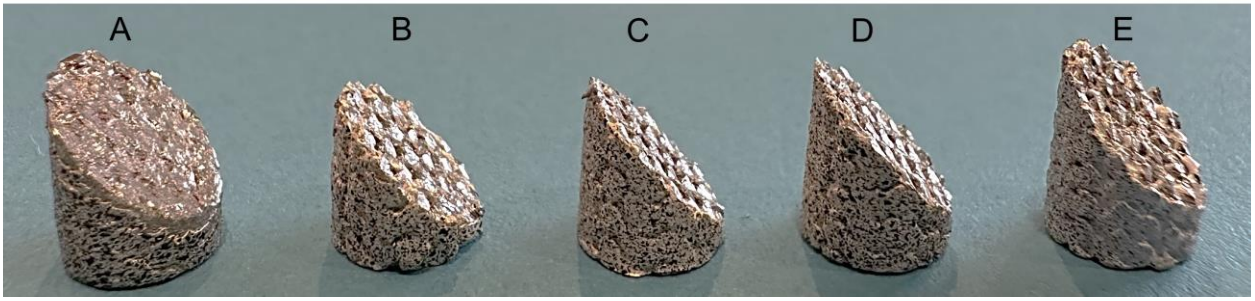

Figure 5.10: Failed samples in shear from the uniaxial compression tests for each porosity. (A) 5.04%, (B) 11.64%, (C) 17.78%, (D) 25.91%, and (E) 34.00%.

The failed samples were then put under a microscope and measured at four points along the line of fracture. An example of the measurement process is shown in Figure 5.11 for the samples with 25.91%. Figure 5.11(A) shows the fracted 25.91% sample with the designated areas marked with a red arrow and separated into four zones. Figure 5.11(B) shows the fractured line under the microscope at the four different zones with 10X magnification. It can be seen that there are ridges along the line of fracture; this could be indicative of the struts between the pores getting caught on each other, causing this feature.

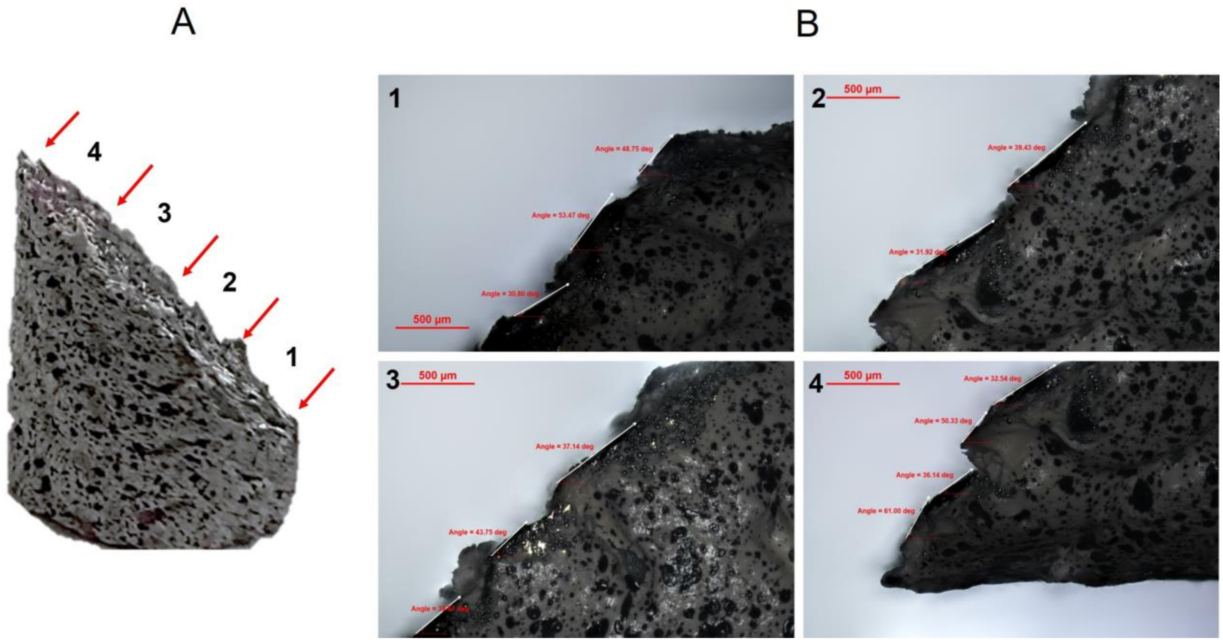

Figure 5.11: Angle measurement across the fracture surface of the 28.74% sample at four different locations characterizing the shear failure mode. (A) Failed scaffold with the designated zone areas analyzed; (B) Corresponding zones under the microscope with 10X magnification.

Table 5.5: The recorded angle at each location across the fracture line for each porous scaffold.

Porosity (%)	**Angle (◦)**			
	1	**2**	**3**	**4**
5.04	63.44	65.95	5.838	59.46
11.64	41.57	51.84	54.14	--
17.78	51.88	58.31	39.26	43.36
25.91	39.43	39.92	51.11	45.00
34.00	48.95	54.22	35.03	55.68

Based on the results in Table 5.5, the angle calculated at each zone along the line for each porosity was close to 45°. This indicates that the samples failed in shear, which is a favorable behavior because the structure will begin to deform, withstanding the load, without catastrophic failure.

The elastic properties and mode of failure were characterized for each scaffold, SEM was used to identify the ductile and brittle failure of the fractures of the scaffolds. It was noticed with decreasing porosity, the increase in ductile fracture. On the other hand, the high porosity structures exhibited ductile and brittle failure, this could be attributed to the struts between the pores with higher energy absorption withstanding the plastic deformation for a longer period before fracture. This is specifically seen in the highest porosity scaffold, 34.00%. We observed a mix of ductile and brittle fracture depending on the location of the pores. This could also have to do with the interlocking of the structs during fracture. There is a tear-like, smooth pattern fracture on some struts indicating a brittle fracture. Figure 5.11 shows the fractured sample with 34.00% porosity under SEM, Figure 5.11(A) shows the entire sample with the area of the struts highlighted that were analyzed under SEM and shown in Figure 5.11 (B-G). Starting from the lower most strut, it is observed that there are high amounts of dimple-like structures formed. This is indicative of ductile behavior. In the upward trend the dimple structures are less indicative of brittle behavior. This trend is consistent for each row of pores parallel to the highlighted region. The bottom half of the sample has more dimples resulting in ductile behavior, the upper half of the sample experiences more brittle failure with low amounts of these dimple structures. This is consistent with previous studies and research [[34], [35]]. Similarly, the 25.91% fractured scaffold had a combination of brittle and ductile fracture with a brittle dominant behavior on the lower half and a ductile dominant behavior on the upper half. This is shown in Figure 5.12 (A-

G). During compression testing, it was observed for both these porosities that an internal fracture occurred around 6kN for the 25.91% porous sample and about 4kN for the 34.00% porous sample. After this then there was a full fracture where the samples separated into two pieces, as shown in DIC. In one of the trials for the 25.91% porous sample, the sample also fractured at the bottom of the sample and broke into three pieces. This could be indicative of the layer-by-layer "crush" that occurs in lattices. This also means that sudden failure or catastrophic failure is avoided.

The 17.78% porous samples, the fracture behavior was the same in that there was ductile and brittle behavior of crack propagation. The samples fractured in shear and there was no internal fracture observed during the compression test before complete failure. The fracture behavior of the sample is shown in Figure 5.14. The left area experienced the more ductile behavior, and moving to the right diagonally, the brittle behavior is observed. The fractured porous sample with a porosity of 11.64% under SEM is shown in Figure 5.15. Similar to the 17.71% porous sample fracture, there was a ductile dominant failure on the left side of the sample where, as moving diagonally to the right, a brittle dominant failure is observed. An interesting observation was made, where there is cracking along the struts shown in the magnified highlighted orange region in Figure 5.15. It can be said that there was a horizontal fracture surface in the struts. This was not observed among the other samples tested.

In the 5.04% manufactured failed sampled, showing in Figure 5.16 the pores and struts were not as prominent. There was an abundance of partially melted powder observed that are attached to the walls between the pores. There was ductile behavior around the edges with brittle dominant behavior in the center. This could be because the outer diameter absorbs all the energy and holds until failure. Similarly, the fully dense sample with 0% porosity, in Figure 5.17, showed a ductile dominant behavior. There were some smooth patterns observed in the center, but there was a dominant ductile mode of fracture.

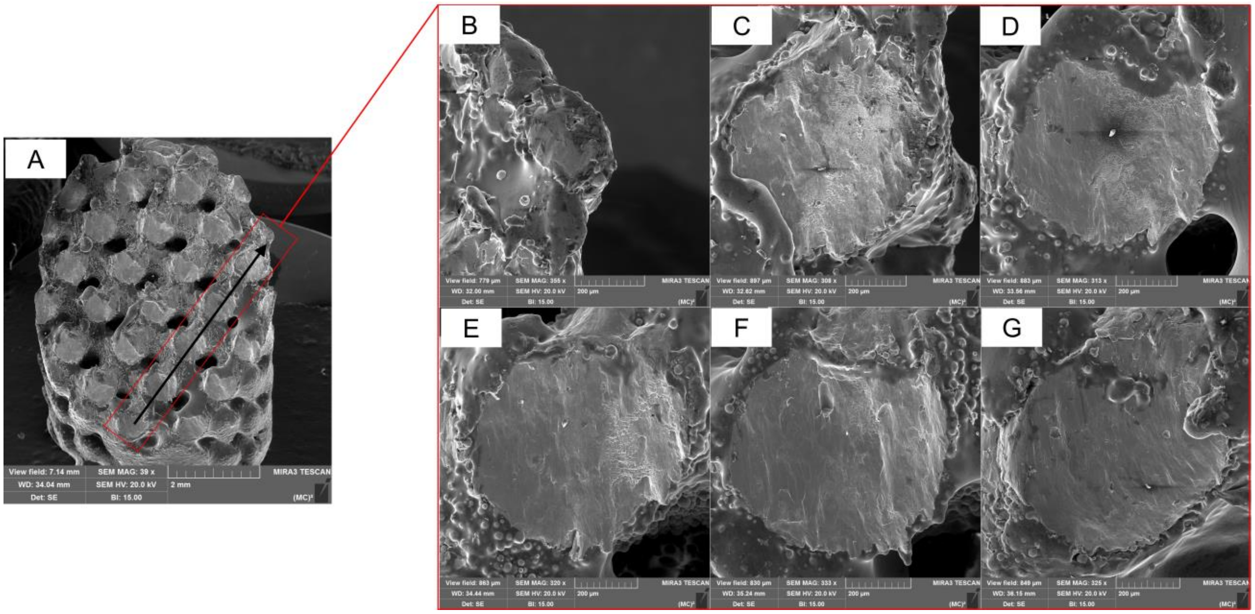

Figure 5.12: (A) SEM of the compression tested 34.00% porous scaffold after failure. (B-G) Each strut along the arrow from the red highlighted region showing the transition from ductile to brittle behavior in an upward trend. (B-D) dimple feature indicating a ductile fracture. (E) Equal parts of the dimple feature and smooth pattern flow indicating a combination of brittle and ductile behavior. (F) Transition from brittle to ductile, (G) smooth pattern indicating a brittle dominant behavior.

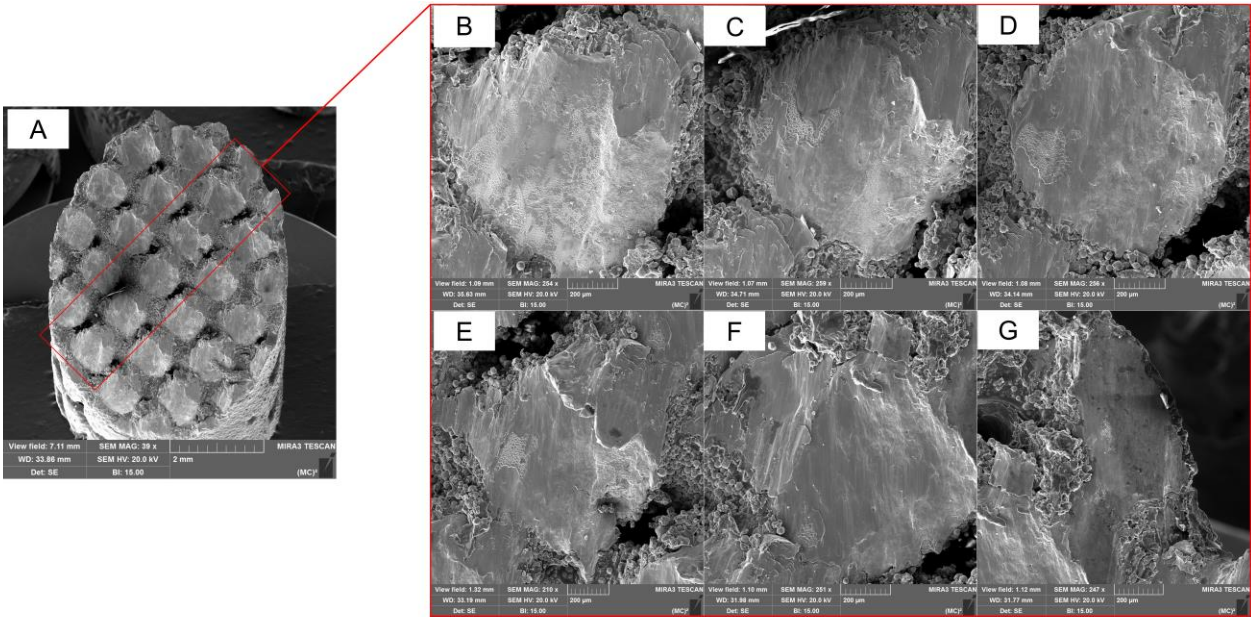

Figure 5.13: (A) SEM of the compression tested 25.91% porous scaffold after failure. (B-G) Each individual surface of the strut along the red highlighted region in the direction of the arrow showing the transition from ductile to brittle behavior in an upward trend. (B-E) dimple feature indicating a ductile fracture. (E) Dimple feature and smooth pattern flow indicating the transitions from ductile to brittle behavior. (F-G) Smooth dominant pattern indicating a brittle behavior.

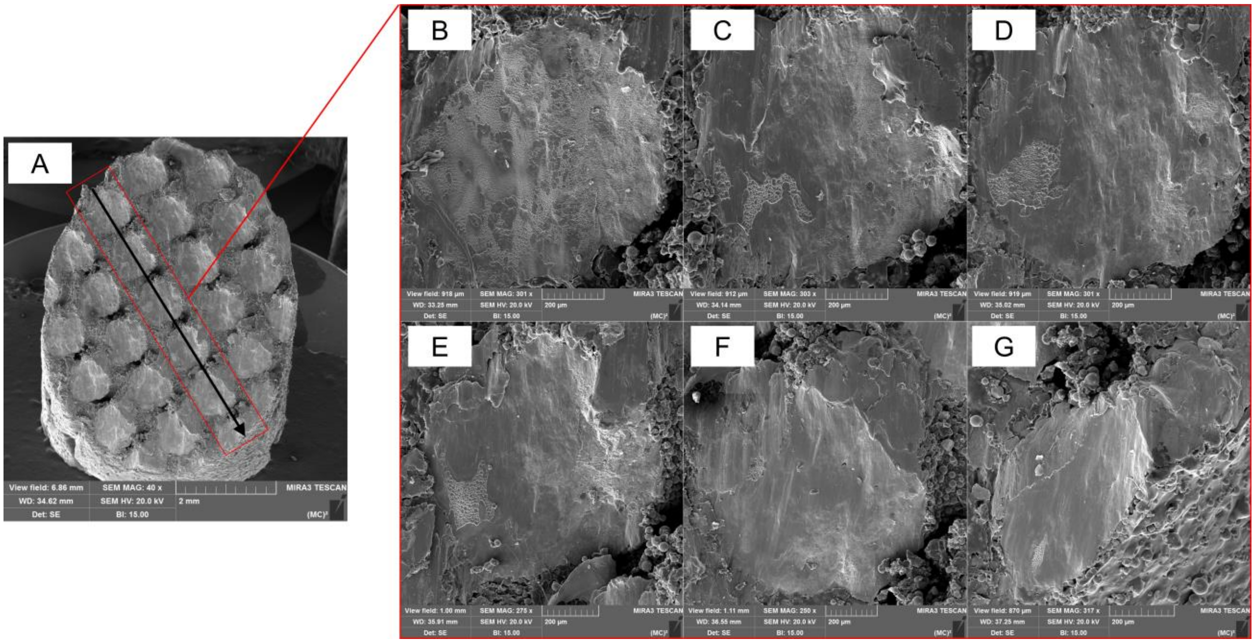

Figure 5.14: (A) SEM of the compression tested 17.78% porous scaffold after failure. (B-G) Each individual surface of the strut along the red highlighted region in the direction of the arrow showing the transition from ductile to brittle behavior in a downward trend. (B,C) dimple feature indicating a ductile fracture. (D, E) Dimple feature and smooth pattern flow indicating the transitions from ductile to brittle behavior. (F-G) Smooth dominant pattern indicating a brittle behavior.

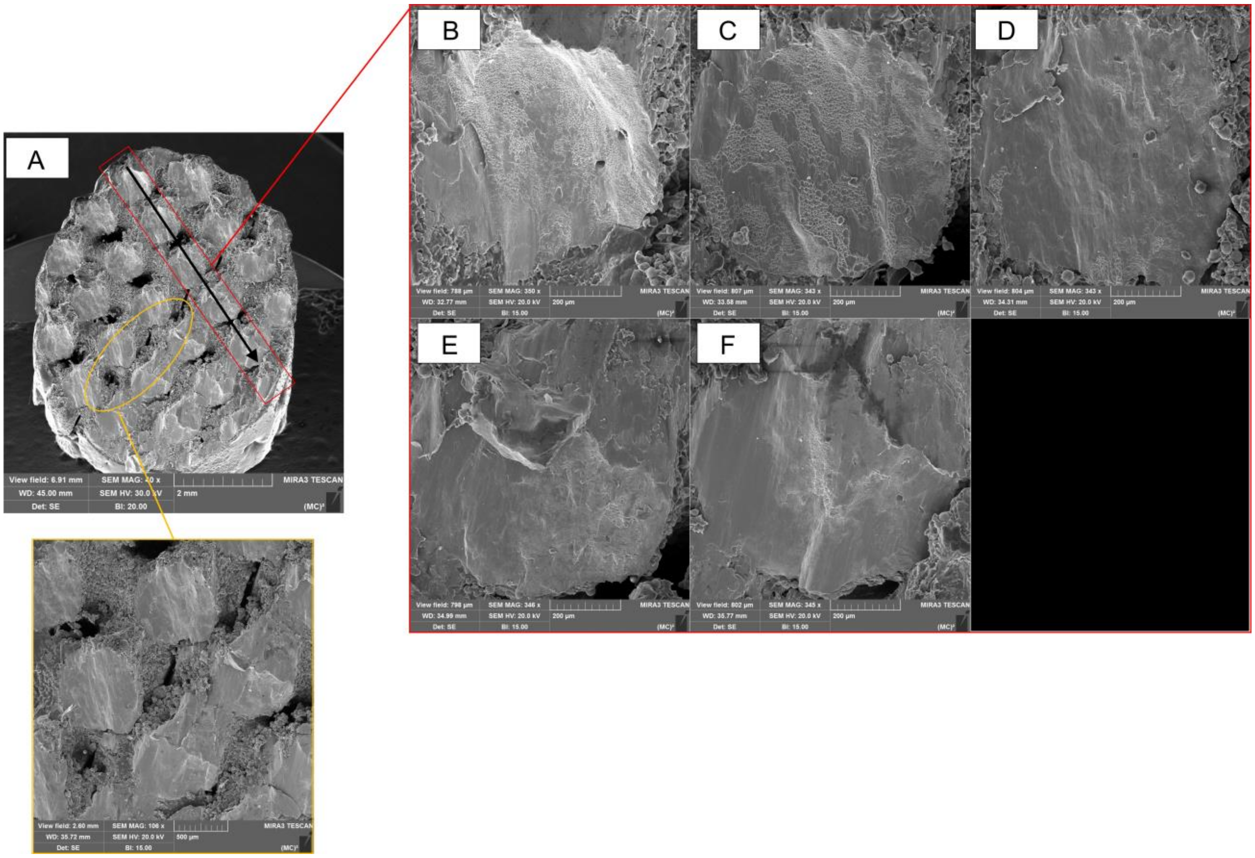

Figure 5.15: (A) SEM of the compression tested 11.64% porous scaffold after failure. (B-F) Each individual surface of the strut along the red highlighted region in the direction of the arrow showing the transition from ductile to brittle behavior in an downward trend. The highlighted orange region showed fractures in the vertical direction along the horizontal struts. (B,C) dimple feature indicating a ductile fracture. (D, E) Dimple feature and smooth pattern flow indicating the transitions from ductile to brittle behavior. (F) Smooth dominant pattern indicating a brittle behavior.

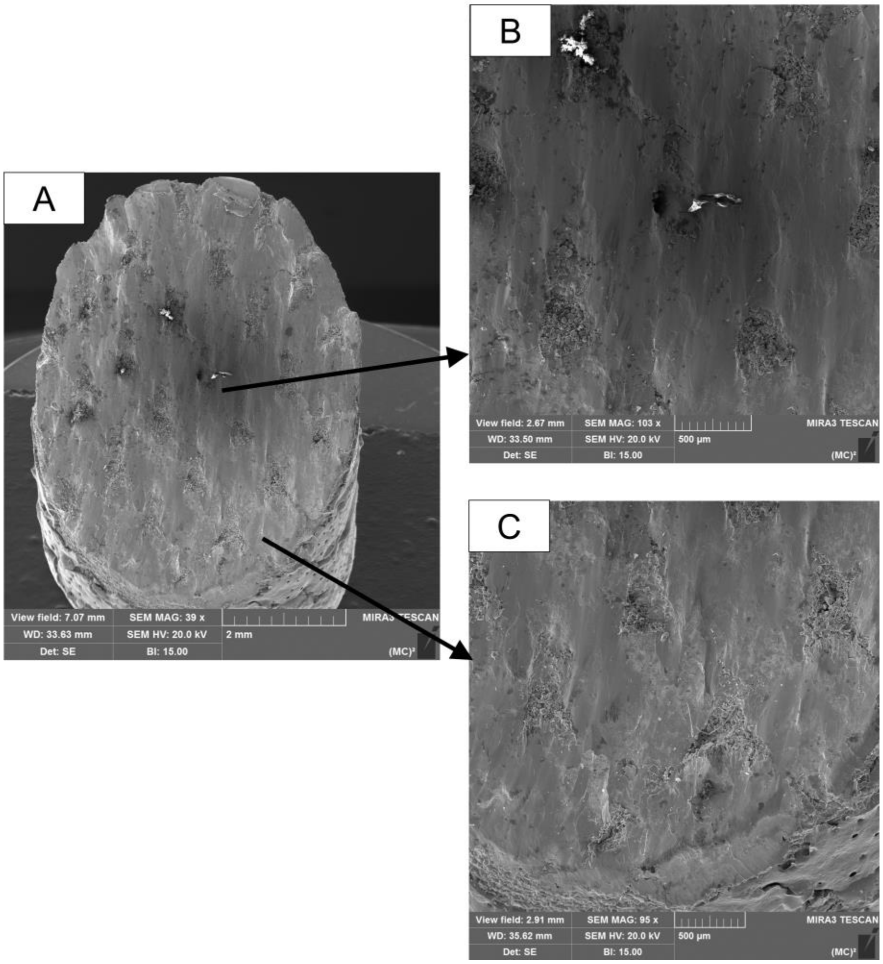

Figure 5.16: (A) SEM of the compression tested 5.04% porous scaffold after failure. (B) The center of the sample had a smooth flow pattern correlating to brittle behavior. (C) The presence of the dimple features was present around the perimeter of the sample correlating to ductile behavior.

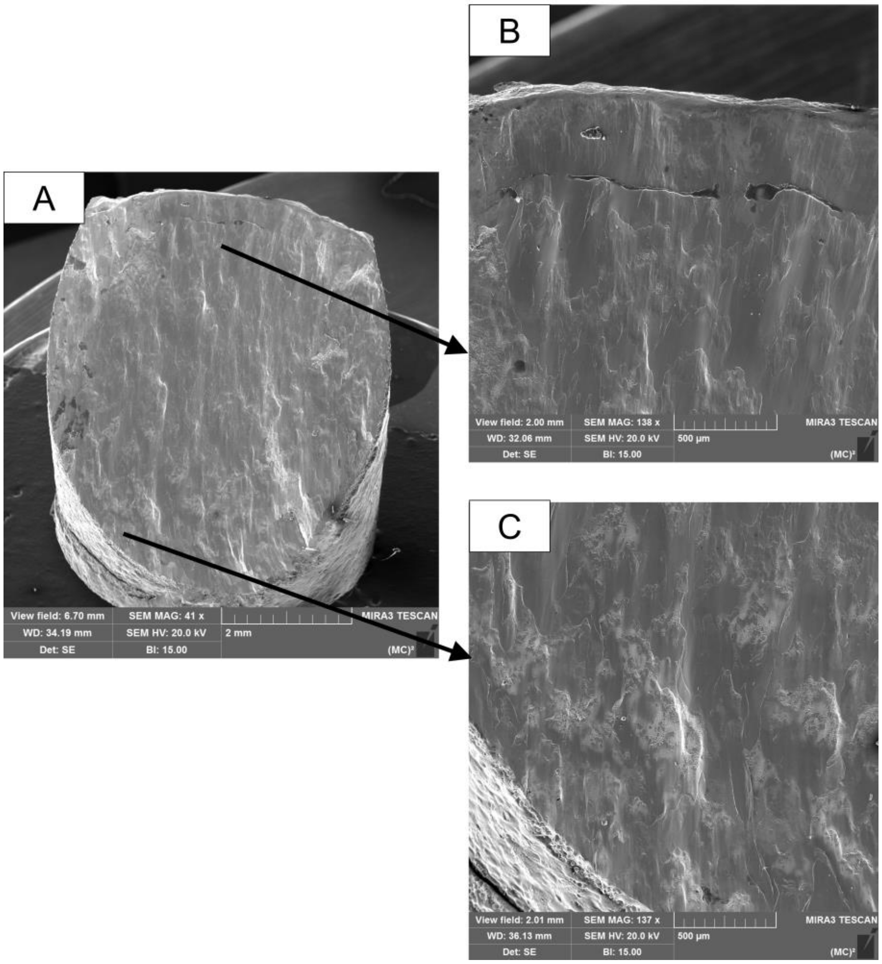

Figure 5.17: (A) SEM of the compression tested fully dense scaffold after failure. (B) The center of the sample had a dimple like dominant feature with some smooth pattens correlating to ductile fracture with the presence of brittle fracture. (C) The dimple features was present around the perimeter of the sample correlating to ductile behavior.

5.4 Conclusions

Functionally graded porous materials are the optimal design architecture for dental implant scaffolds. The main contribution of this work was to develop and characterize a set of TPMS solid gyroid structures with increasing pore size and porosity for the purpose of creating a functionally graded porous structure. The theoretical model for developing the porous structures could be used as an initial starting point for the set of designs, but tuning of the equation needs to further be done to be used as a predicted model. The inducement of pores in a bulk titanium material alters the structural properties thus careful and thorough characterization is needed. Although previous works reported elastic modulus and studies on the material characterization of TPMS gyroid structures and cellular structures, the gap remains that the cell size, pore size, and wall thickness parameters varied from each study, affecting the elastic modulus outputs. The failure mechanisms remained similar. Further, we developed the compression test using digital image correlation (DIC); this allowed us to analyze this small-sized microporous structure in real-time to fully understand the behavior in compression. It is important that we develop a structure mitigating catastrophic failure for the safety of patients. This study showed promising results for the next generation of dental implants inducing a functionally graded TPMS gyroid porous architecture. The implementation of DIC as the strain measurement during the compression test allowed for more accurate characterization of the strain behavior. The results indicated potential for enhanced mechanical properties beyond mimicking the elastic modulus of bone to reduce the stress shielding effect. Song et al, showed no stress shielding effect for an FEA simulation with a gyroid structure with 30% and 40% porosity [13]. We hypothesize the designed and manufactured porous samples had a reduction in stress shielding.

A noteworthy observation of the fracture behavior during compression testing, from the cameras of the DIC setup, led to the hypothesis of crack arrest occurring. The crack arrest behavior was noticed and noted for the higher porosity samples, 25.74% and 34.00%. These higher porosity samples showed an initial cracking at approximately 6kN for the 25.74% sample and 5kN for the 34.00% samples then continued to absorb the load applied until full fracture. This indicates the potential for a higher-strength structure that will delay failure and, in turn, restrict catastrophic failure. The scanning electron microscopy (SEM) results agreed with this behavior in that we saw a combination of ductile and brittle failure. Ductile failure shows us that there was load absorbed before failure occurred.

Each porous sample is sufficient enough to withstand physiological loading, thus it is vital to take into account all aspects of the characterization of these structures. This includes interconnectivity, mode of failure, and resolution. 2D DIC showed to be effective as a non-contact strain gauge, although with the cylindrical nature of the samples, 3D DIC would be needed to study this further to get a global view of the sample and its deformation.

In conclusion, the choice for the potential for the optimal functionally graded porous architecture would include the 5.04%, 17.78%, and 34.00% porosity. This is because the samples have a large enough porosity difference to fabricate a functionally graded structure while maintaining mechanical strength. Each structure retained its interconnectivity from SLM. Further experiments need to be conducted to study the optimal choice. Fatigue testing needs to be conducted to encompass the full characterization and use of the TPMS solid gyroid. This work aimed to achieve a TPMS solid gyroid functionally graded porous scaffold for dental implants with mechanical integrity and interconnectivity.

Chapter 6 Conclusions and Future Works

6.1 Contributions and Key Findings

This work established a framework for designing, developing, and fabricating an additively manufactured functionally graded porous Ti6Al4V scaffold with a dense core as an alternative to current dental implant solutions. The aim was to develop a porous architecture embedded within the structures to promote the ingrowth of bone for enhanced biological performance, simultaneously reducing stress shielding, and to address the main research gaps of bone loss in medically compromised patients along with reducing bone resorption long term. The Voronoi stochastic, random and non-uniform, and the triply periodic minimal surface (TPMS) gyroid, uniform and periodic lattice structures have been researched. This research aimed to compare the two variants of TPMS structures, sheet and solid, and the Voronoi stochastic structures related to manufacturability, biological performance, and mechanical characteristics. It was also important to further understand the limitations, geometric constraints, and effects of additive manufacturing on the TPMS gyroid and Voronoi stochastic porous structures. Chapter 3, Chapter 4, and Chapter 5 built upon each other to gain insight into the optimal porous architecture based on additive manufacturing, cell culturing, and mechanical performance to finally choose the optimal combination of pore and pore sizes for a functionally graded structure.

In Chapter 3, the framework for design and additive manufacturing of TPMS gyroid and Voronoi stochastic structures was established. The minimum pore size to achieve interconnectivity for the lattice structures were designed, additively manufactured, and analyzed from micro computed tomography scans. The porosity distribution, interconnectivity, pore size, and pore size revealed that for the Voronoi stochastic lattice and the TPMS sheet and solid gyroid variants the minimum pore size to achieve optimal interconnectivity was a designed pore size and porosity of 250µm and 38.39%, 200µm and 51.10%, and 220µm and 32.57%. The corresponding manufactured pore size and porosities are 214.90 ± 140.00µm and 19.00%, 197.74 ± 91.49µm and 18.81%. and 153.28 ± 60.92µm and 19.91%. Ultimately, the TPMS solid gyroid had the lease amount of porosity distribution with the optimal manufacturability in relation to interconnectivity and resolution.

The work in Chapter 4, seeks to identify the biological performance of the SLM fabricated TPMS sheet gyroid, TPMS solid gyroid, and Voronoi stochastic structures with designed pore sizes and porosities of 250µm and 38.39%, 200µm and 51.10%, and 220µm and 32.57%. Each construct was cell-seeded, and a set of experiments was conducted to analyze the cell adhesion properties, pore morphology behavior with the cells, and cell infiltration. Chapter 3 indicated that the TPMS solid gyroid had the highest manufactured resolution and interconnectivity, it was hypothesized that the TPMS solid gyroid would outperform in comparison to the TPMS sheet gyroid and Voronoi stochastic structures. The RNA extraction revealed that the TPMS solid gyroid had the highest RNA quantity, indicating that the cells favored this structure. The images from scanning electron microscopy (SEM) showed a uniform cellular matrix on the TPMS solid gyroid scaffold also indicating that this was the most favorable for cells. SEM also revealed the unmelted powder particles as a result from additive manufacturing and were apparent on all structures. The results from RNA extraction and SEM allowed us to eliminate the TPMS sheet gyroid as it underperformed in comparison to the Voronoi stochastic and TPMS solid gyroid structure. The lack of research comparing the non-uniform stochastic and TPMS structures was a driving factor in not eliminating the Voronoi stochastic structure. To further understand the cell trajectory and penetration of the pores, cross-sectional samples were SLM fabricated and cell seeded and analyzed using fluorescent confocal microscopy. Thus, further revealing that the TPMS solid gyroid in fact had the highest interconnectivity and more favorable environment of for cells. A greater number of pores are cellularized in the TPMS gyroid compared to Voronoi stochastic. Additionally, the cell trajectory profile comparison within a single pore indicated the Voronoi stochastic is significantly steeper than the TPMS, which may negatively influence cell migration, integration, and occlude vascular ingrowth critical to subsequent bone formation. In parallel to the cell culturing experiments, the solid-modeled pores from the micro computed tomography outputs of the fabricated samples were simulated in the environment of the in vitro cell culturing experiments performed and in the environment of human blood. Utilizing the solid models of micro-CT scans of the fabricated samples allowed for a more accurate comparison of the permeability. The TPMS solid gyroid had values within the range of human and bovine bone. Thus, in this chapter the design with the best interaction with cells was chosen to further optimize and test for its mechanical performance. The TPMS solid gyroid was chosen for further experimenting to characterize the mechanical performance and properties to now mitigate the stress shielding effect.

The work in Chapter 5 investigated a range of combinations of pore size and porosities to test the mechanical properties of a TPMS solid gyroid structure. An analytical model was used to design and fabricate a set of five fully porous samples. The analytical model outputs the theoretical elastic modulus for a given porosity at a certain point across the fully dense structure. Based on the optimal pore sizes for bone ingrowth this was put in combination with the theoretical prosody values. Thus, five designs with pore size and porosity of 10% and 130μm, and 20% and 120μm was designed as cylindrical samples. These were designed as fully porous samples, with the intention of applying them each as a functionally graded porous structure. We developed the compression test with 2D digital image correlation (DIC) to output the displacement and strain values more accurately. The samples were 5mm in diameter and 7.5mm in height with microporous TPMS designs. Thus, DIC was shown to be a promising measurement of strain during compression testing. These experiments showed that the elastic modulus was significantly reduced compared to that of fully dense Ti6Al4V. The designed 50% porous structure with a manufactured porosity of 34.00% had the lowest average elastic modulus of 18.43 GPa and performed well during the compression test. The 5.04% porosity showed to have a high elastic modulus of 52.56 GPa and fractured similar to a bulk metallic material. The 17.78% porous sample with a pore size of 168.20 ±75.16μm, showed to have an average elastic modulus of 34.52 GPa between the 5.04% and 34.00% porous samples. We concluded that the porosity and average pore size combination of the 5.04% and 69.47 ±44.76μm, 17.78% and 168.20 ±75.16μm, and 34.00% and 300.45 ±108.65μm would be a good fit for a functionally graded porous structure where there could be a smooth transition across the varying porosities. The values are far enough to enable a functionally graded porous structure, with pore sizes conducive to bone ingrowth, cell adhesion, and favorable mechanical properties to mitigate the stress shielding effect.

6.2 Future Works

The findings in this work fostered opportunities for further research and optimization of additively manufactured porous titanium implants. The opportunities and suggestions are outlined in this section.

6.2.1 Surface Topography Effects from Selective Laser Melting

In Chapter 4, the SLM fabricated structures showed unmelted powders on the surfaces of the porous structures and on the surfaces within the pores. It is important to remove the unmelted powders, based on their angle of contact they are considered harmless or can be ignored. It is proposed to conduct experiments for acid etching utilizing hydrofluoric acid to remove the unmelted powders, then conduct the in vitro cell culturing experiments again as well as calculate the pore size and porosity. Previous studies showed minimal differences between acid etched samples and the samples with unmelted pores, but showed an increasing pore size and porosity closer to the designed models after etching.

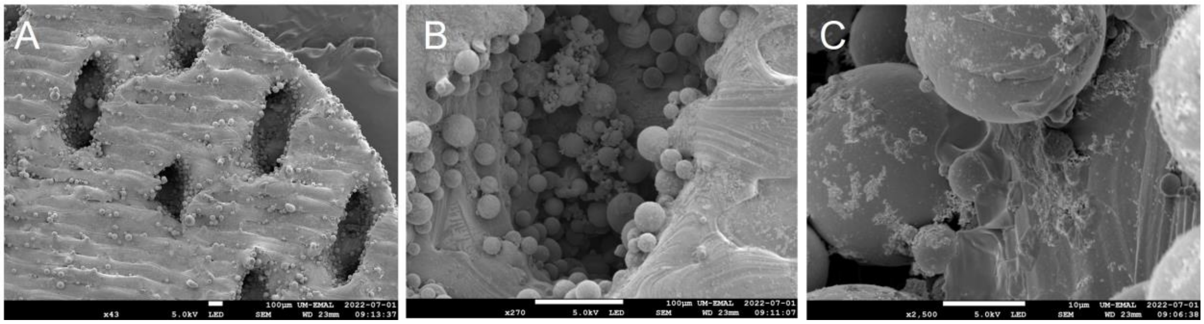

Figure 6.1: Scanning electron microscopy of the TPMS solid gyroid. (A) Top view of pores, (B) magnified top view within the pores, and (C) magnified view of the unmelted powder within the pores.

6.2.2 Mechanical Characterization of TPMS solid gyroid structures of its intended use

Although the elastic properties of the TPMS solid gyroid structures were shown to reduce the elastic modulus, thus concluding the potential for the reduction of stress shielding, the implant responsibility performs under fatigue. The behavior of the samples under fatigue would be valuable to characterize the samples' life cycle. In general fatigue strength is lower than its compressive strength. It is important to characterize the TPMS solid gyroid pore size and porosity combinations chosen as most optimal from this research to test in fatigue to ensure a fatigue strength deemed safe for dental implant applications; this is, it can withstand 10^6 cycles of cyclic loading or when the scaffold loses 90% of its initial strength. Another standard, ISO 14801:2016, suggests loading the geometry at a 30-degree angle. The fatigue strength is measured at the point of 10^6 if there if no debris found.

6.2.3 In-Vivo Animal Testing

This work is currently under study and awaiting results. It is important to understand the effects of the cell interaction and bone ingrowth within the pores in an animal model. The porous scaffold is implanted in the femur or tibia to mimic the constant load and unloading of the implant. The dimensions are 2mm diameter and 4mm length. The Voronoi stochastic and TPMS solid gyroid structures were both designed, manufactured, and implanted with a pore size of 250µm and 34.95% porosity. The TPMS solid gyroid was designed with a 200µm pore size and 32.57% porosity. These values were intended to be consistent with the in-vitro pore size and porosity to maintain an equitable comparison. Figure 6.2 shows the designed samples of the TPMS solid gyroid and Voronoi stochastic structure with a solid core. The results from the in-vivo experiments will give comprehensive insight into the behavior of osseointegration and if it was enhanced. The in-vitro experiments concluded the possibility for enhanced osseointegration based on cell adhesion and proliferation, which is positively correlated with osseointegration. However, osseointegration is measured by measuring the bone-to-implant contact within the pores and surrounding the implant, thus in-vivo experiments are needed.

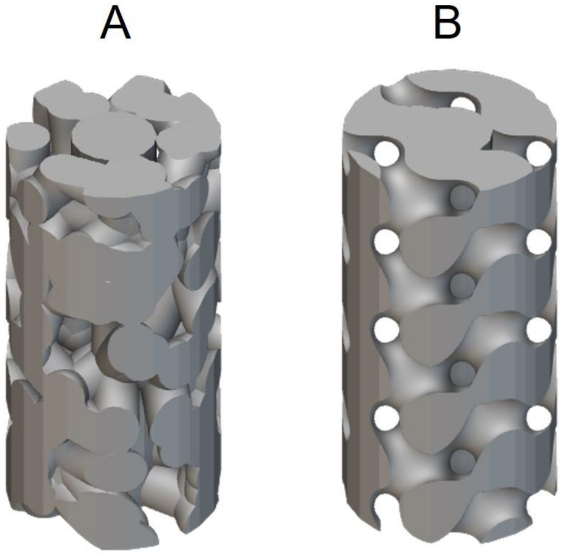

Figure 6.2: Porous scaffolds for In-vivo experiments. (A) Voronoi stochastic scaffold, (B) TPMS solid gyroid scaffold.

6.2.4 Artificial Intelligence for the Design of Spinodal Patient-specific Porous Implants

The preliminary work was in collaboration with post-doctoral student Zhuo Wang at the University of Michigan. A computational data-driven model was established to train the neural network to design a specific porosity, pore size, and interconnected network with a solid core. Figure 6.3 shows a 40% porous cylindrical spinodal structure designed using the neural network model and the cross-section indicating favorable interconnectivity. Based on the developed framework for designing, additively manufacturing, and experimenting both biologically and mechanically the same method should be applied to the spinodal structures developed with the data driven model. The purpose of this research is to identify another solution for designing patient-specific porous implants. This would theoretically make it more attainable to design and manufacture customized implants on-site for clinicians.

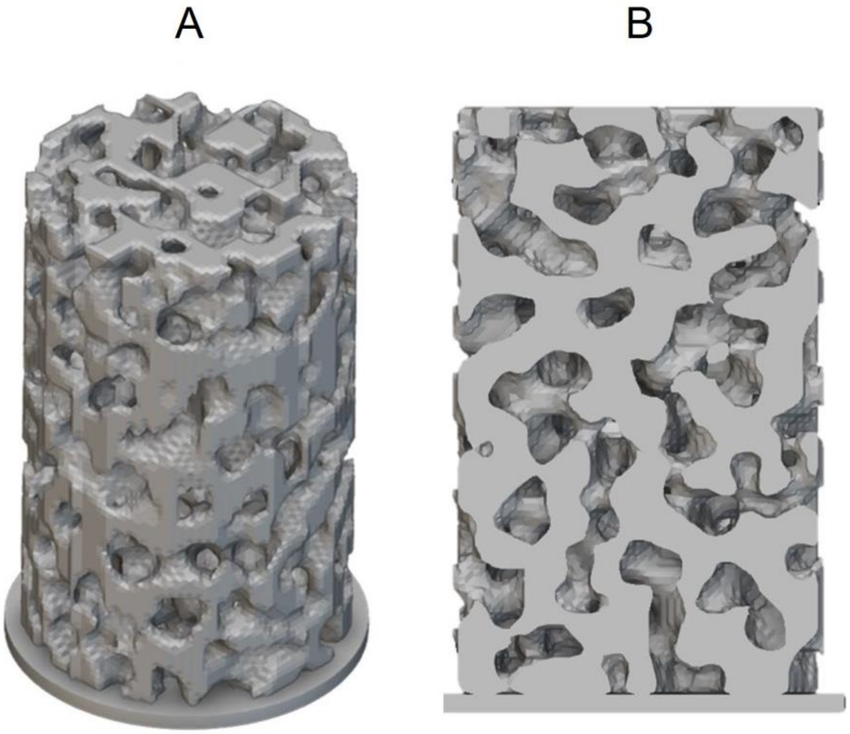

Figure 6.3: (A) Spinodal structure with 40% porosity designed with the data-driven model. (B) Cross-section of the spinodal structure indicating interconnectivity.

Bibliography

[1] "Dental implants market size, share: Growth Analysis [2030]," https://www.fortunebusinessinsights.com/industry-reports/dental-implants-market-100443. Accessed: Sep. 04, 2023. [Online]. Available: https://www.fortunebusinessinsights.com/industry-reports/dental-implants-market-100443

[2] A. Parihar, S. Madhuri, R. Devanna, G. Sharma, R. Singh, and K. Shetty, "Assessment of failure rate of dental implants in medically compromised patients," J Family Med Prim Care, vol. 9, no. 2, p. 883, 2020, doi: 10.4103/jfmpc.jfmpc_989_19.

[3] H. S. Alghamdi, "Functional Biomaterials Methods to Improve Osseointegration of Dental Implants in Low Quality (Type-IV) Bone: An Overview", doi: 10.3390/jfb9010007.

[4] Z. J. Wally et al., "Porous Titanium for Dental Implant Applications," Metals (Basel), vol. 5, 2015, doi: 10.3390/met5041902.

[5] S. Parithimarkalaignan and T. V. Padmanabhan, "Osseointegration: An Update," The Journal of Indian Prosthodontic Society, vol. 13, no. 1, pp. 2–6, Mar. 2013, doi: 10.1007/s13191-013-0252-z.

[6] C.-P. Hao, N.-J. Cao, Y.-H. Zhu, and W. Wang, "The osseointegration and stability of dental implants with different surface treatments in animal models: a network meta-analysis," Sci Rep, vol. 11, no. 1, p. 13849, Jul. 2021, doi: 10.1038/s41598-021-93307-4.

[7] H. Alghamdi, “Methods to Improve Osseointegration of Dental Implants in Low Quality (Type-IV) Bone: An Overview,” J Funct Biomater, vol. 9, no. 1, p. 7, Jan. 2018, doi: 10.3390/jfb9010007.

[8] L. Zhang, B. Song, S. K. Choi, and Y. Shi, “A topology strategy to reduce stress shielding of additively manufactured porous metallic biomaterials,” Int J Mech Sci, vol. 197, p. 106331, May 2021, doi: 10.1016/J.IJMECSCI.2021.106331.

[9] A. Ouldyerou, A. Merdji, L. Aminallah, S. Roy, H. Mehboob, and M. Ozcan, “Biomechanical performance of Ti-PEEK dental implants in bone: An in-silico analysis,” 2022, doi: 10.1016/j.jmbbm.2022.105422.

[10] F. J. Quevedo González et al., “Mechanical performance of cementless total knee replacements: It is not all about the maximum loads,” Journal of Orthopaedic Research®, vol. 37, no. 2, pp. 350–357, Feb. 2019, doi: 10.1002/jor.24194.

[11] Y. Ichioka, F. Asa’ad, B. Ö. Malekzadeh, A. Westerlund, and L. Larsson, “Epigenetic changes of osteoblasts in response to titanium surface characteristics,” J Biomed Mater Res A, vol. 109, no. 2, pp. 170–180, Feb. 2021, doi: 10.1002/jbm.a.37014.

[12] R. Osman and M. Swain, “A Critical Review of Dental Implant Materials with an Emphasis on Titanium versus Zirconia,” Materials, vol. 8, no. 3, pp. 932–958, Mar. 2015, doi: 10.3390/ma8030932.

[13] M. Umar Farooq, M. Pervez Mughal, N. Ahmed, N. Ahmad Mufti, A. M. Al-Ahmari, and Y. He, “On the Investigation of Surface Integrity of Ti6Al4V ELI Using Si-Mixed Electric Discharge Machining,” Materials, vol. 13, no. 7, p. 1549, Mar. 2020, doi: 10.3390/ma13071549.

[14] M. P. Mughal et al., “Surface modification for osseointegration of Ti6Al4V ELI using powder mixed sinking EDM,” J Mech Behav Biomed Mater, vol. 113, p. 104145, Jan. 2021, doi: 10.1016/j.jmbbm.2020.104145.

[15] C. E. Misch, Z. Qu, and M. W. Bidez, “Mechanical properties of trabecular bone in the human mandible: Implications for dental implant treatment planning and surgical placement,” Journal of Oral and Maxillofacial Surgery, vol. 57, no. 6, pp. 700–706, Jun. 1999, doi: 10.1016/S0278-2391(99)90437-8.

[16] Marina Ayoub Farag, “Variation in the mechanical properties of the human mandibular bone,” RWTH Aachen University, 2015.

[17] J. M. Jung and C. S. Kim, “Analysis of stress distribution around total hip stems custom-designed for the standardized Asian femur configuration,” Biotechnol Biotechnol Equip, vol. 28, no. 3, p. 525, May 2014, doi: 10.1080/13102818.2014.928450.

[18] S. A. Naghavi et al., “Stress Shielding and Bone Resorption of Press-Fit Polyether–Ether–Ketone (PEEK) Hip Prosthesis: A Sawbone Model Study,” Polymers (Basel), vol. 14, no. 21, Nov. 2022, doi: 10.3390/POLYM14214600.

[19] A. Sakkas, F. Wilde, M. Heufelder, K. Winter, and A. Schramm, “Autogenous bone grafts in oral implantology—is it still a ‘gold standard’? A consecutive review of 279 patients with 456 clinical procedures,” Int J Implant Dent, vol. 3, no. 1, p. 23, Dec. 2017, doi: 10.1186/s40729-017-0084-4.

[20] M. P. Ferraz, “Bone Grafts in Dental Medicine: An Overview of Autografts, Allografts and Synthetic Materials,” Materials, vol. 16, no. 11, p. 4117, May 2023, doi: 10.3390/ma16114117.

[21] A. H. Schmidt, “Autologous bone graft: Is it still the gold standard?,” Injury, vol. 52, pp. S18–S22, Jun. 2021, doi: 10.1016/j.injury.2021.01.043.

[22] A. Oryan, S. Alidadi, A. Moshiri, and N. Maffulli, “Bone regenerative medicine: classic options, novel strategies, and future directions,” J Orthop Surg Res, vol. 9, no. 1, p. 18, Dec. 2014, doi: 10.1186/1749-799X-9-18.

[23] R. Zhao, R. Yang, P. R. Cooper, Z. Khurshid, A. Shavandi, and J. Ratnayake, “Bone Grafts and Substitutes in Dentistry: A Review of Current Trends and Developments,” Molecules, vol. 26, no. 10, p. 3007, May 2021, doi: 10.3390/molecules26103007.

[24] M. Clementini, A. Morlupi, C. Agrestini, and L. Ottria, “Success rate of dental implants inserted in autologous bone graft regenerated areas: a systematic review.,” Oral Implantol (Rome), vol. 4, no. 3–4, pp. 3–10, Jul. 2011.

[25] S.-H. Kim, N.-S. Oh, and H.-J. Kim, “Survival Rates and Clinical Outcomes of Implant Overdentures in Old and Medically Compromised Patients,” Int J Environ Res Public Health, vol. 19, no. 18, p. 11571, Sep. 2022, doi: 10.3390/ijerph191811571.

[26] S. M. Beschnidt et al., “Implant success and survival rates in daily dental practice: 5-year results of a non-interventional study using CAMLOG SCREW-LINE implants with or without platform-switching abutments,” Int J Implant Dent, vol. 4, no. 1, p. 33, Dec. 2018, doi: 10.1186/s40729-018-0145-3.

[27] M. H. Taherian, M. Rezazadeh, and A. Taji, “Optimum Surface Roughness for Titanium-Coated PEEK Produced by Electron Beam PVD for Orthopedic Applications,” Materials Technology, vol. 37, no. 8, pp. 631–644, Jul. 2022, doi: 10.1080/10667857.2020.1868209.

[28] M. Sarraf, E. Rezvani Ghomi, S. Alipour, S. Ramakrishna, and N. Liana Sukiman, “A state-of-the-art review of the fabrication and characteristics of titanium and its alloys for

biomedical applications," Biodes Manuf, vol. 5, no. 2, pp. 371–395, Apr. 2022, doi: 10.1007/s42242-021-00170-3.

[29] S. Kligman et al., "Clinical Medicine The Impact of Dental Implant Surface Modifications on Osseointegration and Biofilm Formation," J. Clin. Med, vol. 10, p. 1641, 2021, doi: 10.3390/jcm10081641.

[30] A. Nasar, "Hydroxyapatite and its coatings in dental implants," in Applications of Nanocomposite Materials in Dentistry, Elsevier, 2019, pp. 145–160. doi: 10.1016/B978-0-12-813742-0.00008-0.

[31] R. Family, M. Solati-Hashjin, S. Namjoy Nik, and A. Nemati, "Surface modification for titanium implants by hydroxyapatite nanocomposite.," Caspian J Intern Med, vol. 3, no. 3, pp. 460–5, 2012.

[32] P. Schupbach, R. Glauser, and S. Bauer, "Al_2O_3 Particles on Titanium Dental Implant Systems following Sandblasting and Acid-Etching Process," Int J Biomater, vol. 2019, pp. 1–11, Jun. 2019, doi: 10.1155/2019/6318429.

[33] Y. Zhang, K. Gulati, Z. Li, P. Di, and Y. Liu, "Dental Implant Nano-Engineering: Advances, Limitations and Future Directions," Nanomaterials, vol. 11, no. 10, p. 2489, Sep. 2021, doi: 10.3390/nano11102489.

[34] G. Sayin Ozel, O. Inan, A. Secilmis Acar, G. Alniacik Iyidogan, D. Dolanmaz, and G. Yildirim, "Stability of dental implants with sandblasted and acid-etched (SLA) and modified (SLActive) surfaces during the osseointegration period," J Dent Res Dent Clin Dent Prospects, vol. 15, no. 4, pp. 226–231, Dec. 2021, doi: 10.34172/joddd.2021.037.

[35] A. Barfeie, J. Wilson, and J. Rees, “Implant surface characteristics and their effect on osseointegration,” Br Dent J, vol. 218, no. 5, pp. E9–E9, Mar. 2015, doi: 10.1038/sj.bdj.2015.171.

[36] L. Ramos Xavier Coutinho Nascimento, G. Monteiro Torelly, and C. Nelson Elias, “Analysis of bone stress and primary stability of a dental implant using strain and torque measurements,” Saudi Dent J, vol. 35, no. 3, pp. 263–269, Mar. 2023, doi: 10.1016/j.sdentj.2023.01.006.

[37] T. A. Do, H. S. Le, Y.-W. Shen, H.-L. Huang, and L.-J. Fuh, “Risk Factors related to Late Failure of Dental Implant—A Systematic Review of Recent Studies,” Int J Environ Res Public Health, vol. 17, no. 11, p. 3931, Jun. 2020, doi: 10.3390/ijerph17113931.

[38] S. Sakka, K. Baroudi, and M. Z. Nassani, “Factors associated with early and late failure of dental implants,” J Investig Clin Dent, vol. 3, no. 4, pp. 258–261, Nov. 2012, doi: 10.1111/j.2041-1626.2012.00162.x.

[39] Y. Wang, Y. Zhang, and R. J. Miron, “Health, Maintenance, and Recovery of Soft Tissues around Implants,” Clin Implant Dent Relat Res, vol. 18, no. 3, pp. 618–634, Jun. 2016, doi: 10.1111/cid.12343.

[40] S. Dutta, D. Passi, P. Singh, M. Atri, S. Mohan, and A. Sharma, “Risks and complications associated with dental implant failure: Critical update,” Natl J Maxillofac Surg, vol. 11, no. 1, p. 14, 2020, doi: 10.4103/njms.NJMS_75_16.

[41] J. Wagner, J. H. Spille, J. Wiltfang, and H. Naujokat, “Systematic review on diabetes mellitus and dental implants: an update,” Int J Implant Dent, vol. 8, no. 1, pp. 1–21, Dec. 2022, doi: 10.1186/S40729-021-00399-8/TABLES/6.

[42] S. P. Kochar, A. Reche, and P. Paul, “The Etiology and Management of Dental Implant Failure: A Review”, doi: 10.7759/cureus.30455.

[43] H. Naujokat, B. Kunzendorf, and J. Wiltfang, “Dental implants and diabetes mellitus—a systematic review,” Int J Implant Dent, vol. 2, no. 1, Dec. 2016, doi: 10.1186/S40729-016-0038-2.

[44] T. Abu Alfaraj et al., “Optimizing Osseointegration in Dental Implantology: A Cross-Disciplinary Review of Current and Emerging Strategies,” Cureus, Oct. 2023, doi: 10.7759/cureus.47943.

[45] J. M. Lane, J. E. Mait, A. Unnanuntana, B. P. Hirsch, A. D. Shaffer, and O. A. Shonuga, “Materials in Fracture Fixation,” in Comprehensive Biomaterials, Elsevier, 2011, pp. 219–235. doi: 10.1016/B978-0-08-055294-1.00251-8.

[46] D. V. Budei, D.-I. Vaireanu, P. Prepelita, G. Popescu-Pelin, M. Mincu, and I.-A. Ciobotaru, “A comparative morphological study of titanium dioxide surface layer dental implants,” Open Chem, vol. 19, no. 1, pp. 189–198, Feb. 2021, doi: 10.1515/chem-2021-0197.

[47] S. F. Alves and T. Wassall, “In vitro evaluation of osteoblastic cell adhesion on machined osseointegrated implants,” Braz Oral Res, vol. 23, no. 2, pp. 131–136, Jun. 2009, doi: 10.1590/S1806-83242009000200007.

[48] A. O. Ghaziani, R. Soheilifard, and S. Kowsar, “The effect of functionally graded materials on bone remodeling around osseointegrated trans-femoral prostheses,” J Mech Behav Biomed Mater, vol. 118, p. 104426, Jun. 2021, doi: 10.1016/j.jmbbm.2021.104426.

[49] M. CROSS and J. SPYCHER, “Cementless fixation techniques in joint replacement,” in Joint Replacement Technology, Elsevier, 2008, pp. 190–211. doi: 10.1533/9781845694807.2.190.

[50] M. Elsayed, M. Ghazy, Y. Youssef, and K. Essa, “Optimization of SLM process parameters for Ti6Al4V medical implants,” Rapid Prototyp J, vol. 25, no. 3, pp. 433–447, Apr. 2019, doi: 10.1108/RPJ-05-2018-0112.

[51] M. J. Gupte et al., “Pore size directs bone marrow stromal cell fate and tissue regeneration in nanofibrous macroporous scaffolds by mediating vascularization,” Acta Biomater, vol. 82, pp. 1–11, Dec. 2018, doi: 10.1016/j.actbio.2018.10.016.

[52] M. Yamada and H. Egusa, “Current bone substitutes for implant dentistry,” J Prosthodont Res, vol. 62, no. 2, pp. 152–161, Apr. 2018, doi: 10.1016/j.jpor.2017.08.010.

[53] G. Iviglia, S. Kargozar, and F. Baino, “Biomaterials, Current Strategies, and Novel Nano-Technological Approaches for Periodontal Regeneration,” J Funct Biomater, vol. 10, no. 1, p. 3, Jan. 2019, doi: 10.3390/jfb10010003.

[54] J. H. Nam, S. Y. Lee, G. Khan, and E. S. Park, “Validation of the optimal scaffold pore size of nasal implants using the 3-dimensional culture technique,” Arch Plast Surg, vol. 47, no. 04, pp. 310–316, Jul. 2020, doi: 10.5999/aps.2020.00213.

[55] N. Abbasi, S. Hamlet, R. M. Love, and N.-T. Nguyen, “Porous scaffolds for bone regeneration,” Journal of Science: Advanced Materials and Devices, vol. 5, no. 1, pp. 1–9, Mar. 2020, doi: 10.1016/j.jsamd.2020.01.007.

[56] W. B. Swanson et al., “Macropore design of tissue engineering scaffolds regulates mesenchymal stem cell differentiation fate,” Biomaterials, vol. 272, p. 120769, May 2021, doi: 10.1016/j.biomaterials.2021.120769.

[57] L. Zumofen, K. S. Kopanska, E. Bono, A. Kirchheim, E. B. De Haller, and U. Graf-Hausner, “Properties of Additive-Manufactured Open Porous Titanium Structures for Patient-Specific Load-Bearing Implants,” Front Mech Eng, vol. 7, Feb. 2022, doi: 10.3389/fmech.2021.830126.

[58] C. Pan, Y. Han, and J. Lu, “Design and Optimization of Lattice Structures: A Review,” Applied Sciences, vol. 10, no. 18, p. 6374, Sep. 2020, doi: 10.3390/app10186374.

[59] X. Miao and D. Sun, “Graded/Gradient Porous Biomaterials,” Materials, vol. 3, no. 1, pp. 26–47, Dec. 2009, doi: 10.3390/ma3010026.

[60] O. Al-Ketan, D.-W. Lee, R. Rowshan, and R. K. Abu Al-Rub, “Functionally graded and multi-morphology sheet TPMS lattices: Design, manufacturing, and mechanical properties,” J Mech Behav Biomed Mater, vol. 102, p. 103520, Feb. 2020, doi: 10.1016/j.jmbbm.2019.103520.

[61] J. Deering, K. I. Dowling, L.-A. DiCecco, G. D. McLean, B. Yu, and K. Grandfield, “Selective Voronoi tessellation as a method to design anisotropic and biomimetic implants,” J Mech Behav Biomed Mater, vol. 116, p. 104361, Apr. 2021, doi: 10.1016/j.jmbbm.2021.104361.

[62] B. Herath et al., “Mechanical and geometrical study of 3D printed Voronoi scaffold design for large bone defects,” Mater Des, vol. 212, p. 110224, Dec. 2021, doi: 10.1016/j.matdes.2021.110224.

[63] Z. Wang et al., “Biomimetic design strategy of complex porous structure based on 3D printing Ti-6Al-4V scaffolds for enhanced osseointegration”, doi: 10.1016/j.matdes.2022.110721.

[64] C. Han et al., “Continuous functionally graded porous titanium scaffolds manufactured by selective laser melting for bone implants,” J Mech Behav Biomed Mater, vol. 80, pp. 119–127, Apr. 2018, doi: 10.1016/j.jmbbm.2018.01.013.

[65] E. Onal, J. Frith, M. Jurg, X. Wu, and A. Molotnikov, “Mechanical Properties and In Vitro Behavior of Additively Manufactured and Functionally Graded Ti6Al4V Porous Scaffolds,” Metals (Basel), vol. 8, no. 4, p. 200, Mar. 2018, doi: 10.3390/met8040200.

[66] N. Qiu, J. Zhang, C. Li, Y. Shen, and J. Fang, “Mechanical properties of three-dimensional functionally graded triply periodic minimum surface structures,” Int J Mech Sci, vol. 246, p. 108118, May 2023, doi: 10.1016/j.ijmecsci.2023.108118.

[67] S. Pagani et al., “Mechanical and in vitro biological properties of uniform and graded Cobalt-chrome lattice structures in orthopedic implants,” J Biomed Mater Res B Appl Biomater, vol. 109, no. 12, pp. 2091–2103, Dec. 2021, doi: 10.1002/jbm.b.34857.

[68] S. R. Oke et al., “An overview of conventional and non-conventional techniques for machining of titanium alloys,” Manuf Rev (Les Ulis), vol. 7, p. 34, Sep. 2020, doi: 10.1051/mfreview/2020029.

[69] S. Huang, H. Wei, and D. Li, “Additive manufacturing technologies in the oral implant clinic: A review of current applications and progress,” Front Bioeng Biotechnol, vol. 11, Jan. 2023, doi: 10.3389/fbioe.2023.1100155.

[70] M. Vignesh et al., “Development of Biomedical Implants through Additive Manufacturing: A Review,” J Mater Eng Perform, vol. 30, no. 7, pp. 4735–4744, Jul. 2021, doi: 10.1007/s11665-021-05578-7.

[71] Y. Bozkurt and E. Karayel, “3D printing technology; methods, biomedical applications, future opportunities and trends,” Journal of Materials Research and Technology, vol. 14, pp. 1430–1450, Sep. 2021, doi: 10.1016/j.jmrt.2021.07.050.

[72] E. Davoodi et al., “Additively manufactured metallic biomaterials,” Bioact Mater, vol. 15, pp. 214–249, Sep. 2022, doi: 10.1016/j.bioactmat.2021.12.027.

[73] T. Tom et al., “Additive manufacturing in the biomedical field-recent research developments,” Results in Engineering, vol. 16, p. 100661, Dec. 2022, doi: 10.1016/j.rineng.2022.100661.

[74] A. N. Aufa, M. Z. Hassan, and Z. Ismail, “Recent advances in Ti-6Al-4V additively manufactured by selective laser melting for biomedical implants: Prospect development,” J Alloys Compd, vol. 896, p. 163072, Mar. 2022, doi: 10.1016/j.jallcom.2021.163072.

[75] K. Munir, A. Biesiekierski, C. Wen, and Y. Li, “Selective laser melting in biomedical manufacturing,” in Metallic Biomaterials Processing and Medical Device Manufacturing, Elsevier, 2020, pp. 235–269. doi: 10.1016/B978-0-08-102965-7.00007-2.

[76] W. Abd-Elaziem et al., “On the current research progress of metallic materials fabricated by laser powder bed fusion process: a review,” Journal of Materials Research and Technology, vol. 20, pp. 681–707, Sep. 2022, doi: 10.1016/j.jmrt.2022.07.085.

[77] A. Sola and A. Nouri, “Microstructural porosity in additive manufacturing: The formation and detection of pores in metal parts fabricated by powder bed fusion,” J Adv Manuf Process, vol. 1, no. 3, Jul. 2019, doi: 10.1002/amp2.10021.

[78] J. Feng, J. Fu, X. Yao, and Y. He, “Triply periodic minimal surface (TPMS) porous structures: from multi-scale design, precise additive manufacturing to multidisciplinary

applications," International Journal of Extreme Manufacturing, vol. 4, no. 2, p. 022001, Jun. 2022, doi: 10.1088/2631-7990/ac5be6.

[79] B. Herath et al., "Mechanical and geometrical study of 3D printed Voronoi scaffold design for large bone defects," Mater Des, vol. 212, p. 110224, Dec. 2021, doi: 10.1016/j.matdes.2021.110224.

[80] Z. A. Qureshi, S. A. B. Al-Omari, E. Elnajjar, O. Al-Ketan, and R. Abu Al-Rub, "Nature-inspired triply periodic minimal surface-based structures in sheet and solid configurations for performance enhancement of a low-thermal-conductivity phase-change material for latent-heat thermal-energy-storage applications," International Journal of Thermal Sciences, vol. 173, p. 107361, Mar. 2022, doi: 10.1016/j.ijthermalsci.2021.107361.

[81] K. Song, Z. Wang, J. Lan, and S. Ma, "Porous structure design and mechanical behavior analysis based on TPMS for customized root analogue implant," J Mech Behav Biomed Mater, vol. 115, p. 104222, Mar. 2021, doi: 10.1016/j.jmbbm.2020.104222.

[82] Y. Du et al., "Design and statistical analysis of irregular porous scaffolds for orthopedic reconstruction based on voronoi tessellation and fabricated via selective laser melting (SLM)," Mater Chem Phys, vol. 239, p. 121968, Jan. 2020, doi: 10.1016/j.matchemphys.2019.121968.

[83] H. Zhou, M. Zhao, Z. Ma, D. Z. Zhang, and G. Fu, "Sheet and network based functionally graded lattice structures manufactured by selective laser melting: Design, mechanical properties, and simulation," Int J Mech Sci, vol. 175, p. 105480, Jun. 2020, doi: 10.1016/j.ijmecsci.2020.105480.

[84] J. Lv et al., "Selective Laser Melting Fabrication of Porous Ti6Al4V Scaffolds With Triply Periodic Minimal Surface Architectures: Structural Features, Cytocompatibility,

and Osteogenesis,” Front Bioeng Biotechnol, vol. 10, May 2022, doi: 10.3389/fbioe.2022.899531.

[85] W. Peng, Y. Liu, and C. Wang, “Definition, measurement, and function of pore structure dimensions of bioengineered porous bone tissue materials based on additive manufacturing: A review,” Front Bioeng Biotechnol, vol. 10, Jan. 2023, doi: 10.3389/fbioe.2022.1081548.

[86] S. Shrestha and K. Chou, “Formation of keyhole and lack of fusion pores during the laser powder bed fusion process,” Manuf Lett, vol. 32, pp. 19–23, Apr. 2022, doi: 10.1016/j.mfglet.2022.01.005.

[87] S. Weber, J. Montero, C. Petroll, T. Schäfer, M. Bleckmann, and K. Paetzold, “The Fracture Behavior and Mechanical Properties of a Support Structure for Additive Manufacturing of Ti-6Al-4V,” Crystals (Basel), vol. 10, no. 5, p. 343, Apr. 2020, doi: 10.3390/cryst10050343.

[88] B. Al-Nawas and W. Wagner, “7.19 Materials in Dental Implantology ☆,” in Comprehensive Biomaterials II, Elsevier, 2017, pp. 341–377. doi: 10.1016/B978-0-12-803581-8.10235-8.

[89] F. Javed, H. B. Ahmed, R. Crespi, and G. E. Romanos, “Role of primary stability for successful osseointegration of dental implants: Factors of influence and evaluation,” Interv Med Appl Sci, vol. 5, no. 4, pp. 162–167, Dec. 2013, doi: 10.1556/imas.5.2013.4.3.

[90] L. Ramos Xavier Coutinho Nascimento, G. Monteiro Torelly, and C. Nelson Elias, “Analysis of bone stress and primary stability of a dental implant using strain and torque measurements,” Saudi Dent J, vol. 35, no. 3, pp. 263–269, Mar. 2023, doi: 10.1016/j.sdentj.2023.01.006.

[91] N. Kittur, R. Oak, D. Dekate, S. Jadhav, and P. Dhatrak, “Dental implant stability and its measurements to improve osseointegration at the bone-implant interface: A review,” Mater Today Proc, vol. 43, pp. 1064–1070, 2021, doi: 10.1016/j.matpr.2020.08.243.

[92] V. Swami, V. Vijayaraghavan, and V. Swami, “Current trends to measure implant stability,” The Journal of Indian Prosthodontic Society, vol. 16, no. 2, p. 124, 2016, doi: 10.4103/0972-4052.176539.

[93] D. Apostu, O. Lucaciu, C. Berce, D. Lucaciu, and D. Cosma, “Current methods of preventing aseptic loosening and improving osseointegration of titanium implants in cementless total hip arthroplasty: a review,” Journal of International Medical Research, vol. 46, no. 6, pp. 2104–2119, 2018, doi: 10.1177/0300060517732697.

[94] W. B. Swanson et al., “Scaffold Pore Curvature Influences MSC Fate through Differential Cellular Organization and YAP/TAZ Activity,” Int J Mol Sci, vol. 23, no. 9, p. 4499, Apr. 2022, doi: 10.3390/ijms23094499.

[95] Z. Dong and X. Zhao, “Application of TPMS structure in bone regeneration,” Engineered Regeneration, vol. 2, pp. 154–162, 2021, doi: 10.1016/j.engreg.2021.09.004.

[96] E. F. Lehder, I. A. Ashcroft, R. D. Wildman, L. A. Ruiz-Cantu, and I. Maskery, “A multiscale optimisation method for bone growth scaffolds based on triply periodic minimal surfaces,” Biomech Model Mechanobiol, vol. 20, no. 6, pp. 2085–2096, Dec. 2021, doi: 10.1007/s10237-021-01496-8.

[97] J. Lv et al., “Selective Laser Melting Fabrication of Porous Ti6Al4V Scaffolds With Triply Periodic Minimal Surface Architectures: Structural Features, Cytocompatibility, and Osteogenesis,” Front Bioeng Biotechnol, vol. 10, May 2022, doi: 10.3389/fbioe.2022.899531.

[98] T. Pires, J. Santos, R. B. Ruben, B. P. Gouveia, A. P. G. Castro, and P. R. Fernandes, “Numerical-experimental analysis of the permeability-porosity relationship in triply periodic minimal surfaces scaffolds,” J Biomech, vol. 117, p. 110263, Mar. 2021, doi: 10.1016/j.jbiomech.2021.110263.

[99] J. Santos, T. Pires, B. P. Gouveia, A. P. G. Castro, and P. R. Fernandes, “On the permeability of TPMS scaffolds,” J Mech Behav Biomed Mater, vol. 110, p. 103932, Oct. 2020, doi: 10.1016/j.jmbbm.2020.103932.

[100] Castro, Pires, Santos, Gouveia, and Fernandes, “Permeability versus Design in TPMS Scaffolds,” Materials, vol. 12, no. 8, p. 1313, Apr. 2019, doi: 10.3390/ma12081313.

[101] D. Karaman and H. Ghahramanzadeh Asl, “The effects of sheet and network solid structures of similar TPMS scaffold architectures on permeability, wall shear stress, and velocity: A CFD analysis,” Med Eng Phys, vol. 118, p. 104024, Aug. 2023, doi: 10.1016/j.medengphy.2023.104024.

[102] H. Liang et al., “Trabecular-like Ti–6Al–4V scaffold for bone repair: A diversified mechanical stimulation environment for bone regeneration,” Compos B Eng, vol. 241, p. 110057, Jul. 2022, doi: 10.1016/j.compositesb.2022.110057.

[103] H. Liang et al., “Trabecular-like Ti-6Al-4V scaffolds for orthopedic: fabrication by selective laser melting and in vitro biocompatibility,” J Mater Sci Technol, vol. 35, no. 7, pp. 1284–1297, Jul. 2019, doi: 10.1016/j.jmst.2019.01.012.

[104] M. V. Kiselevskiy et al., “Development of Bioactive Scaffolds for Orthopedic Applications by Designing Additively Manufactured Titanium Porous Structures: A Critical Review,” Biomimetics, vol. 8, no. 7, p. 546, Nov. 2023, doi: 10.3390/biomimetics8070546.

[105] Castro, Pires, Santos, Gouveia, and Fernandes, “Permeability versus Design in TPMS Scaffolds,” Materials, vol. 12, no. 8, p. 1313, Apr. 2019, doi: 10.3390/ma12081313.

[106] C. Poon, “Measuring the density and viscosity of culture media for optimized computational fluid dynamics analysis of in vitro devices,” J Mech Behav Biomed Mater, vol. 126, p. 105024, Feb. 2022, doi: 10.1016/j.jmbbm.2021.105024.

[107] B. Pasha Mahammod, E. Barua, A. B. Deoghare, and K. M. Pandey, “Permeability quantification of porous polymer scaffold for bone tissue engineering,” Mater Today Proc, vol. 22, pp. 1687–1693, 2020, doi: 10.1016/j.matpr.2020.02.186.

[108] A. Campos Marín, M. Brunelli, and D. Lacroix, “Flow perfusion rate modulates cell deposition onto scaffold substrate during cell seeding,” Biomech Model Mechanobiol, vol. 17, no. 3, pp. 675–687, Jun. 2018, doi: 10.1007/s10237-017-0985-4.

[109] G. Li et al., “In vitro and in vivo study of additive manufactured porous Ti6Al4V scaffolds for repairing bone defects,” Sci Rep, vol. 6, no. 1, p. 34072, Sep. 2016, doi: 10.1038/srep34072.

[110] E. M. Bueno, G. Laevsky, and G. A. Barabino, “Enhancing cell seeding of scaffolds in tissue engineering through manipulation of hydrodynamic parameters,” J Biotechnol, vol. 129, no. 3, pp. 516–531, May 2007, doi: 10.1016/j.jbiotec.2007.01.005.

[111] P. Song et al., “Dual modulation of crystallinity and macro-/microstructures of 3D printed porous titanium implants to enhance stability and osseointegration,” J Mater Chem B, vol. 7, no. 17, pp. 2865–2877, 2019, doi: 10.1039/C9TB00093C.

[112] B. Wysocki et al., “The influence of chemical polishing of titanium scaffolds on their mechanical strength and in-vitro cell response,” Materials Science and Engineering: C, vol. 95, pp. 428–439, Feb. 2019, doi: 10.1016/j.msec.2018.04.019.

[113] B. Wysocki et al., “Post Processing and Biological Evaluation of the Titanium Scaffolds for Bone Tissue Engineering,” Materials, vol. 9, no. 3, p. 197, Mar. 2016, doi: 10.3390/ma9030197.

[114] C. Daish et al., “Estimation of anisotropic permeability in trabecular bone based on microCT imaging and pore-scale fluid dynamics simulations,” Bone Rep, vol. 6, pp. 129–139, Jun. 2017, doi: 10.1016/j.bonr.2016.12.002.

[115] A. J. Beaudoin, W. M. Mihalko, and W. R. Krause, “Finite element modelling of polymethylmethacrylate flow through cancellous bone,” J Biomech, vol. 24, no. 2, pp. 127–136, Jan. 1991, doi: 10.1016/0021-9290(91)90357-S.

[116] F. Deng, L. Liu, Z. Li, and J. Liu, “3D printed Ti6Al4V bone scaffolds with different pore structure effects on bone ingrowth”, doi: 10.1186/s13036-021-00255-8.

[117] L. Liu, S. Wang, J. Liu, F. Deng, Z. Li, and Y. Hao, “Architectural design of Ti6Al4V scaffold controls the osteogenic volume and application area of the scaffold,” 2020, doi: 10.1016/j.jmrt.2020.11.061.

[118] S. Ma, Q. Tang, Q. Feng, J. Song, X. Han, and F. Guo, “Mechanical behaviours and mass transport properties of bone-mimicking scaffolds consisted of gyroid structures manufactured using selective laser melting,” 2019, doi: 10.1016/j.jmbbm.2019.01.023.

[119] M. Kaur and K. Singh, “Review on titanium and titanium based alloys as biomaterials for orthopaedic applications,” Materials Science and Engineering: C, vol. 102, pp. 844–862, Sep. 2019, doi: 10.1016/j.msec.2019.04.064.

[120] A. Sidambe, “Biocompatibility of Advanced Manufactured Titanium Implants—A Review,” Materials, vol. 7, no. 12, pp. 8168–8188, Dec. 2014, doi: 10.3390/ma7128168.

[121] A. Ouldyerou, A. Merdji, L. Aminallah, S. Roy, H. Mehboob, and M. Özcan, “Biomechanical performance of Ti-PEEK dental implants in bone: An in-silico analysis,” J Mech Behav Biomed Mater, vol. 134, p. 105422, Oct. 2022, doi: 10.1016/j.jmbbm.2022.105422.

[122] L. Zhang, B. Song, S.-K. Choi, and Y. Shi, “A topology strategy to reduce stress shielding of additively manufactured porous metallic biomaterials,” Int J Mech Sci, vol. 197, p. 106331, May 2021, doi: 10.1016/j.ijmecsci.2021.106331.

[123] D. W. Abueidda, M. Elhebeary, C.-S. (Andrew) Shiang, S. Pang, R. K. Abu Al-Rub, and I. M. Jasiuk, “Mechanical properties of 3D printed polymeric Gyroid cellular structures: Experimental and finite element study,” Mater Des, vol. 165, p. 107597, Mar. 2019, doi: 10.1016/j.matdes.2019.107597.

[124] X. Zheng et al., “A TMPS-designed personalized mandibular scaffolds with optimized SLA parameters and mechanical properties,” Front Mater, vol. 9, Aug. 2022, doi: 10.3389/fmats.2022.966031.

[125] K. Song, Z. Wang, J. Lan, and S. Ma, “Porous structure design and mechanical behavior analysis based on TPMS for customized root analogue implant,” J Mech Behav Biomed Mater, vol. 115, p. 104222, Mar. 2021, doi: 10.1016/j.jmbbm.2020.104222.

[126] Y. Xiong et al., “Fatigue behavior and osseointegration of porous Ti-6Al-4V scaffolds with dense core for dental application,” Mater Des, vol. 195, p. 108994, Oct. 2020, doi: 10.1016/j.matdes.2020.108994.

[127] S. A. Naghavi et al., “Mechanical Characterisation and Numerical Modelling of TPMS-Based Gyroid and Diamond Ti6Al4V Scaffolds for Bone Implants: An Integrated

Approach for Translational Consideration," Bioengineering, vol. 9, no. 10, p. 504, Sep. 2022, doi: 10.3390/bioengineering9100504.

[128] L. Yang et al., "Fatigue properties of Ti-6Al-4V Gyroid graded lattice structures fabricated by laser powder bed fusion with lateral loading," Addit Manuf, vol. 46, p. 102214, Oct. 2021, doi: 10.1016/j.addma.2021.102214.

[129] F. Hild and S. Roux, "Digital Image Correlation: from Displacement Measurement to Identification of Elastic Properties – a Review," Strain, vol. 42, no. 2, pp. 69–80, May 2006, doi: 10.1111/j.1475-1305.2006.00258.x.

[130] B. Pan, K. Qian, H. Xie, and A. Asundi, "Two-dimensional digital image correlation for in-plane displacement and strain measurement: a review," Meas Sci Technol, vol. 20, no. 6, p. 062001, Jun. 2009, doi: 10.1088/0957-0233/20/6/062001.

[131] W. Radlof, C. Benz, and M. Sander, "Numerical and experimental investigations of additively manufactured lattice structures under quasi-static compression loading," Material Design & Processing Communications, vol. 3, no. 3, Jun. 2021, doi: 10.1002/mdp2.164.

[132] H. Hyer et al., "High strength WE43 microlattice structures additively manufactured by laser powder bed fusion," Materialia (Oxf), vol. 16, p. 101067, May 2021, doi: 10.1016/j.mtla.2021.101067.

[133] Y. Barranger, P. Doumalin, J. C. Dupré, and A. Germaneau, "Strain Measurement by Digital Image Correlation: Influence of Two Types of Speckle Patterns Made from Rigid or Deformable Marks," Strain, vol. 48, no. 5, pp. 357–365, Oct. 2012, doi: 10.1111/j.1475-1305.2011.00831.x.

[134] X. P. Tan, Y. J. Tan, C. S. L. Chow, S. B. Tor, and W. Y. Yeong, "Metallic powder-bed based 3D printing of cellular scaffolds for orthopaedic implants: A state-of-the-art review on manufacturing, topological design, mechanical properties and biocompatibility," Materials Science and Engineering: C, vol. 76, pp. 1328–1343, Jul. 2017, doi: 10.1016/j.msec.2017.02.094.

[135] A. F. Mota, M. A. R. Loja, J. I. Barbosa, and J. A. Rodrigues, "Porous Functionally Graded Plates: An Assessment of the Influence of Shear Correction Factor on Static Behavior," Mathematical and Computational Applications, vol. 25, no. 2, p. 25, Apr. 2020, doi: 10.3390/mca25020025.

[136] J. Kim, K. K. Żur, and J. N. Reddy, "Bending, free vibration, and buckling of modified couples stress-based functionally graded porous micro-plates," Compos Struct, vol. 209, pp. 879–888, Feb. 2019, doi: 10.1016/j.compstruct.2018.11.023.

[137] "ASTM E9-19: Standard Test Methods of Compression Testing of Metallic Materials at Room Temperature." 2019.

[138] "ISO 13314:2011(E) Mechanical testing of metals — Ductility testing — Compression test for porous and cellular metals." 2011.

[139] L. Guo et al., "Understanding keyhole induced-porosities in laser powder bed fusion of aluminum and elimination strategy," Int J Mach Tools Manuf, vol. 184, p. 103977, Jan. 2023, doi: 10.1016/j.ijmachtools.2022.103977.

[140] M. Araya, M. Jaskari, T. Rautio, T. Guillén, and A. Järvenpää, "Assessing the compressive and tensile properties of TPMS-Gyroid and stochastic Ti64 lattice structures: A study on laser powder bed fusion manufacturing for biomedical implants," Journal of

Science: Advanced Materials and Devices, vol. 9, no. 1, p. 100663, Mar. 2024, doi: 10.1016/j.jsamd.2023.100663.

[141] C. Zhang et al., “Mechanical behavior of a titanium alloy scaffold mimicking trabecular structure,” J Orthop Surg Res, vol. 15, no. 1, p. 40, Dec. 2020, doi: 10.1186/s13018-019-1489-y.

[142] A. Yánez, A. Cuadrado, O. Martel, H. Afonso, and D. Monopoli, “Gyroid porous titanium structures: A versatile solution to be used as scaffolds in bone defect reconstruction,” Mater Des, vol. 140, pp. 21–29, Feb. 2018, doi: 10.1016/j.matdes.2017.11.050.

[143] T. M. van Eijden, “Biomechanics of the Mandible,” Critical Reviews in Oral Biology & Medicine, vol. 11, no. 1, pp. 123–136, Jan. 2000, doi: 10.1177/10454411000110010101.

[144] A. Baldini, G. Bruzzesi, D. Zaffe, M. Giacopini, A. Strozzi, and A. De Pol, “Biomechanical aspects in dental replacements,” 2008, pp. 197–243. doi: 10.2495/978-1-84564-096-5/09.

[145] A. Khaohoen, T. Sornsuwan, P. Chaijareenont, P. Poovarodom, C. Rungsiyakull, and P. Rungsiyakull, “Biomaterials and Clinical Application of Dental Implants in Relation to Bone Density—A Narrative Review,” J Clin Med, vol. 12, no. 21, p. 6924, Nov. 2023, doi: 10.3390/jcm12216924.

[146] Z. Fan, G. Huang, Y. Lu, Y. Chen, F. Zeng, and J. Lin, “Full compression response of FG-based scaffolds with varying porosity via an effective numerical scheme,” Int J Mech Sci, vol. 223, p. 107294, Jun. 2022, doi: 10.1016/j.ijmecsci.2022.107294.